Vehicle-to-grid (V2G) Reactive Power Operation Analysis of the EV/PHEV Bidirectional Battery Charger

A Dissertation
Presented for the
Doctor of Philosophy
Degree
The University of Tennessee, Knoxville

Mithat Can Kisacikoglu
May 2013

to my wife Sevda and my father Ahmet Refik Kisacikoglu

Acknowledgements

I would like to thank first and foremost to Dr. Leon Tolbert for supporting me at all stages of this dissertation study and for being my mentor. I learnt a lot from his professionalism and project management skills. Moreover, he supported the study from the beginning to the end with his patience and guidance. I also would like to thank Dr. Burak Ozpineci for his strong and sincere help and support, and for providing me the opportunity to use the laboratory space at Oak Ridge National Laboratory. I also would like to thank Dr. Fred Wang for very inspiring technical discussions on the subject. Moreover, I thank Dr. Paul Frymier for accepting to be in the committee and for his thought provoking questions throughout the study.

There are many people that I would like to thank in the lab. Each of them has helped me. I would like to thank to Dr. Shengnan Li, Dr. Faete Filho, Lakshmi Reddy, Ben Guo, Dr. Ming Li, Dr. Lijun Hang, Bailu Xiao, Dr. Dong Dong, Dr. Sarina Adhikari, Fan Xu, Zhuxian Xu, Jing Xue, Brad Trento, Weimin Zhang, Zheyu Zhang, Yalong Li, Xiaojie Shi, Dr. Wenjie Chen, Zhiqiang Wang, Jing Wang, Yutian Cui, Kumaraguru Prabakar, Wenchao Cao, Liu Yang, Yang Xue, Yiwei Ma, Martin Stempfle, and Edward Jones for providing their time and intellectual support with discussions and help. They have always been supportive. I also want to thank to our lab manager Bob Martin for making our job easier in the lab. I thank Dr. Omer Onar, Dr. Yan Xu, and Dr. Aleksandar Dimitrovski from ORNL for their technical discussions. I would also like to thank to the other people whom I could not remember their names here for their help during my Ph.D. study.

Last but certainly not the least, I want to thank my wife Sevda Kisacikoglu, my mother Mine Kisacikoglu, and my sister Deniz Kisacikoglu for their love and support.

Abstract

More battery powered electric vehicles (EVs) and plug-in hybrid electric vehicles (PHEVs) will be introduced to the market in 2013 and beyond. Since these vehicles have large batteries that need to be charged from an external power source or directly from the grid, their charging circuits and grid interconnection issues are garnering more attention.

It is possible to incorporate more than one operation mode in a charger by allowing the power to flow bidirectionally. Usually, the bidirectional power transfer stands for two-way transfer of active power between the charger and the grid. The general term of sending active power from the vehicle to the grid is called vehicle to grid (V2G).

While plug-in electric vehicles (PEVs) potentially have the capability to fulfill the energy storage needs of the electric grid, the degradation on the battery during this operation makes it less preferable by the auto manufacturers and consumers. On the other hand, the on-board chargers can also supply energy storage system applications such as reactive power compensation, voltage regulation, and power factor correction without the need of engaging the battery with the grid and thereby preserving its lifetime.

This study shows the effect of reactive power operation on the design and operation of single-phase on-board chargers that are suitable for reactive power support. It further introduces a classification of single-phase ac-dc converters that can be used in on-board PEV chargers based on their power transfer capabilities in addition to the currently available surveys.

The cost of supplying reactive power is also important to effectively evaluate reactive power operation using chargers. There are two major impacts: one is on the converter design (incremental costs) and the other is on the operating electricity costs. Their combination shows the total effect and cost of reactive power operation and can be compared with other options of the utility grid to supply reactive power. Two customer scenarios are investigated to have two options of reactive power support. Level 1 and Level 2 reactive power support are evaluated separately.

Contents

List of Tables

List of Figures

Acronyms

ac alternating current.

ADC analog to digital converter.

Ah amp-hour.

BEV battery electric vehicle.

BMS battery management system.

CC constant current.

CD charge-depleting.

CS charge-sustaining.

CV constant voltage.

dc direct current.

DOD depth of discharge.

DSP digital signal processor.

EV electric vehicle.

GM General Motors.

HEV hybrid electric vehicle.

HF high frequency.

ICE internal combustion engine.

KVL Kirchhoff's voltage law.

kWh kilowatt-hour.

LCO lithium-cobalt-dioxide.

LED light emitting diode.

LFP lithium-iron-phosphate.

Li-ion lithium-ion.

LMS lithium-manganese oxide spinel.

MOSFET metal-oxide-semiconductor field-effect transistor.

NCA nickel-cobalt-aluminum.

NiMH nickel metal hydride.

NMC nickel-manganese-cobalt.

ORNL Oak Ridge National Laboratory.

PCB printed circuit board.

PCC point of common coupling.

PEV plug-in electric vehicle.

pf power factor.

PFC power factor corrected.

PHEV plug-in hybrid electric vehicle.

PR proportional resonant.

rms root mean square.

Si silicon.

SiC silicon-carbide.

SOC state of charge.

SOD state of discharge.

SOH state of health.

TDD total demand distortion.

THD total harmonic distortion.

TI Texas Instruments.

V2G vehicle to grid.

VRLA valve-regulated lead-acid.

W watt.

W/kg watt per kilogram.

W/l watt per liter.

Wh watt-hour.

Wh/kg watt-hour per kilogram.

Wh/l watt-hour per liter.

Chapter 1

Background on Grid Connection of Electric Drive Vehicles and Vehicle Battery Charging

1.1 Introduction

According to the international energy outlook report, the world transportation energy usage is going to increase by 44% in 2035 (compared to 2008) [13]. Therefore, technologies related to reducing oil consumption have one of the utmost challenges in today's vehicle research.

Alternative vehicle technologies to replace conventional vehicles include hybrid electric vehicles (HEVs), PHEVs, and EVs (also known as battery electric vehicles (BEVs)). The dichotomy between HEVs and EVs/PHEVs is the presence of a charger in the latter group. PHEVs and EVs will be termed collectively as PEVs in this study.

The charger is a power conversion equipment that connects the vehicle battery to the grid. Chargers for these vehicles have the ability to foster the interaction of vehicle and the external power source, i.e. the utility grid. Chargers convert the ac voltage to a dc magnitude for the specific battery needs of PEVs. In order for the utility to be spared by the impact of the large number of PEV connections, chargers play an important role in the grid integration of these new technology vehicles.

It is possible to incorporate more than one operation mode in a charger by allowing the power to flow bidirectionally. Usually, the bidirectional power transfer stands for two-way transfer of active power between the charger and the grid. The general term of sending active power from the vehicle to the grid is called V2G. The economic benefits of this operation has been a research subject for more than a decade because of the large energy reserve of an electric vehicle battery and the potential of thousands of these connected to the grid [14–16].

While PEVs potentially have the capability to fulfill the energy storage needs of the electric grid, the degradation on the battery during this operation makes it less preferable by the auto manufacturers and consumers unless a properly structured battery warranty and compensation model is implemented [17–20]. On the other hand, the on-board chargers can also supply energy storage system applications such as reactive power compensation, voltage regulation, and power factor correction without the need of engaging the battery with the grid and thereby preserving their lifetime.

Reactive power consumed at the load side is transmitted from the energy source to the load through the transmission and distribution system. This causes increased energy losses and decreases the system efficiency. For long distances, line reactance for line "k" (X_k) becomes much larger than the line resistance (R_k). Because reactive power losses are proportional with line susceptance ($B_k = -X_k/(R_k^2 + X_k^2)$) and real power losses are proportional with line conductance ($G_k = R_k/(R_k^2 + X_k^2)$), the relative losses of reactive power become much greater than the relative losses of active power on the transmission lines [21]. Therefore, reactive power is best utilized when it is generated close to where it is needed. Moreover, residential appliances such as microwaves, washing machines, air conditioners, dishwashers, and refrigerators consume reactive power for which the residential costumers do not pay, but the utility

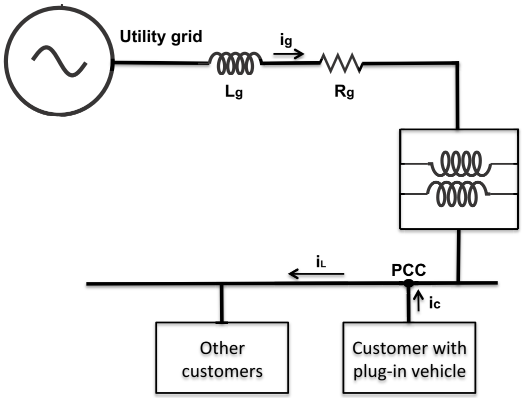

Figure 1.1: Proposed reactive power support diagram using PEVs.

is responsible to deliver. PEVs can readily supply this reactive power need locally without the need of remote VAR transmission.

Fig. 1.1 shows the proposed application of PEVs. Customers with a PEV that carries an on-board charger can negotiate with the utility grid to allow the usage of the charger for grid support. The charger compensates for the reactive current (i_c) that either the customer with the PEV or other customers without a PEV demand from the utility grid. Generating reactive current at the point of common coupling (PCC) provides increased efficiency of power transfer through transmission lines and decreases transformer overloading.

A vehicle can provide reactive power irrespective of the battery state of charge (SOC). The charger can supply reactive power at any time even during charging. However, the selected topology and the effect of the reactive power on the operation of the charger and the battery should be well analyzed. On-board single-phase charging systems have been researched in terms of different power factor corrected (PFC) rectifier topologies that can be used for unidirectional charging operation [22, 23]. Other studies have surveyed bidirectional single-phase ac-dc converter topologies that are suitable for V2G applications [24–26]. Single-phase battery-powered renewable energy systems have also been well researched in terms of ac-dc power transfer calculations, second harmonic current ripple elimination, and reduction of electrolytic dc-link capacitors [27, 28]. However, there is a need in the literature for technical analysis and survey of topologies suitable for V2G reactive power operation for single-phase on-board PEV charging systems and its effect on both the charger design and battery charging operation.

A charger is composed of two power conversion stages: a single/three-phase ac-dc conversion stage, and a dc-dc conversion stage. This study focuses on single-phase chargers that are mostly suited for on-board charging applications. The front-end ac-dc conversion stage can have PFC unidirectional and four-quadrant bidirectional power transfer options. The design of the charger changes considerably between the different options and applications. Moreover, single-phase power conversion also adversely affects the energy storage requirements during reactive power operation due to increased ripple energy storage at the dc-link. Another concern is the limitation of the ac line current harmonics either during charging the traction battery or when the vehicle supplies power back to the grid. DC-DC conversion stage can either have an isolated or non-isolated topology based on the mandated protection requirements by the auto manufacturers. Another concern is the limitation of battery charging current harmonics which adversely affect the lifetime of the battery.

1.2 PHEV and EV Technology

1.2.1 Definitions of HEV, PHEV, and EV

Today, there are three types of passenger vehicles available in the market operating with an electric traction motor powered by a battery: HEVs, PHEVs, and EVs or BEVs. HEVs have the smallest size battery pack, and therefore an electric motor is used to drive at very low cruise speeds or to assist the internal combustion engine (ICE) during higher power requirements. Therefore, HEVs offer customers a way to increase gasoline mileage by having batteries and electric drive systems work with the ICE. The most efficient hybrid vehicles reduce the gas consumption by around 40% compared to similar size conventional ICE vehicles. However, HEVs lack the availability to go for more than just short distances at low speeds with only electric power because the battery is not capable of storing enough energy to power the vehicle for a daily commute.

PHEVs, however, provide an all-electric range up to a pre-specified distance with a larger size battery pack, which is not inherent in HEVs. There are several definitions on how a PHEV is defined. According to [29], the battery pack capacity should be at least 4 kWh, and the PHEV must be rechargeable by an external source of electricity. Another definition adds the ability to drive the vehicle at least 10 miles in electric-only mode without consuming any gasoline as a requirement for a vehicle to be classified as a PHEV. By definition, an EV has only an electric motor in the traction drive which is powered by an on-board battery, and conventional vehicles have only combustion engines. The 2010 Toyota Prius HEV has only 1.3 kWh on-board traction battery capacity. As a comparison, the 2011 Chevrolet Volt PHEV has a 16 kWh battery capacity [30], and 2011 Nissan Leaf EV has a capacity of 24 kWh on-board battery energy storage [31].

PHEVs operate in charge-depleting (CD) mode when most/all of the energy comes from the battery during the all-electric mode; hence, the battery is in the deep cycle mode. If the battery reaches its minimum state of charge, the control system switches to the charge-sustaining (CS) mode where the battery experiences only shallow cycles. PHEVs are usually described as PHEV-X where X is the number of miles that a PHEV can go just with the electric energy. The explanation of the different operation modes in EV, HEV, and PHEV are demonstrated in Fig. 1.2.

1.2.2 The current status of PEVs

Light-duty passenger PEVs that have demonstrated successful market penetration and that will be in mass market in upcoming years prove that the challenges regarding the grid connection issues of these vehicles need to be taken very seriously. This

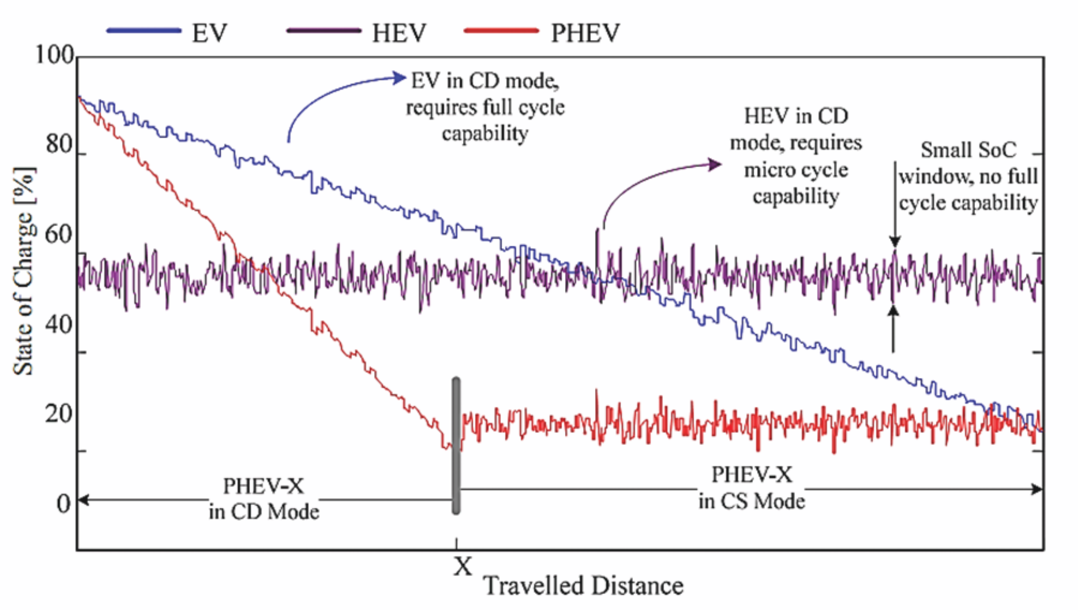

Figure 1.2: Charge depleting and charge sustaining modes for the EV, HEV, and PHEV [9].

section lists the market vehicles in terms of their grid-related features such as energy storage and charging specifications.

Table 1.1 lists the important specifications of the surveyed vehicles. As shown in this table, the battery pack voltage has an increasing trend compared to older versions of the vehicles. Most of the vehicles have more than 330 V nominal pack voltage. However, mechanical configuration of cells changes from vehicle to vehicle. The on-board dedicated charger output power rating generally stays between 3 kW to 7 kW.

Design of the charger of a vehicle traction battery includes different options in terms of where to place the charger and how to design the charger. The circuit topology, location, connection type to the vehicle, electrical waveform of the charging coupler, and the direction of power flow can totally change the design of the charger (more on this classification is explained in [32]). Although the surveyed market vehicles employ different combinations of the above classification, most of the vehicles carry its charger on-board for increased charging availability. Although carrying the charger on-board increases the availability of charging the vehicle, it also brings added cost and weight to the vehicle. Also, the power rating of the charger is inversely proportional to the charging time necessary to fully charge the vehicle battery. Therefore, it is desired to have a high power charging rate to make the EV charging experience comparable to the filling time of a gasoline tank. However, due to space and weight limitations on a vehicle, the on-board charger must be restricted in power rating. So, these two objectives contradict with each other and a compromise should be made. The power rating is also related to the type of the vehicle. For instance, EVs usually require a charger with a higher power rating compared to PHEVs due to having a larger battery. As shown in Table 1.1, battery sizes of an EV in the U.S. market change between 16 kWh - 53 kWh whereas a PHEV has its pack with 4.4 kWh - 20.1 kWh energy capacity. Therefore, for comparable charging time, an EV usually requires its charger to have a higher power rating. For instance, EVs with integrated chargers[*] (BMW Mini E and Tesla Roadster) have higher on-board charging power capability (> 11 kW).

1.3 Vehicular Traction Battery Technology Status

For years, the biggest hindrance of deployment of EVs has been the lack of a portable high-energy storage device. With recent developments in battery technology, it has been easier to overcome this obstacle. During this advancement of vehicle grade batteries, the main categories that the vehicle battery research has focused on are: energy, power, life span, safety, and cost [49].

The energy stored in a battery determines the electric drive range and is measured in amp-hour (Ah) or watt-hour (Wh). The electric drive range of a PHEV is proportional to the amount of stored energy, as more energy is required to drive the vehicle in electric-only mode. Since the available space is limited in vehicles, researchers usually focus on the energy density (watt-hour per liter (Wh/l)) or specific

---

[*] The definition of integrated chargers are explained in chapter 2

Table 1.1: Specifications for commercially available PHEV/EVs.

#	Vehicle Make and Model	Type	Battery Size (kWh)	Electric range (mi)	Battery voltage (V)	Charger power (kW)	Level 2 charging time(h)
1	BMW Mini E [33]	EV	35	156	380	11.5	3 - 4.5
2	BMW Active E [34,35]	EV	32	100	N/A	7.7	4 - 5
3	BYD F3DM [36]	PHEV	16	40 - 60	N/A	N/A	7
4	Coda Sedan	EV	36	150	333	6.6	6
5	Fisker Karma [37]	PHEV	20.1	50	336	3.3	6
6	Ford Focus Electric [38]	EV	23	100	N/A	6.6	3-4
7	Ford Transit Connect EV [39,40]	EV	28.3	80	390	3.3	6-8
8	GM Chevrolet Volt [30]	PHEV	15	35	N/A	3.3	4
9	GM EV1 (NiMH version) [41]	EV	26.4	160	343	6.6	3
10	Mitsubishi MiEV [42]	EV	16	62	330	3.3	6.5
11	Nissan Leaf [31]	EV	24	73	365	3.3	7
12	Renault Fluence Z.E. [43]	EV	22	100	NA	3.7	6-8
13	Renault Kangoo Z.E. [43]	EV	22	100	NA	3.7	6-8
14	Smart Fortwo ED	EV	16.5	84	NA	3.3	8
15	Tesla Roadster [44]	EV	53	244	375	16.8	3-4
16	Tesla Model-S [44]	EV	42,65, and 85	160, 230, and 300	N/A	N/A	N/A
17	Think City [45]	EV	24	100	N/A	3.3	8
18	Toyota Prius Plug-in Hybrid [46]	PHEV	4.4	15	346	2	4
19	Toyota RAV4 EV- 1^{st} Gen. [47]	EV	27	130	288	6	N/A
20	Toyota RAV4 EV- 2^{nd} Gen. [48]	EV	37	96	N/A	N/A	12

energy (watt-hour per kilogram (Wh/kg)) of a battery. The amount of stored energy is more of a concern for EVs compared to PHEVs, since EVs do not have a gasoline tank to extend the driving range on a single charge.

The battery power is measured in watt (W); however, as in the energy and energy density, battery researchers focus on power density (watt per liter (W/l)) or specific power (watt per kilogram (W/kg)) in battery terminology. Higher battery power translates into higher motor torque or vehicle acceleration. The power rating is also important to determine how fast a battery can be charged which is usually much slower compared to discharging.

The battery life span includes two different cycle measurements; the first of which is the minimum calendar life. A vehicle battery is expected to operate above a specified capacity for the calendar life period of 15 years with limited degradation [49]. The next important item for the battery lifetime is the cycle life which relates to the total number of charging-discharging cycles that the battery is exposed to during its lifetime. A battery experiences both deep and shallow charge-discharge cycles depending on its operation mode. A deep cycle means one complete charging and discharging of the battery usually between 20% and 90% of the SOC[†]. A shallow cycle usually occupies a very narrow SOC window, i.e. 40% - 60%. A shallow cycle is more battery friendly compared to a deep cycle since a smaller SOC window is used. In other words, a deep cycle affects the battery lifetime worse than a shallow cycle.

Safety should always be kept as the number one priority for all of the operating conditions. Batteries require strict safety precautions, which are detailed in section 1.4.4.

Batteries should meet the above requirements with an affordable cost goal. For years, high battery costs have prevented the technology from being widespread. However, with recent research and development advances, PEVs have been in the market recently with the cost and performance characteristics comparable to conventional vehicles in the market [30, 31].

There are three main battery technologies that stand out from the rest. These are lead-acid, nickel metal hydride (NiMH), and Li-ion technologies. In this section, these batteries are investigated and compared with respect to their weight, volume, energy, charge and discharge power, operating temperature range, life span (cycle and calendar), cost, safety-electrical abuse tolerance, and availability.

[†] The definition of SOC is given in section 1.4.1

1.3.1 Previous battery technologies: lead-acid and NiMH batteries

The lead-acid battery was the most preferred option to power early EVs; therefore, it is readily available at a reasonable cost owing to the maturity of the technology and manufacturing. Its good discharge power capacity makes it easier to respond fast to load changes. In contrast, it has a low energy density and is heavy. Also, lead-acid batteries have short life spans as a consequence of the deterioration from deep discharges. The first EV released to the market General Motors (GM) EV1 used a lead-acid battery to provide power to electrical drive motor.

A NiMH battery has simple charge and discharge reactions, and it does not have soluble intermediates or complex phase changes as opposed to lead acid batteries [50]. Therefore, NiMH batteries have higher power and energy densities and a longer intrinsic cycle life. Also, a NiMH battery is resistant to damage as it can tolerate moderate overcharges and deep discharges. Due to the high energy density of NiMH batteries, the range of a vehicle with a NiMH battery is doubled compared to a vehicle with the same size and weight lead-acid battery [50]. Finally, due to low internal resistance, a NiMH battery has a much higher charge acceptance capability which results in higher charging efficiency.

One drawback of the NiMH batteries is the high self-discharge rate compared to lead acid batteries, which causes batteries to lose charge when not used. The self-discharge is 5-10% on the first day and averages around 0.5-1% per day at room temperature [51].They also have higher cost compared to lead-acid, poor charge acceptance capability at high temperatures that result in low cell charging efficiency at these temperatures. Most of the HEVs currently in the market employ a NiMH battery including Toyota Prius and Honda Insight.

1.3.2 Li-ion battery technology for vehicular traction application

Lithium-ion battery cells are expected to become viable energy storage devices for coming generations of PEVs according to experts [52]. The superiority of Li-ion batteries have been demonstrated over other type of batteries in supplying greater discharge power for faster acceleration and higher energy density for increased all-electric range. Furthermore, higher efficiency operation and lower weight make them preferable for vehicular applications. However, some issues including cell life (calendar and number of charge-discharge cycles), cost, and safety still need improvement and are the main impediments to widely employ Li-ion batteries in PEVs [52, 53]. One important issue with Li-ion batteries is the need to equalize each cell charge to balance out the total charge among the cells in a more precise way compared to lead-acid and NiMH chemistries. In addition, since lithium is more chemically reactive, it is more intolerant to abusive conditions which require the battery management system to protect it from overcharging and overheating. Poor cold temperature operation is another drawback of Li-ion battery.

The term Li-ion does not specifically correspond to particular battery chemistry as NiMH does. Rather, it includes several chemistries that can be classified with respect to different cathode contenders. Some of the major cathode compositions are lithium-cobalt-dioxide (LCO), nickel-manganese-cobalt (NMC), nickel-cobalt-aluminum (NCA), lithium-manganese oxide spinel (LMS), and lithium-iron-phosphate (LFP). Although each type of Li-ion cell has some advantages, lithium-iron-phosphate cathode is a new and promising cathode for PEV applications with increased safety and stability features [52,54]. Its failure due to overcharging does not emit too much heat. However, it has lower cell voltages compared to other cathodes, and hence many of these have to be connected in series requiring more balancing issues. To solve the low cell voltage problem, nanostructures are being used. This new nanotechnology offers better power and longer life than earlier generations [52].

A Li-ion cell with lithium titanate spinel anode rather than graphite is also advantageous for a vehicle to charge/discharge faster. In addition, it has improved cycle and calendar lifetime. In this case, energy density is compromised at the expense of getting a much broader operation temperature range as well as a safer voltage range [55].

Consequently, researchers agree that among batteries Li-ion batteries stand out for their advantages of higher energy density and lighter weight [1–5, 52–56]. Life cycle, abuse tolerance, and cost are the next barriers to overcome for this technology. Most of the vehicle manufacturers that made publicly available EV/PHEV models in the market use Li-ion batteries.

As a summary, battery technologies are compared with different performance and cost characteristics in Table 1.2. This table is a result of a literature survey based on both battery cell manufacturers data sheets and individual cell tests [1–5] . As it is shown in Table 1.2, each different lithium-ion cathode composition cell has pros and cons, and they are still under development.

Table 1.2: Different battery cell comparison [1–5].

Battery type	Specific power (W/kg)	Specific energy (Wh/kg)	Cost	Safety	Life Calendar	Life Cycle (deep)	Manufacturer
Lead-acid	Low	Low	Very low	Proven	Low	Low	Many
NiMH	Moderate	Moderate	Moderate	Proven	Good	Good	Many
Li-ion LCO	Good	Good-excellent	High	Low	Low	Poor	Many, mostly consumer electr.
Li-ion LFP	Good-excellent	Good	Low	Excellent	Good	Good	A123, Valence, and Gaia.
Li-ion NCA	Good-excellent	Good-excellent	Moderate	Low	Good	Good	Toyota, Johnson Controls-Saft
Li-ion NMC	Good	Good-excellent	Moderate	Moderate	Moderate	Poor	Hitachi, Panasonic, Sanyo
Li-ion LMS	Moderate	Good	Moderate	Moderate	Moderate	Poor	GS Yuasa, LG Chem, Samsung

1.4 Discussion and Definition of PEV Battery Charging

This section describes the important battery, charger, and charging terminologies and definitions that are used throughout this study.

1.4.1 Battery and charging definitions

State of charge

In order to predict how many driving miles are left for the electric mode in a PEV, one needs to interpret the fuel gauge of the battery. SOC is the gauge that is used to understand the amount of charge which is proportional to the amount of energy that can propel the vehicle with only electric power. It is analogous to the fuel gauge that is used to show how much gas is left in the tank in an ICE vehicle.

There are different methods used to determine the electrical energy that exists in the chemical bonds of the battery. One simple and efficient method is to measure the current, thereby charge, entering and leaving the battery which is called coulomb counting. Based on this method, SOC can be found using Eq. 1.1:

$$SOC = \frac{Q_0 \pm \int i_{bt} dt}{Q_n} \times 100 \tag{1.1}$$

where Q_o is the initial electric charge present before charging/discharging the battery [C], Q_n is the nominal electric charge capacity of the battery [C], and i_{bt} is the battery current [A]. i_{bt} can be either negative or positive depending on the current direction. If the current is entering the battery, SOC will increase and vice versa. As shown in Eq. 1.1, SOC is a normalized value that is written in percentage for easier readability of the battery gauge.

State of discharge

Another definition is also used to measure the discharge state of the battery, state of discharge (SOD). It stands for the complement to SOC, meaning that it describes how much electricity has been taken out of the battery. Therefore SOC and SOD always sum to one. Mathematically, it follows as:

$$SOD = 1 - SOC \tag{1.2}$$

SOD is also termed as depth of discharge (DOD) which corresponds to the same definition.

State of health

A method of assessment to determine the condition of the battery cell is called state of health (SOH). It measures the condition of the battery to determine if battery operates above its factory guaranteed operating conditions. It is a relative measurement to the brand new battery cell. However, there is no direct method of assessing SOH like SOC. Rather, the history on the usage of battery is recorded in battery management system (BMS) to derive representation of SOH. The function of the BMS will be explained later.

Charging rate

Every individual battery cell has a charging current rate as a default manufacturer value. This is often termed as “C-rate”. C stands for the rated charge current of the battery cell that will fully charge the battery in one hour. All the charging currents are often referred to the rated current using the C rate such that $n \times C$ is a charge rate equal to the n times the rated charging current where n is a real number. For instance, $0.1C$ charging rate means the charging current is 10% of the rated charging current of the battery cell. As n increases, the charging time required to fully charge the battery cell decreases and vice versa.

1.4.2 Charging profiles

The common charging profiles used in the industry for lithium-ion (Li-ion) batteries are constant current (CC) and constant voltage (CV) charging. During CC charging, the current is regulated at a constant value until the battery cell voltage reaches a certain voltage level. Then, the charging is switched to CV charging, and the battery is charged with a trickle current applied by a constant voltage. Lithium-ion batteries with a cathode composition being lithium-cobalt-oxide, which is mostly used in consumer applications, (cell phone, camera, mp3 players, etc) have the following charging profile shown in Fig. 1.3. These batteries have a maximum charging voltage of 4.2 V. One observation from the charging profile is that the battery cell requires around 50 min to finish CC charging phase starting from 0% SOC with 1C charging current. At the instant when the battery reaches 75% SOC, the charger switches from CC to CV charging. The CV charging takes around 2 h 40 min resulting in a total charge time of 3.5 h [10]. Therefore the charge time required to charge the battery cell up to 75% SOC is around 25% of the total charge time. In comparison, to cover only 25% SOC, the charger needs to charge for 75% of total charge time during CV charging. In comparison, Li-ion LFP batteries present a different charging profile compared to Li-ion LCO batteries because of the difference in the chemical structure. For LFP batteries, CC charging stage takes 75% of the total charging time whereas CV charging occupies 25% of the total charging time as shown in Fig. 1.4.

1.4.3 Charging levels in the U.S.

There are three charging levels based on the voltage and current ratings used to charge a vehicle battery: Level 1, Level 2, and dc fast charging. However, only Level 1 and Level 2 have been standardized [57]. DC charging, or previously known as Level 3

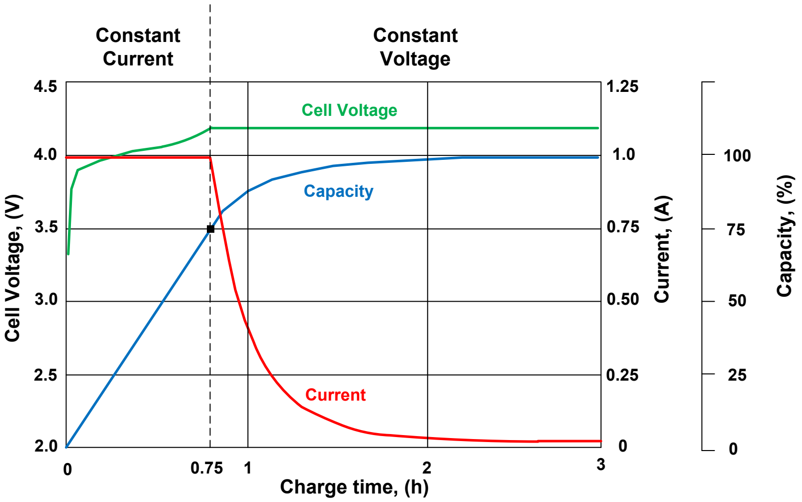

Figure 1.3: Li-ion LCO battery CC-CVcharging profile [10].

charging, is still under development [57]. Fig. 1.5 shows the map of the U.S. standard outlet receptacle ratings. There are different chargers; most of them are introduced in the next chapter, rated at Level 1, Level 2, or dc charging schemes.

Level 2 charging is much more preferred because of reduced charging time compared to Level 1 charging. This method employs standard 208-240 V ac single phase power outlet that has a continuous current rating less than 80 A [57]. For example, Nissan Leaf EV has a total of 8 h charging time using its 3.3 kW on-board charger to fully charge its 24 kWh depleted battery pack [31]. Also, it takes around 4 h to fully charge the depleted 16 kWh Chevrolet Volt PHEV battery [30].

Another charging method is fast charging or dc charging. At these charging stations, ac voltage is converted to dc off the vehicle and the vehicle is dc coupled to the charging station. Charging power can go up to higher values compared to the on board charging.Therefore, it will help vehicles to be charged in shorter amount of times. However, decreased battery lifetime is an issue because of the increased heat generation of the batteries at higher rates of current charging. As an example to decreased charging time for this type of station, Nissan Leaf EV will be charged with an off-board quick charge station in 30 min from a depleted SOC to 80% SOC [31].

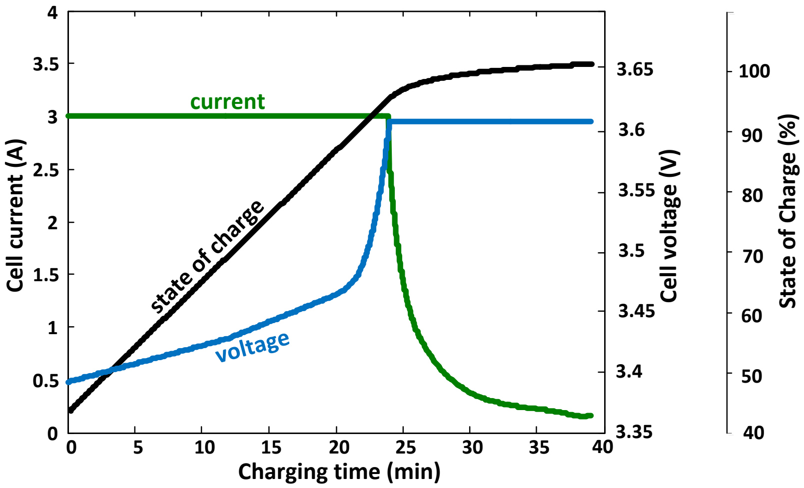

Figure 1.4: Li-ion LFP battery CC-CV charging profile.

1.4.4 Battery charging security and charging power quality

For lithium-ion batteries, the precautions in handling a secure battery operation are more important than other type of batteries. Since they are prone to failure in harsh working conditions, it is mandatory to have the utmost protection in vehicle applications both for customer and expensive battery safety point of views. Therefore, battery manufacturers also sell battery management systems, BMS for short, with added price to the battery cost. BMS is responsible for overseeing safety in charging and discharging operation. The key protection goals for Li-ion batteries include over-voltage, deep discharge, shutting-off in case of over temperature, shutting-off in case of over-current, and individual cell charge balancing [52, 58]. Especially for inrush current conditions, the BMS needs tight regulation not to allow any overcharging current entering the battery cells. BMS should also perform SOC and SOH determination, history (log book) function, and communication with other system components such as charger, grid, and the motor drive.

Since the battery manufacturer is responsible for the BMS, the charger only sends power to the battery pack where the BMS is also included. However, there is another issue that can cause problem for the battery cells related to the operation of the charger. This is the quality of the waveform of the dc voltage output of the battery

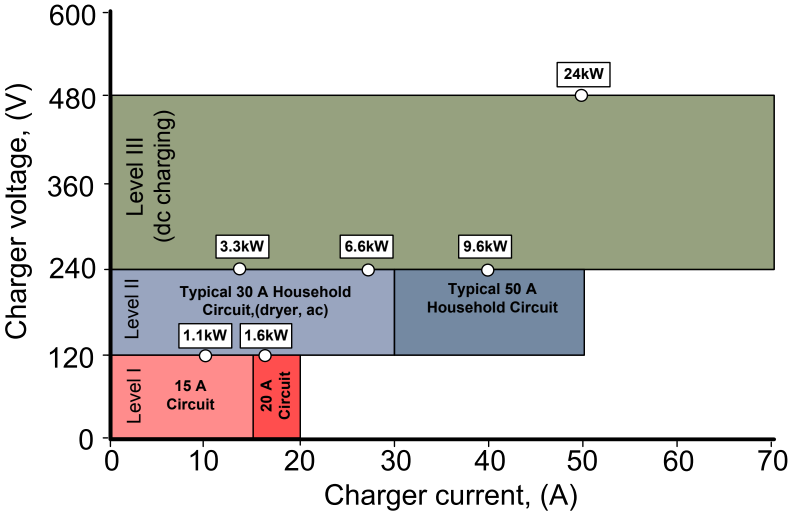

Figure 1.5: Charging outlet circuit breaker map with respect to receptacle voltage and current ratings [11].

charger. The chargers' output voltage waveform must be well regulated. In other words, the low/high frequency components present at the output voltage must be less than the maximum allowed voltage ripple harmonics to protect the health, and thereby the lifetime of the battery.

Currently, there is not much information about the effects of ripples on lifetime of the Li-ion batteries in the literature. It is difficult to find direct impacts of the ripple on the battery especially considering that each different Li-ion technology has different structures. However, there is a mature experience about lead-acid batteries in the literature and in the market [6, 59–67]. Hence, this experience can give the designer of the charger an idea about the limits on voltage and also current ripples.

Battery manufacturers give ripple limits to which a battery can be exposed. Table 1.3 summarizes the ripple limits taken from different manufacturers for lead-acid valve-regulated lead-acid (VRLA) batteries. The design of the charger should be optimized by selecting correct inductance, capacitance, switching frequency, and feedback compensator values to meet these requirements.

In order to understand the adverse effects of ripple on batteries in general, one needs to know how the ripple current converts to extra heat. A typical single-phase

Table 1.3: Different battery manufacturer limits for charging current and voltage ripple [6].

Manufacturer	Battery type	Voltage ripple	Current ripple
Yuasa	Lead-acid	N/A	C/10
Dynasty, Johnson Controls	Lead-acid	1.5% rms and 4% peak-peak	N/A
C&D Tech	Lead-acid	N/A	C/20

charger output voltage has two main ripple frequencies: one is at the second harmonic with respect to grid frequency, and the other is at the converter switching frequency. Assuming a simple battery model shown in Fig. 1.6, the extra ripple current will convert into extra heat due to the internal resistance of the battery pack, R_i in Fig. 1.6.

To calculate the total ripple current, the ripple output voltage of the charger at the specified frequency must be known. For example, the ripple current at a specified frequency can be related to the ripple voltage and the internal resistance by the equation:

$$I_{bt-ripple} = \frac{V_{bt-ripple}}{R_i} \tag{1.3}$$

where R_i is the equivalent internal resistance of the battery pack [Ω], $V_{bt-ripple}$ is the voltage ripple root mean square (rms) value present in the charger dc output voltage [V], and $I_{bt-ripple}$ is the ripple rms current value present in the battery charging current

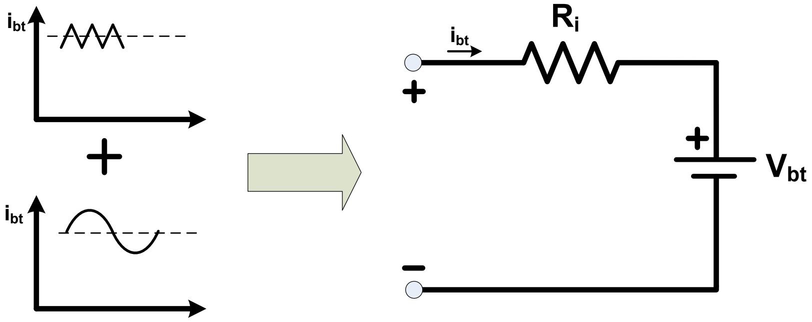

Figure 1.6: A simple equivalent circuit of the battery pack.

[A]. However, the internal resistance is not constant in different frequencies, and it decreases as the frequency of the ripple current increases. Assuming that each cell has the same internal resistance, and this resistance is the worst case resistance measured at the low frequency ripple current, the added dissipated power because of the total ripple becomes equal to:

$$P_{loss} = I^2_{bt-ripple-total} \times R_i \tag{1.4}$$

where $I_{bt-ripple-total}$ is the rms sum of the ripple currents at different frequencies. It is important to note that R_i also changes dynamically with different rms current values and temperature. Temperature increase should be limited by controlling this extra current. To show the effect of temperature increase on batteries, some of the derived assumptions about lead-acid batteries in the literature are: 1) a temperature increase of about 7-10 °C causes half of the lifetime of the battery to vanish [59, 61], 2) each degree C rise in battery temperature can decrease calendar life by 10% [6], 3) maximum allowable temperature increase should be around 3-5 °C, and 4) corruption and wear in the battery can also cause capacity loss [60].

In conclusion, the charger design procedure should include the battery ripple restrictions into account to reduce the extra heat dissipation in the battery cell. Therefore, the output voltage of the battery charger must be limited in its ripple voltage magnitude both in second harmonic ripple and in converter switching frequency ripple. Due to the electro-chemical process in the battery, the lower frequency ripple current will cause more heat dissipation compared to a higher frequency ripple current that has the same rms value.

1.4.5 Grid Connection Power Quality

One of the important requirements of an EV/PHEV charger is the amount of current distortion that it draws from the grid. The harmonic currents need to be well regulated not to cause excess heat which decreases the distribution transformer lifetime. Therefore, if this distortion is not limited, it can pose a threat on the utility grid. There are two definitions to measure the harmonic content of the battery charger current. The first parameter is THD is defined as follows.

$$THD = \frac{I_{c,h}}{I_{c,1}} \tag{1.5}$$

where $I_{c,h}$ is the rms sum of the harmonics (usually up to n=39) of the charger current [A], i.e. $I_{c,h} = \sqrt{\sum_{n=2}^{39} {I_{c,n}}^2}$ and $I_{c,1}$ is the rms fundamental (60 Hz) component of the charger current [A]. However, this definition is not enough to account for all charging currents of a charger. When there is a need to control the charger input current to help reduce the demand from the grid, the rms charger current may need to be reduced to less than 50% of the rated current. As loading on the grid decreases, the harmonic content of the charger current is not as disturbing to the grid as when the loading is high. In such cases, total harmonic distortion (THD) does not reflect the real impact of the harmonic content of the charger on the grid. Therefore, total demand distortion (TDD) can be used to accurately evaluate the harmonic content of the charger between 0 – 100% loading range. The definition of the TDD is shown in (1.6).

$$TDD = \frac{I_{c,h}}{I_{c,1,rated}} \tag{1.6}$$

where $I_{c,1,rated}$ is the rated fundamental current of the charger [A]. The only difference between TDD and THD is the change in the denominator. TDD is equal to THD when charging occurs at the rated current, i.e. $I_{c,1} = I_{c,1,rated}$. Table 1.4 lists the limits for the harmonic content of the single-phase chargers operating either as a load or as a distributed generator based on the limits shown in [7, 8]. It is important to note that the charger should meet the individual harmonic limits as well as the TDD limit which are calculated separately, i.e. $I_{c,3}/I_{c,1,rated}$ <4.0%, $I_{c,13}/I_{c,1,rated}$ <2.0%, etc. and TDD<5% using (1.6).

Table 1.4: Maximum Harmonic Current Distortion for Single-phase On-board Bidirectional Chargers [7,8].

Individual harmonic order	Max. distortion in percent of $I_{c,1,rated}$	
	Odd harmonics	Even harmonics[a]
h<11	4.0	1.0
11≤h<17	2.0	0.5
17≤h<23	1.5	0.375
23≤h<35	0.6	0.15
35≤h	0.3	0.075
TDD	5.0	1.25

[a] Even harmonic limits are 25% of the odd harmonics

1.5 Why V2G Reactive Power Support?

A potential benefit of PEVs is the ability to maintain the reliable operation of the grid by coordination between the vehicle and the utility. There are various services that PEVs can supply to the grid. Since every PEV has a charger that can convert ac to dc, this charger can be developed so that it can also send power back to grid for V2G operation. Based on the specific service provided, the utility can benefit by using a considerable amount of energy storage at the distribution system level. Coupled with this, the design of the charger can alleviate some of the problems that the utility are concerned with the integration of PEVs. These issues are listed below.

First, reactive power consumed at the load side are transmitted from the energy source to the load through the transmission and distribution system. This causes increased energy losses and decreases the system efficiency. With on-site generation of reactive power, the amount of reactive power that need to be transmitted from the generation side will decrease.

A recent DOE report predicts that the annual sales of EVs and PHEVs combined can reach up to 300 thousand vehicles by the year 2035 [13]. Another study claims that the annual sales of EVs and PHEVs combined would reach up to 500 thousand by the year 2020 with more than a cumulative of 2.5 million of them on the road [68]. The PEV charging is one of the primary concerns of smart grid applications due to its effect on power generation, transmission, and distribution when the large scale of PEV load is considered. While the requirement for more power generation will be a concern with an increased number of PEVs, the distribution system level issues raise more questions. Several studies look at the effect of PEV charging at distribution system level. Studies show that depending on the number of PEVs connected, the rating of the chargers in those PEVs, size of the energy storage, rating of the distribution transformer (25-100 kVA), harmonic content of the charging current, geographical location, and if any charging management control is employed, the lifetime of the distribution transformer may reduce down to its 30% of regular life expectancy [69, 70]. To prevent such problems on the distribution system, the utilities must build infrastructure to enable smart grid incentives like variable rates, smart meters, grid communications, and distributed energy management.

A regular microwave oven consumes up to 0.5 kVAR and a washing machine consumes up to 0.8 kVAR of reactive power. Other loads of reactive power in a residential house include air conditioner, dishwasher, and refrigerator, etc. Although appliances consume reactive power, the customers are not billed for the reactive power they use. Instead, utility pays for the reactive power for residential customers. However, with increased number of PEV connection and the aforementioned issues of transformers makes the on-site generation of reactive power an important add-on value. Therefore, generating V2G reactive power will help the utility by providing increased efficiency of power transfer through transmission lines and decreasing overloading of transformers

Consequently, of utmost importance is the need to regulate PEV - grid interaction. The design of the battery charger will be crucial in this effort to effectively control the power flow and, as a result, maintain continuous service of efficient electrical energy supply.

1.6 Proposed Study

This study first proposes an analysis and experimental verification of the effect of reactive power operation on the design and operation of a single-phase on-board bidirectional charger. The topology consists of two stages, an ac-dc converter and a dc-dc converter. The operation modes that are of interest are PFC unidirectional charging operation, charging and reactive power operation, and full-reactive power operation. The main effect of the reactive power operation is observed on the operation of dc-link capacitor. Its peak-peak voltage ripple, and low frequency current ripple affects the selection of the electrolytic capacitors and operation of the charger. Furthermore, the effect of reactive power operation on the battery charging operation is also summarized.

Second, the study also proposes a novel control system for PQ command following of the bidirectional charger. It contributes to the literature of the reactive power support operation of on-board bidirectional chargers by proposing a variable dc-link voltage control that helps to generate a reference dc current for battery charging. The study experimentally shows the verification of the proposed controller.

Finally, the incremental and operating costs of reactive power are summarized and compared with other options of reactive power supply. The net cost penalty of the charger for two different customer cases are calculated.

1.7 Outline of the Dissertation

The dissertation is organized into seven chapters. The first chapter is background information on alternative vehicles, their energy storage, and grid connected charging. It elaborates on the vehicle types with grid chargeable batteries; namely, EVs and PHEVs. Then it describes the battery technology that is used in current grid-connected vehicles and presents the important definitions and subjects related to vehicle battery charging. Chapter 2 is concerned with the classification and comparison of all the different battery charging devices that have been used in the market. It highlights the power electronics topology structure of different chargers. Chapter 3 presents the analysis of reactive power operation using single-phase bidirectional chargers. It summarizes the effect of reactive power operation on different components of the charger. Chapter 4 describes the simulation study of the system. Chapter 5 describes the design of the system and implementation of the controller. Chapter 6 evaluates the cost of reactive power operation for different charger and customer profiles. Chapter 7 concludes the study.

Chapter 2

Literature Survey of PHEV/EV Battery Chargers and V2G Power Transfer

2.1 Discussion and Classification of Battery Chargers

Since the inception of the first EVs, there have been many different charging systems proposed. The chargers can be classified based on the circuit topologies (dedicated or integrated), location of the charger (either on or off the vehicle), connection (conductive, inductive/wireless, and mechanical), electrical waveform (dc or ac), and the direction of power flow (unidirectional or bidirectional) as listed in Table 2.1. More on this classification can be found in [32].

There is not a single charging method that will fulfill all the customer expectations. It will most likely be a combination of different methods that will maximize the charging availability of a PEV. Among the noteworthy chargers of the industry and literature which initially attracted the attention of several number of vehicle manufacturers, are dedicated, on-board, conductive, ac, and unidirectional chargers.

Table 2.1: Charger classification chart.

Classification type	Options
Topology	Dedicated or Integrated
Location	On-board or Off-board
Connection type	Conductive, Inductive, or Mechanical
Electrical waveform	AC or DC
Direction of power flow	Unidirectional or Bidirectional

However, there is a great potential to further develop the topologies and make the charger design more advanced with functions for future smart grid applications such as V2G support. In the next section, the literature will be presented in the framework of V2G support.

2.2 PHEV/EV Charger Power Electronics and Configurations

The focus of this section is to analyze the available topologies applicable for on-board conductive bidirectional power transfer operation. Bidirectional power transfer means that the active power can either be transferred from the utility to the vehicle (charging) or from the vehicle battery to the grid (discharging). The charger topologies investigated in this section are single-phase Level 1 and Level 2 compatible bidirectional chargers. Some other charger topologies including unidirectional topologies are also highlighted to compare with the surveyed bidirectional topologies.

There are basically two power conversion stages required to charge the battery using grid electricity: one is the alternating current (ac)-direct current (dc) rectification and the other is the dc-dc conversion as shown in Fig. 2.1. Each of these stages can be formed with many different passive and active component combinations (inductors, capacitors, and semiconductor switches). Any combination of the two aforementioned stages will result in a different topology. Rather than giving different

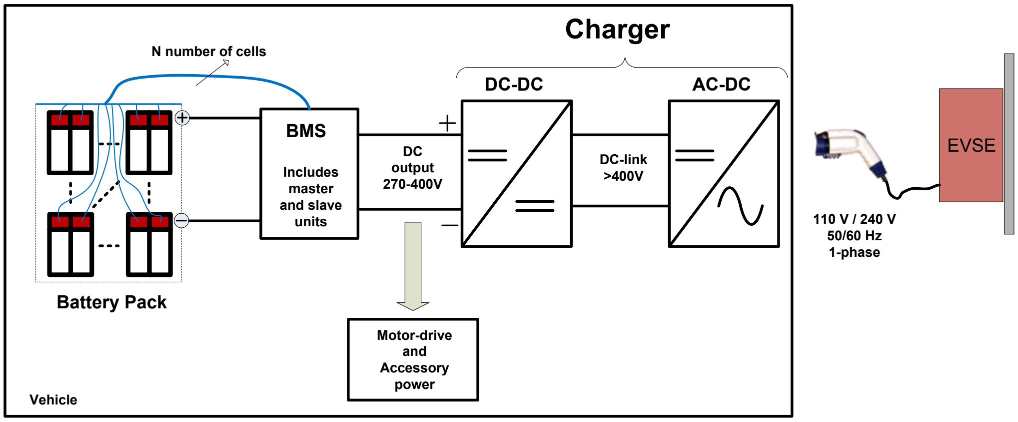

Figure 2.1: Schematic of an on-board charger with other charging components.

available ac-dc power conversion circuits, only the ones that are found promising in the literature to be used with on-board Level 1 and Level 2 charging are listed here.

The discussion includes single-phase Level 1 and Level 2 chargers. Off-board dc fast charging topologies can be analogous to the ones discussed here. However, this charging level employs a three-phase system. Therefore, it will require increased number of component and higher ratings for the devices.

As shown in chapter 1, the common nominal battery voltage levels in PHEVs and EVs that are in the market, are in between 300 V- 400 V. The terminal voltage levels of PHEVs/EVs are higher than HEVs mainly because of increased power requirement from the battery. Higher terminal voltages will allow for smaller cabling size and considerably decrease the current ratings of active and passive devices for a given power level. Due to high battery voltage and a 120 V/240 V grid connection, a boost rectification stage is preferred over a buck rectification stage to prevent an unnecessarily high conversion ratio between the dc link and the battery terminals.

A charger can be configured in two different ways in terms of its active and reactive power transfer capability with the utility grid as shown in Table 2.2. The first option is the PFC unidirectional charger that is mostly in use in todays PHEVs and EVs. Its operation boundary is shown in Fig. 2.2a as the red line on the positive power axis of the P-Q power plane. This charger operates close to unity power factor

Table 2.2: Different types of chargers based on power transfer operation.

Charger type	Active power direction	Reactive power direction
Power factor-corrected unidirectional	Grid-to-vehicle charging	Zero
Four-quadrant bidirectional	Grid-to-vehicle charging or Vehicle-to-grid discharging	Inductive or capacitive

and only allows controlling the active power used to charge the battery. Therefore, it operates only on the positive x-axis of the P-Q power plane. Second, the four-quadrant bidirectional charger operates in the full circle shown in Fig. 2.2b. All of the charger types have a maximum power limitation marked as P_{max} and Q_{max}, which are defined by the charger apparent power rating and the outlet power rating that the charger gets power from.

The following section will present an overview of the power electronics topology of the charger types listed in Table 2.2. The topologies listed here in the next section only include ac-dc rectification. The dc-dc conversion circuits are separately explained later in this chapter in section 2.2.3

2.2.1 Power Factor-Corrected Unidirectional Chargers

PFC unidirectional chargers only transmit power from the utility to the vehicle battery and operate with almost unity input power factor. In other words, they are not designed to exchange reactive power with the grid. Today, all of the PHEV and EV manufacturers that are in the market use this type of charger. Some of the ac-dc rectification stages are highlighted in the next sections.

Conventional AC-DC Boost Converter

In this topology, a front-end diode bridge is used to rectify the input voltage, and it is followed by a boost section as shown in Fig. 2.3. This topology is widespread for low power applications. Due to conduction losses of the diode-bridge, it is not well suited for power levels higher than 1 kW [22, 71]. Another problem is the design of the dc

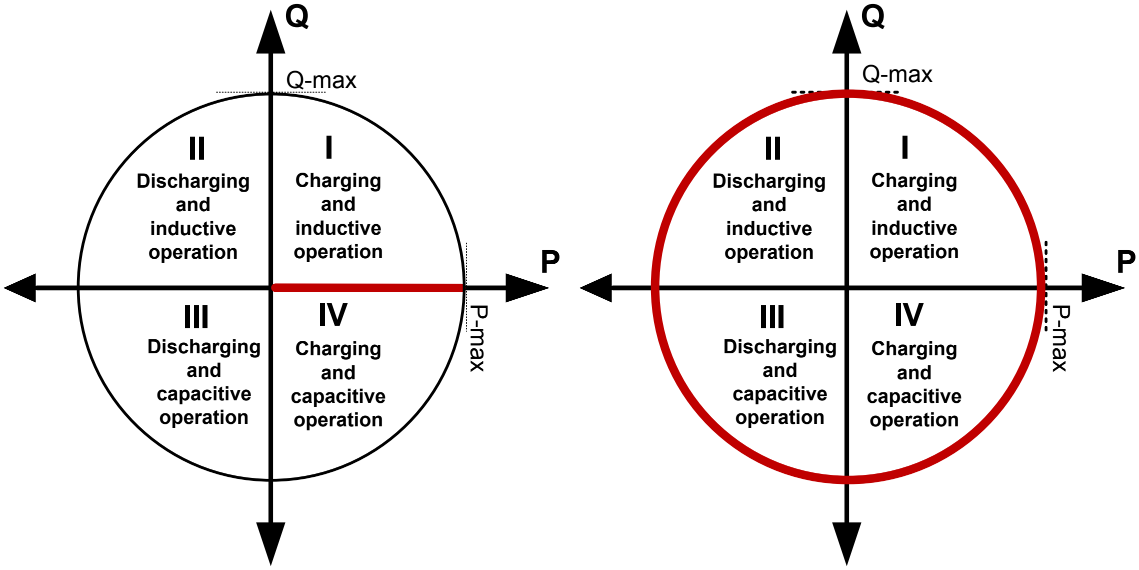

(a) Power factor-corrected unidirectional charger operation **(b)** Four-quadrant bidirectional charger operation

Figure 2.2: Operation regions of different chargers shown in red in P-Q power plane.

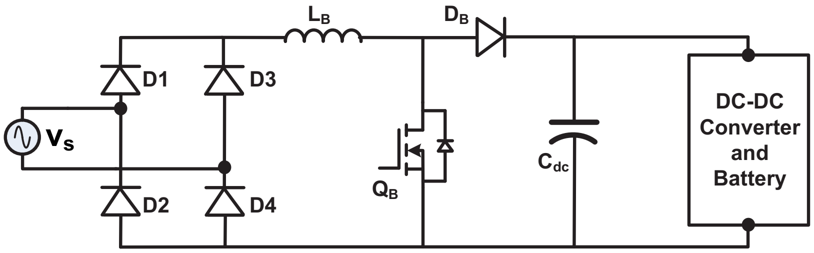

Figure 2.3: Conventional ac-dc boost converter.

inductor at high power levels. As a solution to this problem, interleaving techniques are proposed as shown in the next section.

Interleaved AC-DC Boost Converter

Interleaving the boost section of the conventional PFC is first introduced in [72] and shown in Fig. 2.4. The main advantage of this topology is decreased high frequency PWM rectifier input current ripple caused by the switching action. Reducing input ripple decreases the required switching frequency to meet a current TDD limit imposed by the utility. Reducing PWM input ripple current also decreases the ac ripple current supplied by the dc link capacitor, thereby reducing its stress. Another advantage is the reduced current rating of the active switches as the interleaving converter halves the input current. One disadvantage of the topology is the high conduction losses of the input bridge rectifier as well as increased number of semiconductor devices and associated gate control circuitry. This topology is preferred by the industry for on-board charging applications and is used for 3.3 kW Level 2 chargers [73, 74].

Bridgeless AC-DC Boost Converters

This converter type eliminates the input diode-bridge to attain higher efficiencies at increased power levels at the expense of using a higher number of active switches, and increased control and sensing circuit complexity. The topology proposed in [75] is called symmetrical bridgeless boost rectifier and is shown in Fig. 2.5. Another topology called asymmetrical bridgeless boost rectifier is proposed in [76] and is shown in Fig. 2.6.

Discussion

Although power factor-corrected unidirectional chargers are mostly suited for high power factor applications, they can still be used for reactive power compensation with certain limits. However, there are two main disadvantages of this operation. First, reactive power operation can only be achieved by natural commutation of current through the diodes. This poses a strict limit on the amount of phase difference

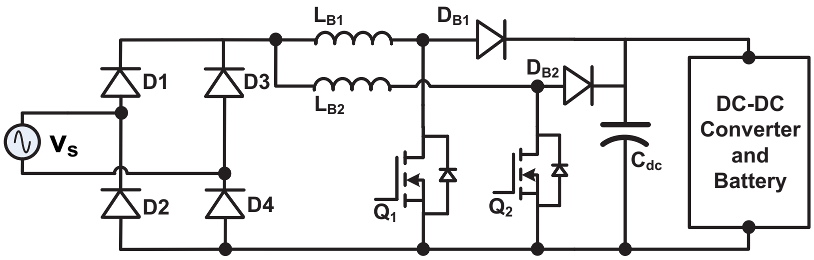

Figure 2.4: Interleaved ac-dc boost converter.

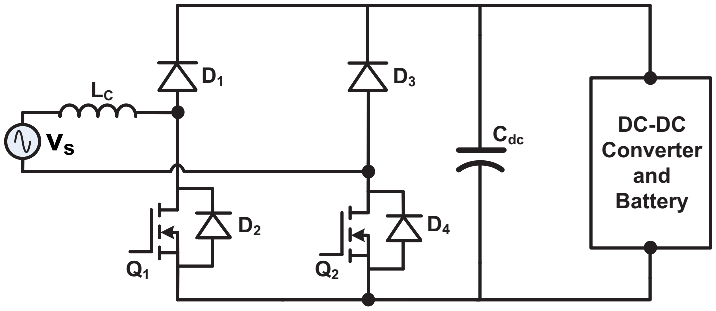

Figure 2.5: Symmetrical bridgeless boost rectifier.

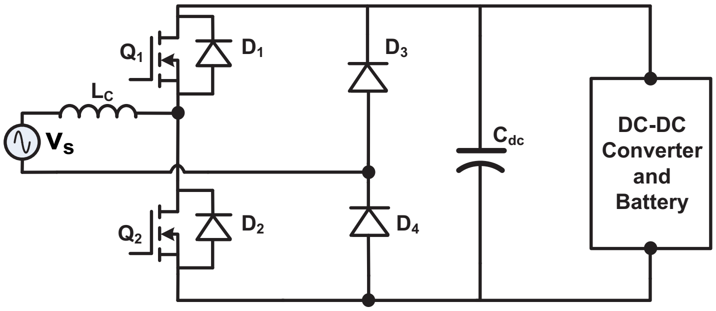

Figure 2.6: Asymmetrical bridgeless boost rectifier.

that can be introduced between the grid voltage and grid current depending on the inductance value of the boost inductor. Otherwise, the current THD exceeds the allowed limit by the utility. For instance, the application given in [77] has only a maximum of 14% reactive power operation range compared to full power rating of the charger. A second disadvantage is that the charger must always be charging the battery in order to supply reactive power to the grid. In other words, if the battery has full SOC, reactive power operation is not possible. Considering these two limitations, power factor-corrected unidirectional chargers are not promising compared to other type of topologies for reactive power operation. The following sections describe the suitable topologies for this type of application.

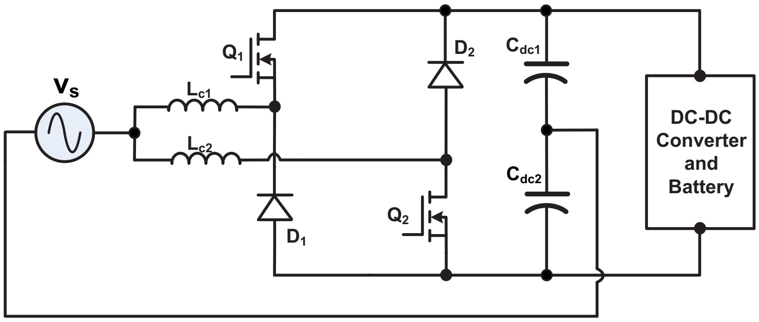

Figure 2.7: Dual-buck ac-dc half-bridge converter.

2.2.2 Four-quadrant Bidirectional Chargers

Dual-buck AC-DC Half Bridge Converter

A dual-buck ac-dc half bridge converter shown in Fig. 2.7 was first introduced in [78] and also employed for a battery storage system to demonstrate four-quadrant operation capability with increased efficiency [79]. By placing the two active semiconductor switches in a diagonal structure rather than symmetrical/asymmetrical structure, four-quadrant operation is achieved. The circuit does not need shoot through protection as there are no active switches connected in series. The circuit requires two split dc-link capacitors and two input inductors.

Conventional AC-DC Half Bridge Converter

This type of converter diagram is illustrated in Fig. 2.8. It includes two dc link capacitors, two switches, two diodes, and a coupling inductor for grid interconnection. Two sufficiently large capacitors share the dc link voltage equally. The switches Q_1 and Q_2 cannot be on at the same time to prevent any short circuit or shoot through. This requires a dead time when the switches are operated sequentially. When the switch Q_1 is on, either Q_1 or D_1 conducts depending on the direction of the charger current. Similarly, when the switch Q_2 is on, either Q_2 or D_2 conducts depending on the current direction. The topology is suitable to transfer power in four quadrants.

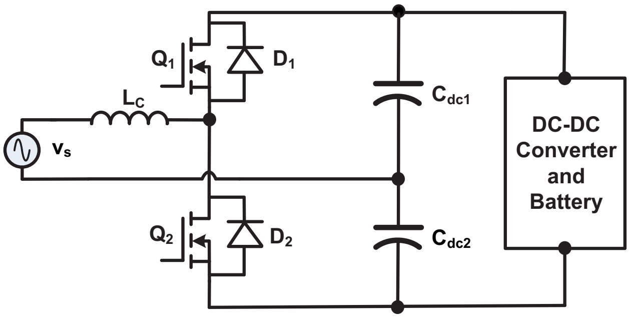

Figure 2.8: AC-DC half bridge converter diagram.

A half bridge converter requires bipolar switching because there are only two possible output voltage levels, $+V_{dc}$ and $-V_{dc}$.

AC-DC Full Bridge Converter

The full bridge converter, shown in Fig. 2.9, is comprised of a dc link capacitor, four transistors (either MOSFETs or IGBTs), four diodes, and a coupling inductor. Voltage of the capacitor is doubled in this configuration. The topology is suitable for four quadrant operation.

The full-bridge converter can operate in unipolar modulation and has three output voltage levels; $+V_{dc}$, $-V_{dc}$, and zero. Since there are three output voltage levels for the full bridge inverter, the number of switchings required for the same current THD level is effectively reduced with the full-bridge converter compared to half-bridge converter.

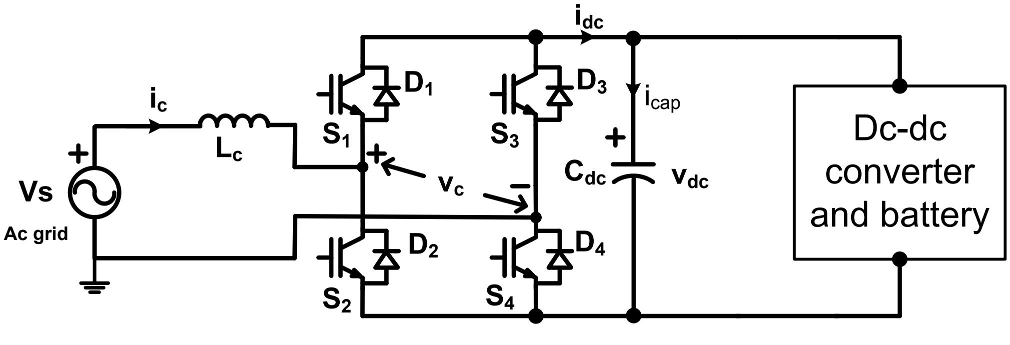

Figure 2.9: AC-DC full bridge converter diagram.

2.2.3 DC-DC Converter Stage

The fundamental bidirectional dc-dc converters are explained in this section. The two dc-dc converters under discussion are half bridge bidirectional dc-dc converter and dual active bridge bidirectional dc-dc converter.

Half Bridge Bidirectional DC-DC Converter

This converter has two transistors (IGBT or MOSFET), two diodes, a filtering capacitor and an inductor as shown in Fig. 2.10. It can transfer power in both directions. However, it can only operate as a buck converter in one direction and as boost converter in the opposite direction as illustrated in Fig. 2.11.

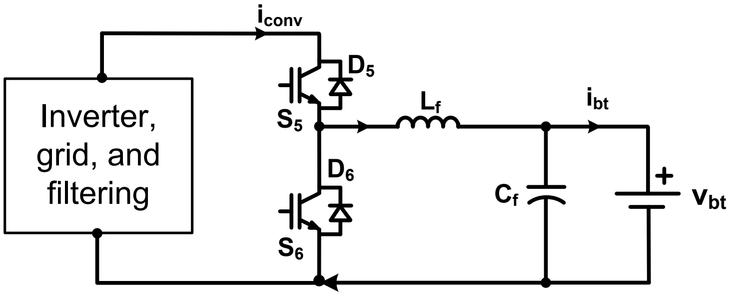

Figure 2.10: Half bridge bidirectional dc-dc converter diagram.

The bidirectional operation of the charger requires a higher dc link voltage value than the peak value of the line voltage to keep the modulation index of the inverter less than one. This is also required for sinusoidal charger current. Therefore, the dc link voltage is usually required to be higher than 350 V for a 240 V grid connection. For increased control stability, the minimum dc link voltage should be selected to be at least 400 V. This value is higher than the regular battery pack voltage which is at 200 V - 390 V level. Therefore, the operation of the dc-dc converter is one way buck (from dc link to battery) and one way boost (from battery to the dc link).

Switches S5 and D6 operate during buck operation when the energy is transferred from dc bus to battery, i.e. charging operation. During this operation, S6 is turned off. In contrast, when battery is being discharged switch S6 and D5 operate and S5 is turned off. One disadvantage of this converter is the lack of electrical isolation of the battery from the dc link and the grid.

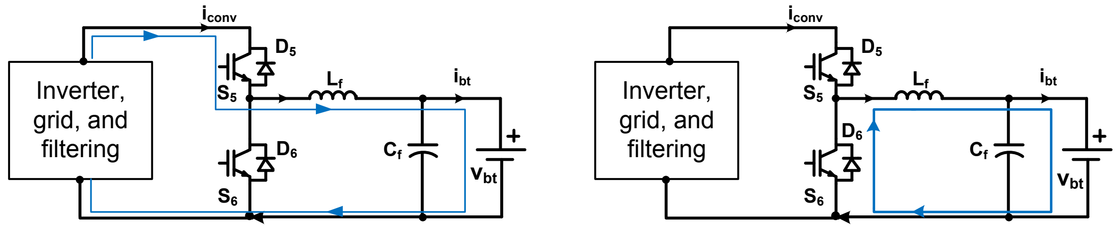

(a) Buck mode with S5 operating. **(b)** Buck mode with D6 operating.

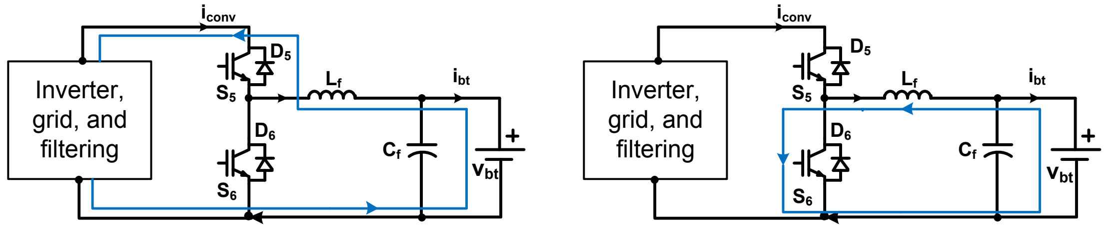

(c) Boost mode with D5 operating. **(d)** Boost mode with S6 operating.

Figure 2.11: Buck and boost mode of operation for the bidirectional dc-dc converter.

Dual Active Bridge Bidirectional DC-DC Converter

A dual active bridge dc-dc converter has the merits of providing isolation and a higher buck/boost ratio between the dc link voltage and the battery since it has a HF transformer. The configuration of the converter is demonstrated in Fig. 2.12. This converter requires much more increased number of components than the non-isolated topology: eight transistors (IGBT or MOSFET), eight diodes, an inductor, and a high frequency (HF) transformer. Therefore, it has a more complex control circuitry.

The first stage of the converter inverts the dc link voltage into ac voltage during battery charging. Then, the ac voltage is electrically isolated through an HF transformer. Last, the ac voltage again is rectified to appropriately charge the battery. The process is reversed when the battery has to discharge back to the grid.

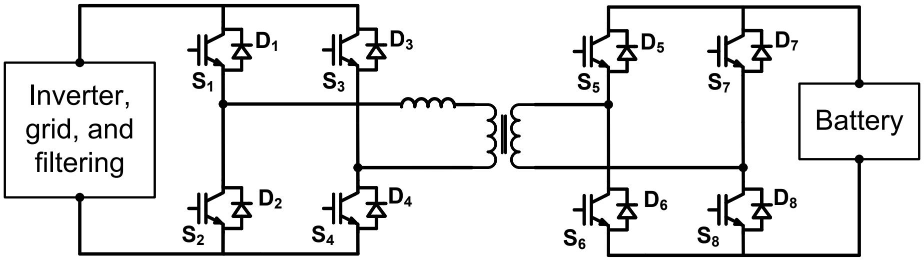

Figure 2.12: Dual active-bridge bidirectional dc-dc converter diagram.

This topology is only used if a very high voltage ratio or isolation is required between the dc link and the battery pack. Usually the conversion ratio between the dc link and the battery is not selected to be very high for charger applications. For increased safety of the users, auto manufacturers mandate the electrical isolation requirement between the high voltage battery and charging outlets that are connected to the grid.

2.2.4 Integrated Charger Topologies

The literature studies mostly focus on designing chargers with low volume, weight, and cost. Therefore, researchers have looked at partly/completely integrating the charger into the traction drive so that the size, cost, and volume of the charger can be reduced [12, 80–85]. What is more, utilizing the already available high power traction drive, the charging time can theoretically be reduced. While there are different topologies proposed, only the ones used in electric vehicle applications and published with enough technical details are discussed here.

ORNL Integrated Charger

One of the recent topologies developed at Oak Ridge National Laboratory (ORNL) shows the performance of an integrated charger described in [12] and shown in Fig. 2.13. Here, authors utilize two inverters that are already present in a Toyota Prius HEV. The first inverter is an auxiliary inverter that is usually used for the air

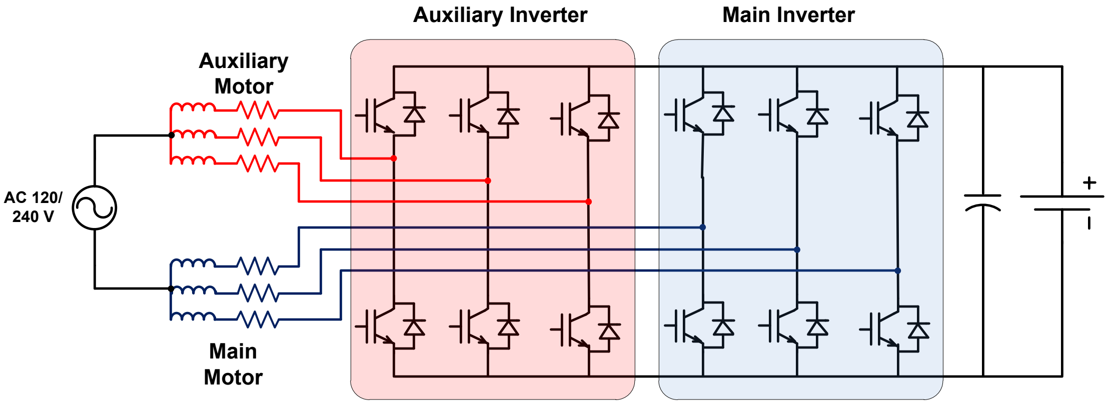

Figure 2.13: An integrated charger employing two inverters [12].

compressor drive motor, the water pump motor, or the generator in the vehicle. The main inverter is used to drive the motor. The auxiliary inverter is usually 1/3 of the main inverter in power rating size. Hence, only the main inverter is rated at high power level. By selecting a leg from the auxiliary inverter and another leg from the main inverter, and using the electrical machine inductance, the topology is converted to a single-phase charging circuit as shown in Fig. 2.13. This topology can only be realized using a Y-connected electrical machine.

Level 1 charging with 1.3 kW output charging power shows that the topology is 92.1% efficient, the line current THD is close to 12%, and input power factor is 0.98 [12]. Level 2 charging with 14.5 kW output charging power recorded an efficiency of 93.6%, and the current THD at that level is 6.60%.

Although this topology saves the extra charging circuit, it has several drawbacks. Because of the fixed inductance of the system, the selected switching frequency (15 kHz) is not enough to decrease the line current THD to acceptable levels (less than 5%). To further decrease the current THD, higher switching frequency will be required which will further increase the losses. Another disadvantage mentioned in the paper is the rating of the auxiliary inverter is much lower than the rating of the main inverter that would decrease the proposed fast charging time considerably. To avoid this, an extra diode leg is needed so that the auxiliary inverter will be bypassed as shown in Fig. 2.14. However, this solution will further decrease the equivalent

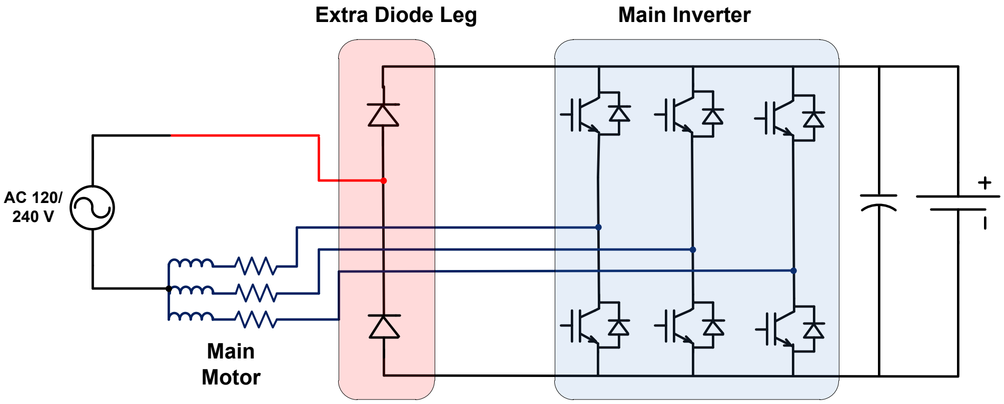

Figure 2.14: Solution to bypass the auxiliary inverter [12].

inductance of the system that will counteract the THD of the line current. Therefore, an external filter inductance is required for this topology to achieve acceptable line current THD values.

Although not mentioned in the study, the dc-dc converter is necessary to meet charging requirements of the battery. Without a dc-dc converter, due to the conventional power equation of the single-phase inverter, the battery will see a large voltage and current ripple. Therefore, to improve the safety and lifetime of the battery pack, a dc-dc converter is needed. Generally, traction drives such as the one used in the Toyota Prius HEV employ a dc-dc converter between the inverter and the battery. That dc-dc converter can also be employed for battery charging voltage and current regulation.

AC Propulsion Integrated Charger

Another topology that is used in the market is the integrated drive and charging system manufactured by AC Propulsion and shown in Fig. 2.15 [85]. This charger is rated from 200 W to 20 kW and can operate with either 120 V or 240 V outlets. Efficiency of the system for 1.44 kW with Level 1 charging is around 85% and it is around 95% for 14 kW input power with Level 2 charging [85]. The relays K1, K2, and K2′ are used to switch from motoring to charging mode and vice versa. In

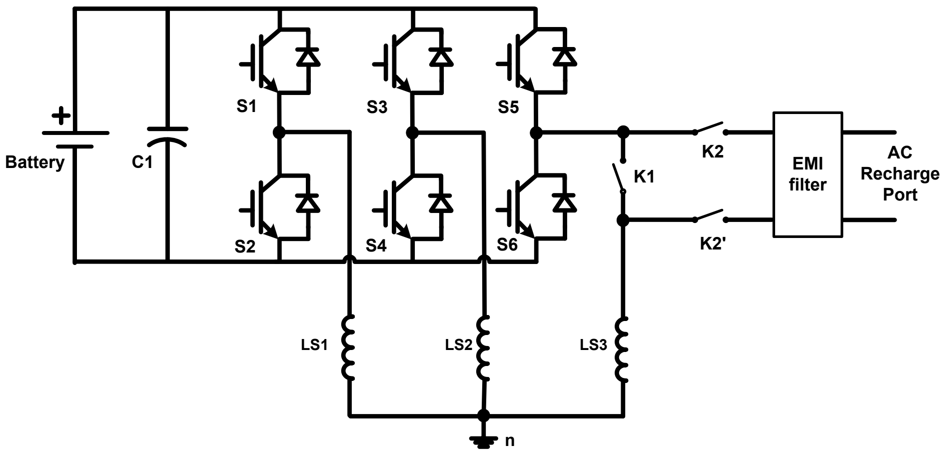

Figure 2.15: AC propulsion integrated charger [66].

traction mode, relay K1 is closed and K2 and K2′ are open. In charging mode, relays K2 and K2′ are closed and relay K1 is open. When charging, switches S1 and S2 are kept open, and switches S3-S6 operate to form a single phase full-bridge ac-dc converter. This system design does not employ a dc-dc converter, but it can be added if desired.

Partly Integrated Chargers

In addition to the above approaches, a charger can also partly share the circuitry with the drive-train. Rather than fully embedding the charger into the motor drive, it can only utilize the dc-dc converter already available in the drive-train. This approach is shown in Fig. 2.16. The advantage of this usage is the elimination of one extra dc-dc converter from the charger circuit. For example, Toyota Prius HEV uses a half bridge bidirectional dc-dc converter. Since this boost dc-dc converter is already rated at high power, it can also be used to charge the vehicle battery during charging operation. Moreover, already available large electrolytic capacitor can also be used to filter out second harmonic ripple due to the single-phase charging. The disadvantage of this approach is that the traction dc-dc converter is designed to be non-isolated due to the

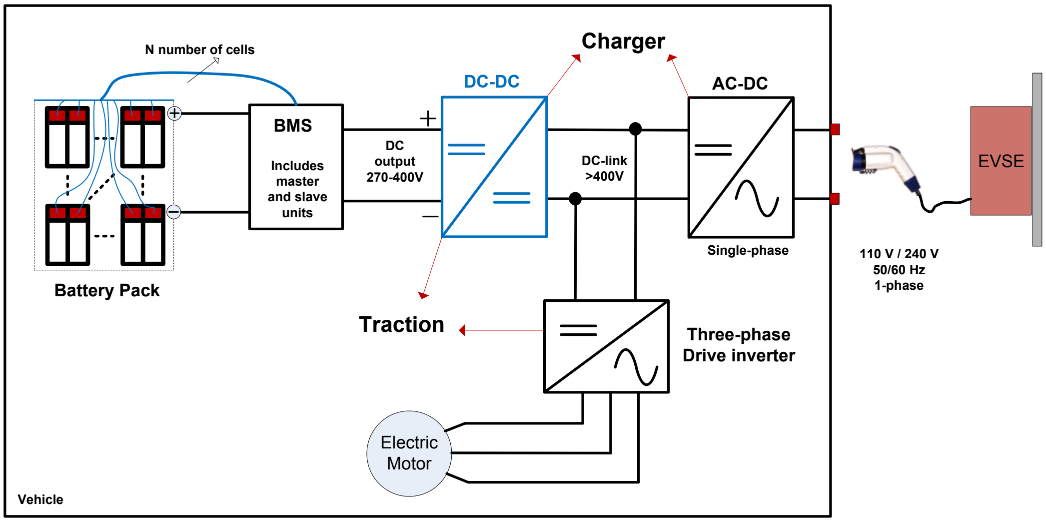

Figure 2.16: Partly integrated charger into the traction-drive.

efficiency and cost concerns. Using the same converter as a charger will only provide a non-isolated charging option.

2.3 Chapter Summary

This chapter presented a summary of power electronic circuit solutions for on-board charging operation. The chargers are classified into two categories in terms of the power transfer direction between the charger and the grid: PFC unidirectional charger and four-quadrant bidirectional charger. The available topologies for each of the categories are listed and their pros and cons are explained. Moreover, some of the integrated charger topologies proposed in the literature are added at the end of the chapter.

Chapter 3

Mathematical Analysis of Reactive Power Operation and its Effect on the Charger

3.1 Introduction

The purpose of this chapter is to first show the parameters of PFC operation of a charger to effectively fulfill the requirements of the charging operation that has been explained in the previous chapters. Second, the effect of reactive power operation (on a scale from full inductive operation to full capacitive operation) on different system parameters will be found and the net difference from the PFC operation will be summarized.

The system parameters that are under discussion are listed in Table 3.1 in page 52. The first three parameters (S, V_s, and f) are constant during the analysis. The other parameters (L_c, V_{dc}, ΔV_{dc}, C_{dc}, and I_{cap}) are selected as the basis of comparison for evaluating the effect of the reactive power operation on the charger. The results will show how the selection of these parameters changes while the charger goes into reactive power operation.

3.2 Analysis of single-phase power transfer between the utility grid and charger

The topology that is investigated in this chapter is a single-phase ac-dc converter for front-end conversion of ac energy into dc. An example of this type of topology, a full bridge bidirectional ac-dc converter is shown in Fig. 3.1. For a charger application it should also be followed by a dc-dc conversion stage. Normally, the inverter output voltage (the voltage difference between the points a and b shown in Fig. 3.1) has a PWM waveform shape. However, for the purpose of understanding the power flow operation in this single-phase system, initially we can ignore high frequency PWM ripple components of the waveforms.

The analysis in this chapter starts with a simplified diagram of the grid and the charger as shown in Fig. 3.2. The grid voltage, $v_s(t)$, is assumed to be purely sinusoidal. L_c is the coupling inductor which includes the charger boost inductor and the line inductance of the utility. For analysis purposes, the system has only one frequency component, both of the voltage sources are sinusoidal, and the current flow is designated positive for current flowing from the grid to the inverter, since the primary function of the circuit is to charge the battery from the grid. Therefore, positive power sign of active power (P_s), reactive power (Q_s), and apparent power (S) correspond to the power sent by the grid to the charger.

Since the system has only one frequency component, phasor analysis can be used to solve for the charger (line) current, $i_c(t)$.

$$\begin{aligned} v_s(t) &= \sqrt{2}\,V_s\,sin(\omega t) \\ &= \sqrt{2}\,V_s\,cos(\omega t - \frac{\pi}{2}) \qquad (3.1) \end{aligned}$$

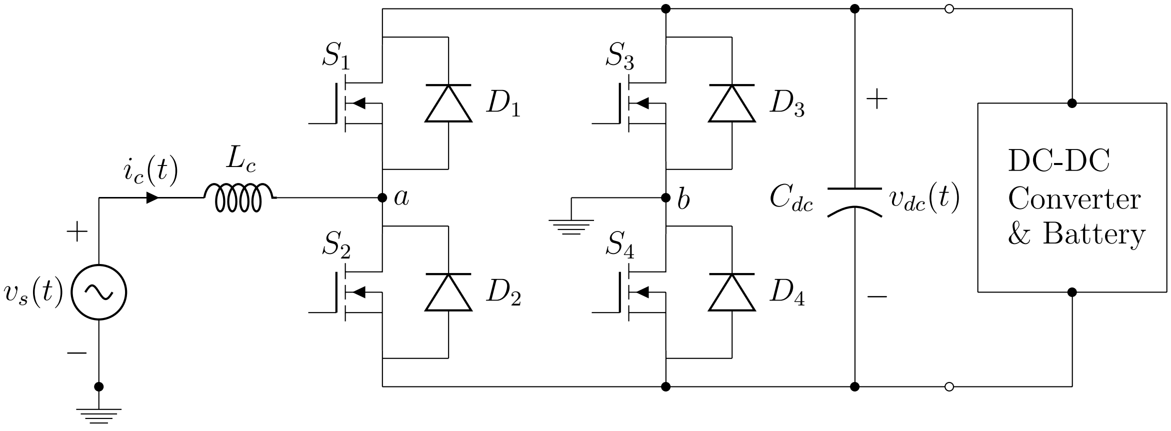

Figure 3.1: Full bridge bidirectional ac-dc converter.

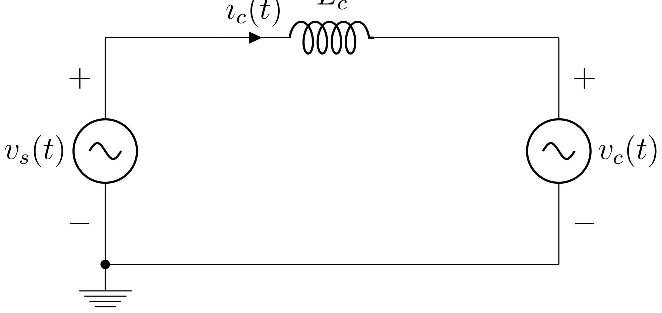

Figure 3.2: Equivalent circuit of the charger-grid connection.

Since, the default active power flow is from the grid to the charger, $v_c(t)$ is lagging $v_s(t)$ by δ degrees.

$$\begin{aligned} v_c(t) &= \sqrt{2}\,V_c\,sin(\omega t - \delta) \\ &= \sqrt{2}\,V_c\,cos(\omega t - \delta - \frac{\pi}{2}) \end{aligned} \tag{3.2}$$

and

$$\omega = 2\pi f \tag{3.3}$$

where V_s and V_c are the rms of the grid voltage and charger output voltage, respectively (V), f is the system frequency (Hz), and ω is the angular frequency (rad/s). Using the phasor notation, it can be written that:

$$\overline{V_s} = \sqrt{2}\, V_s\, e^{-j\frac{\pi}{2}} \tag{3.4}$$

$$\overline{V_c} = \sqrt{2}\, V_c\, e^{-j(\delta+\frac{\pi}{2})} \tag{3.5}$$

where $\overline{V_s}$ and $\overline{V_c}$ are phasor representation of the grid and charger voltage, respectively. The definition of the inductor voltage in phasor representation is as follows:

$$\overline{V_L} = j\omega\, L_c\, \overline{I_c} \tag{3.6}$$

where $\overline{I_c}$ is the phasor representation of the charger current (A). Using Kirchhoff's voltage law (KVL) for the equivalent circuit shown in Fig. 3.2 yields the following equation:

$$\overline{V_s} = \overline{V_L} + \overline{V_c} \tag{3.7}$$

Therefore, plugging (3.4), (3.5), and (3.6) into (3.7) yields the following derivation:

$$\begin{aligned}
\overline{I_c} &= \frac{\overline{V_s} - \overline{V_c}}{j\omega L_c} \\
&= \frac{\sqrt{2}}{j\omega L_c}\{V_s\, e^{-j\frac{\pi}{2}} - V_c\, e^{-j(\delta+\frac{\pi}{2})}\} \\
&= \frac{\sqrt{2}}{j\omega L_c}\{-jV_s - V_c\, cos(\delta + \frac{\pi}{2}) + jV_c\, sin(\delta + \frac{\pi}{2})\} \\
&= \frac{\sqrt{2}}{j\omega L_c}\{-jV_s + V_c\, sin(\delta) + jV_c\, cos(\delta)\} \\
&= \frac{\sqrt{2}}{j\omega L_c}\{V_c\, sin(\delta) + j(V_c\, cos(\delta) - V_s)\} \\
&= \frac{\sqrt{2}}{\omega L_c}\{V_c\, cos(\delta) - V_s - jV_c\, sin(\delta)\} \\
&= \sqrt{2} I_c\, e^{-j\alpha}
\end{aligned} \tag{3.8}$$

where

$$I_c = \frac{1}{\omega L_c}\sqrt{{V_c}^2 + {V_s}^2 - 2V_c\,V_s\,cos(\delta)} \tag{3.9}$$

and

$$\alpha = tan^{-1}\left(\frac{V_c\,sin(\delta)}{V_c\,cos(\delta) - V_s}\right) \tag{3.10}$$

Therefore,

$$i_c(t) = \sqrt{2}\,I_c\,cos(\omega t - \alpha) \tag{3.11}$$

Since the initial voltage waveforms are in the form of a sinusoid, the charger current is written in sinusoidal form for consistency. Therefore:

$$i_c(t) = \sqrt{2}\,I_c\,sin(\omega t - \alpha + \frac{\pi}{2}) \tag{3.12}$$

To make notation easier, the phase angle can be replaced as follows:

$$i_c(t) = \sqrt{2}\,I_c\,sin(\omega t - \theta) \tag{3.13}$$

where

$$\theta = tan^{-1}\left(\frac{V_s - V_c\,cos(\delta)}{V_c\,sin(\delta)}\right) \tag{3.14}$$

The definitions of active, reactive and apparent power formulas are defined as follows:

$$P_s = V_s\,I_c\,cos(\theta) \tag{3.15}$$

$$Q_s = V_s\,I_c\,sin(\theta) \tag{3.16}$$

$$S = V_s\,I_c \tag{3.17}$$

One can also derive another set of power definitions by replacing the current magnitude and phase angle given in (3.15), (3.16), and (3.17) with the definitions given in (3.9) and (3.14). By doing so, the following active, reactive, and apparent power definitions are found:

$$P_s = \frac{V_s\, V_c\, sin(\delta)}{\omega L_c} \tag{3.18}$$

$$Q_s = \frac{V_s}{\omega L_c}\, \{V_s - V_c\, cos(\delta)\} \tag{3.19}$$

$$S = \frac{V_s}{\omega L_c} \sqrt{{V_c}^2 + {V_s}^2 - 2V_c\, V_s\, cos(\delta)} \tag{3.20}$$

3.3 Effect of single-phase ac-dc power transfer on the stored ripple energy at the dc-link capacitor

The definition of the instantaneous power drawn from the grid is as follows:

$$p_s(t) = v_s(t)\, i_c(t) \tag{3.21}$$

Using (3.1) and (3.13), the instantaneous input power can be written as:

$$\begin{aligned} p_s(t) &= 2\, V_s\, I_c\, sin(\omega t)\, sin(\omega t - \theta) \\ &= 2\, V_s\, I_c\, \frac{1}{2}\, \{cos(\theta) - cos(2\omega t - \theta)\} \\ &= V_s\, I_c\, cos(\theta) - V_s\, I_c\, cos(2\omega t - \theta) \end{aligned} \tag{3.22}$$

Using the definition of the voltage of an inductor ($v_L(t)$), the instantaneous power of the coupling inductor can be calculated:

$$\begin{aligned} p_L(t) &= v_L(t)\, i_c(t) \\ &= L_c\, \frac{di_c(t)}{dt}\, i_c(t) \\ &= L_c\, \{\sqrt{2}\, I_c\, \omega\, cos(\omega t - \theta)\}\, \{\sqrt{2}\, I_c\, sin(\omega t - \theta)\} \\ &= 2\, \omega\, L_c\, {I_c}^2\, sin(\omega t - \theta)\, cos(\omega t - \theta) \\ &= w\, L_c\, {I_c}^2\, sin(2\omega t - 2\theta) \end{aligned} \tag{3.23}$$

The instantaneous power that the charger receives is equal to instantaneous grid power minus the instantaneous power of the inductor. Therefore:

$$\begin{aligned} p_c(t) &= p_s(t) - p_L(t) \\ &= V_s\, I_c\, cos(\theta) - V_s\, I_c\, cos(2\omega t - \theta) - w\, L_c\, {I_c}^2\, sin(2\omega t - 2\theta) \end{aligned} \tag{3.24}$$

The instantaneous charger input power contains two components: the average power and the ripple power component at twice the grid frequency.

$$P_{ave} = V_s\, I_c\, cos(\theta) \tag{3.25}$$

$$P_{ripple}(t) = -\{V_s\, I_c\, cos(2\omega t - \theta) + \omega L_c\, {I_c}^2\, sin(2\omega t - 2\theta)\} \tag{3.26}$$

The ripple component can be summed into a single sinusoidal function using phasor addition since both of the sinusoidal components of (3.26) are at the same frequency.

$$P_{ripple}(t) = -\{V_s\, I_c\, cos(2\omega t - \theta) + \omega L_c\, {I_c}^2\, cos(2\omega t - 2\theta - \frac{\pi}{2})\} \tag{3.27}$$

$$\begin{aligned}
\overline{P_{ripple}} &= -\{V_s\, I_c\, e^{-j\theta} + \omega L_c\, {I_c}^2\, e^{-j(2\theta+\frac{\pi}{2})}\} \\
&= -V_s\, I_c\, cos(\theta) + jV_s\, I_c\, sin(\theta) - \omega L_c\, {I_c}^2\, cos(2\theta + \frac{\pi}{2}) + j\omega L_c\, {I_c}^2\, sin(2\theta + \frac{\pi}{2}) \\
&= \{-V_s\, I_c\, cos(\theta) + \omega L_c\, {I_c}^2\, sin(2\theta)\} + j\{V_s\, I_c\, sin(\theta) + \omega L_c\, {I_c}^2\, cos(2\theta)\} \\
&= P_{ripple}\, e^{j\beta} \qquad (3.28)
\end{aligned}$$

where

$$P_{ripple} = \sqrt{(V_s\, I_c)^2 + (\omega L_c\, {I_c}^2)^2 - 2\omega L_c\, V_s\, {I_c}^3 sin(\theta)} \qquad (3.29)$$

$$\beta = tan^{-1}\left(\frac{V_s\, I_c\, sin(\theta) + \omega L_c\, {I_c}^2\, cos(2\theta)}{-V_s\, I_c\, cos(\theta) + \omega L_c\, {I_c}^2\, sin(2\theta)}\right) \qquad (3.30)$$

The magnitude of the ripple power, P_{ripple}, can be defined in terms of the active and reactive power that is sent to the charger by the grid. As stated before, the positive sign for all the power variables stand for power transfer from the grid to the charger. Plugging (3.15), (3.16), and (3.17) into (3.29) yields the ripple power in terms of P_s, Q_s, and S:

$$P_{ripple} = \sqrt{S^{\,2} + \left(\omega L_c\, \frac{S^{\,2}}{{V_s}^2}\right)^2 - 2\omega L_c\, \frac{S^{\,2}}{{V_s}^2} Q_s} \qquad (3.31)$$

Finally, the instantaneous power that the charger receives from the grid is written in time domain form. Note that, the ripple power is converted to time domain form using (3.28).

$$\begin{aligned}
p_c(t) &= P_{ave} + p_{ripple}(t) \\
&= V_s\, I_c\, cos(\theta) + P_{ripple}\, cos(2\omega t + \beta) \qquad (3.32)
\end{aligned}$$

The ripple power component of the instantaneous charger power is a result of the single-phase conversion of ac power into dc power, and it is an oscillating power between the grid and the charger. This oscillating ripple power is temporarily stored in the dc-link capacitor of the charger. In other words, the dc-link capacitor is used to balance the power transfer between the grid and the charger to effectively charge the vehicle battery.

As (3.31) suggests, when the charger is used to source/sink reactive power in addition to providing active power, this oscillating ripple power component changes. Therefore, the effect of reactive power transfer on the dc-link capacitor becomes an issue when designing the charger for reactive power operation mode.

Equation (3.32) is plotted in Fig. 3.3 using the following system parameters: $V_s = 240\ V$ (Level 2 charging), P_s=3.3 kW, Q_s=0 VAR, L_c=1 mH and f=60 Hz. The dc-link capacitor should have the capacity to store the required energy to balance the power transfer. As the capacitor is the energy storage method of the oscillatory ripple power at the dc-link, the required energy capacity of the dc-link capacitor can be found by integrating the ripple power waveform plotted in Fig. 3.3 between its minimum and maximum values.

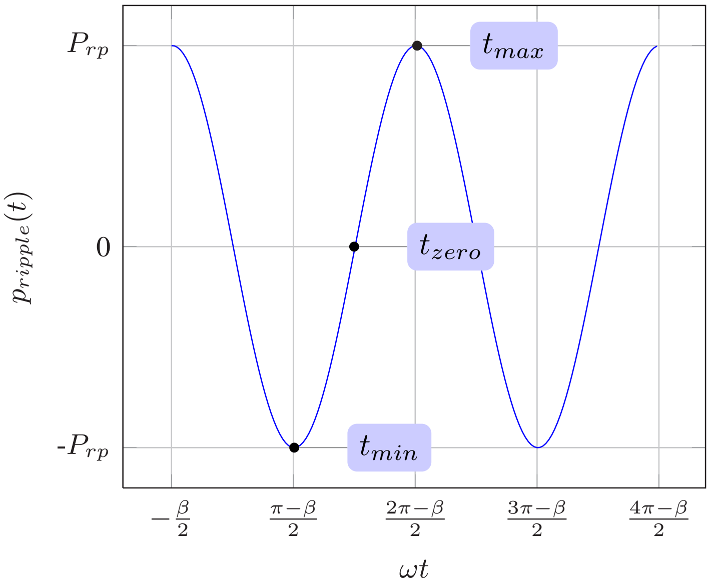

Figure 3.3: Instantaneous charger input ripple power.

This means that the dc-link capacitor should have the energy capacity to store and then discharge the energy explained below.

$$\begin{aligned}
E_{ripple} &= \int_{t_{min}}^{t_{zero}} \left|p_{ripple}(t)\right|dt + \int_{t_{zero}}^{t_{max}} \left|p_{ripple}(t)\right|dt \\
&= 2\int_{t_{zero}}^{t_{max}} P_{ripple}\, cos(2\omega t+\beta)dt \\
&= \frac{1}{\omega}P_{ripple}\, sin(2\omega t+\beta)\Big|_{t_{zero}}^{t_{max}} \qquad (3.33)
\end{aligned}$$

where based on Fig. 3.3, t_{zero} occurs when $2\omega t+\beta = 3\pi/2$ and t_{max} occurs when $2\omega t+\beta = 2\pi$. Therefore:

$$\begin{aligned}
E_{ripple} &= \frac{1}{\omega}\, P_{ripple}\, sin(2\omega t+\beta)\Big|_{\frac{1}{2\omega}\{\frac{3\pi}{2}-\beta\}}^{\frac{1}{2\omega}\{2\pi-\beta\}} \\
&= \frac{1}{\omega}\, P_{ripple}\,\{sin(2\pi) - sin(\frac{3\pi}{2})\} \\
&= \frac{P_{ripple}}{\omega} \qquad (3.34)
\end{aligned}$$

Plugging (3.31) into (3.34) gives:

$$E_{ripple} = \frac{1}{\omega}\sqrt{S^{\,2} + \left(\omega L_c \frac{S^{\,2}}{V_s^{\,2}}\right)^2 - 2\omega L_c \frac{S^{\,2}}{V_s^{\,2}} Q_s} \qquad (3.35)$$

The relation of the ripple energy calculated in (3.35) to the reactive power transfer is investigated here for two charger input power values: $S = 3.3$ kVA and $S = 6.6$ kVA. The parameters used in the analysis are shown in Table 3.1. The base value for the ripple energy is calculated when the charger operates at unity power factor which means reactive power, Q_s, is zero. This is to show the effect of the reactive power operation on the required ripple energy compared to charging only operation. The base value for the ripple energy is calculated using (3.35). It is 8.75 J for $S = 3.3$ kVA, and it is 17.5 J for $S = 6.6$ kVA.

Table 3.1: The base system parameters used in showing the analysis results.

Parameter	Symbol	Base value for system 1	Base value for system 2
Charger apparent power	S	3.3 kVA	6.6 kVA
Grid voltage	V_s	240 V	240 V
Grid frequency	f	60 Hz	60 Hz
Coupling inductance	L_c	1.0 mH	1.0 mH
DC-link voltage	V_{dc}	450 V	450 V
DC-link peak-peak ripple voltage	ΔV_{dc}	10% (45 V)	10% (45 V)
DC-link capacitance	C_{dc}	432.5 μF	865 μF
DC capacitor ripple rms current	I_{cap}	5.2 A	10.4 A

Figure 3.4 illustrates the effect of reactive power (from rated inductive to rated capacitive) operation for S=3.3 kVA on the required ripple energy storage. While the reactive power changes from full inductive (pf is zero-lagging) to full capacitive operation (pf is zero-leading), it shows that the required ripple energy storage at the dc-link increases. The dc-link capacitor has to store the most ripple energy in a charge/discharge cycle when the charger operates in full capacitive mode. Moreover, as the input coupling impedance increases, the required ripple energy increases. Similarly, Fig. 3.5 shows the same effect for S = 6.6 kVA charger.

The summary of the effect of the reactive power operation on the required dc-link ripple storage energy is shown in Fig 3.6. It is shown that as the input power increases, the effect of reactive power operation (compared to charging only operation) on the required dc ripple storage becomes more obvious due to the reactive power component of (3.35). In other words, the ripple energy increase issue becomes worse as the charger input power increases, and therefore dc-link energy storage requirement increases more on higher power levels. The following sections describe this effect in terms of dc-link capacitance, dc-link ripple voltage, capacitor ripple current, and minimum required dc link voltage.

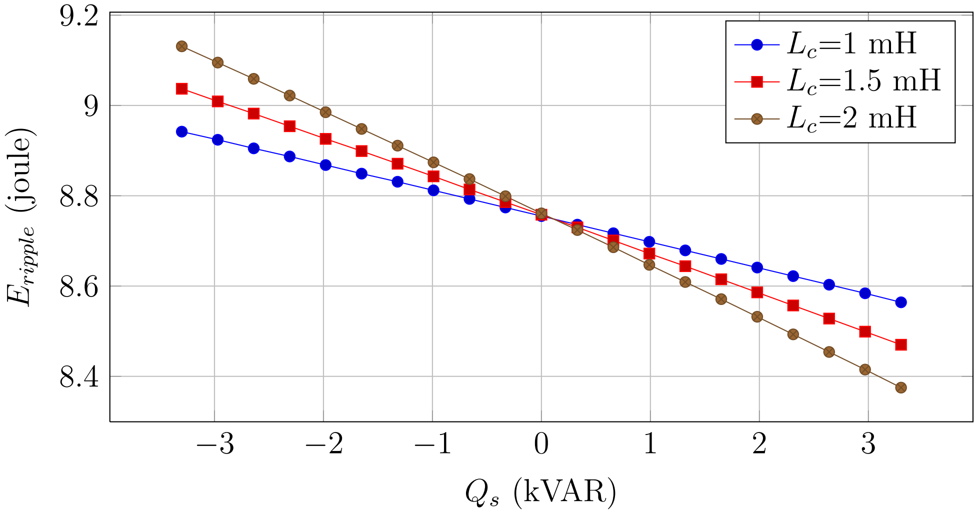

Figure 3.4: Change of the required ripple energy storage at the dc-link with different reactive power values for $S = 3.3$ kVA.

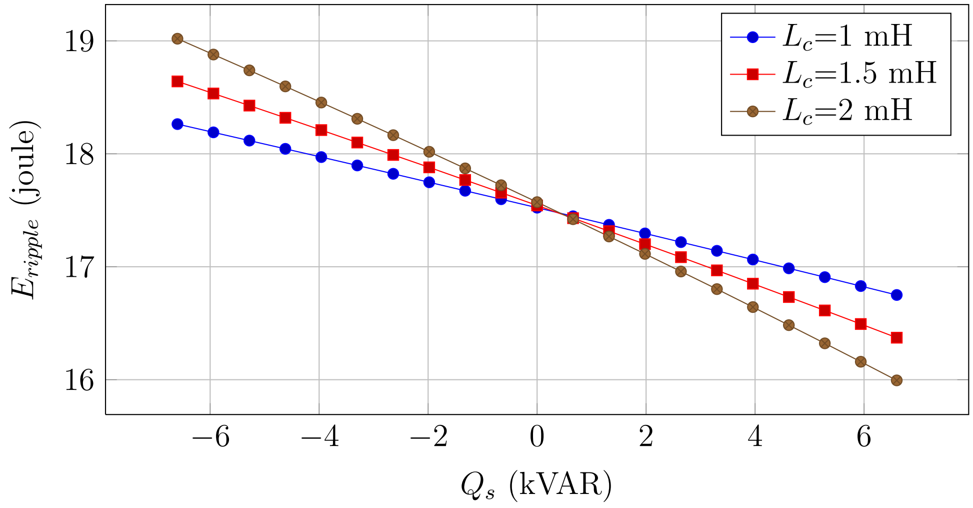

Figure 3.5: Change of the required ripple energy storage at the dc-link with different reactive power values for $S = 6.6$ kVA.

3.4 Effect of single-phase ac-dc power transfer on the dc-link capacitor

As stated in [27], once the values for V_{dc} and ΔV_{dc} are selected for a specific application, the selection of a dc-link capacitor is done using two parameters: a

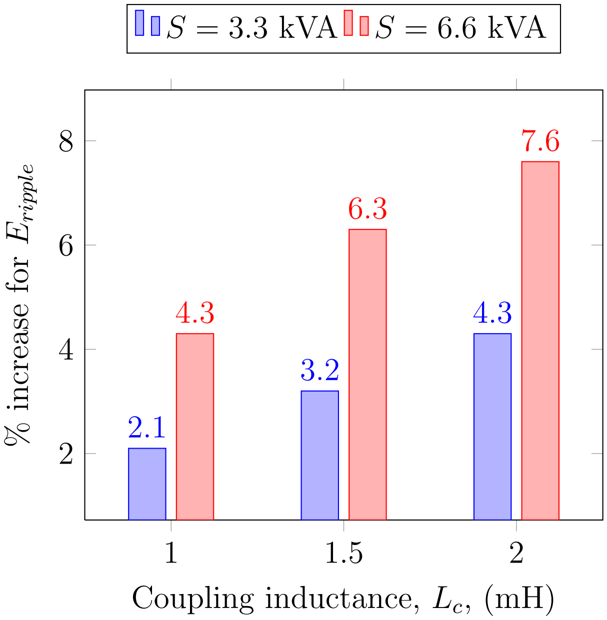

Figure 3.6: The net % change in the ripple energy (E_{ripple}) for a reactive power change of 100% for different L_c values.

required capacitance, and a required current rms value given in a frequency range. For this analysis, V_{dc} is selected to be 450 V and ΔV_{dc} is chosen to be 10% of V_{dc}.

This section first investigates the inherent ripple energy storage requirement in single-phase ac-dc power conversion systems. Then, it calculates how the ripple energy storage requirement translates into dc-link capacitance, dc-link ripple voltage, and dc-link capacitor current. Consequently, it will provide how these parameters change when the charger operates in reactive power mode.

3.4.1 Effect of reactive power on the dc-link capacitance and dc-link ripple voltage

The instantaneous energy stored in a dc capacitor can be found using the following equation:

$$E_{cap}(t) = \frac{1}{2} C_{dc} v_{dc}^2(t) \tag{3.36}$$

where E_{cap}(t) is the instantaneous energy (J) of the capacitor, C_{dc} is the dc-link capacitance (F), and $v_{dc}(t)$ is the capacitor voltage (V). Figure 3.7 shows the voltage ripple and current waveform of a capacitor using the capacitor voltage-current equation shown below:

$$i_{cap}(t) = C_{dc}\,\frac{dv_{dc,ripple}(t)}{dt} \tag{3.37}$$

The dc offset of the capacitor voltage (V_{dc}) is not shown in order to show the two waveforms on the same scale. The current flowing through the capacitor is leading the voltage by 90° and charging the capacitor from its minimum voltage to the maximum voltage. Therefore, the maximum energy (in joules) that a dc-link capacitor can store in a charging cycle is calculated by the following:

$$\Delta E_{max} = \frac{1}{2}\,C_{dc}\,\{V_{dc,max}^2 - V_{dc,min}^2\} \tag{3.38}$$

where $V_{dc,max}$ and $V_{dc,min}$ are maximum and minimum voltage levels as shown in Fig. 3.7. The difference between the minimum and maximum voltage is $\Delta V_{dc} = V_{dc,max} - V_{dc,min}$. The average value of the instantaneous dc-link voltage is V_{dc}. Therefore, the energy stored in one cycle equals to:

$$\begin{aligned}
\Delta E_{max} &= \frac{1}{2}\,C_{dc}\,\{V_{dc,max} - V_{dc,min}\}\,\{V_{dc,max} + V_{dc,min}\} \\
&= \frac{1}{2}\,C_{dc}\,(\Delta V_{dc})\,\{V_{dc,max} + V_{dc,min}\} \\
&= \frac{1}{2}\,C_{dc}\,(\Delta V_{dc})\,(2V_{dc}) \\
&= C_{dc}\,\Delta V_{dc}\,V_{dc} \qquad (3.39)
\end{aligned}$$

The peak-to-peak ripple energy found in (3.35) that is a result of the ac-dc power conversion is stored in the dc link capacitor. The peak-to-peak energy storage capability of the dc link capacitor was found in (3.39), therefore, in a lossless system

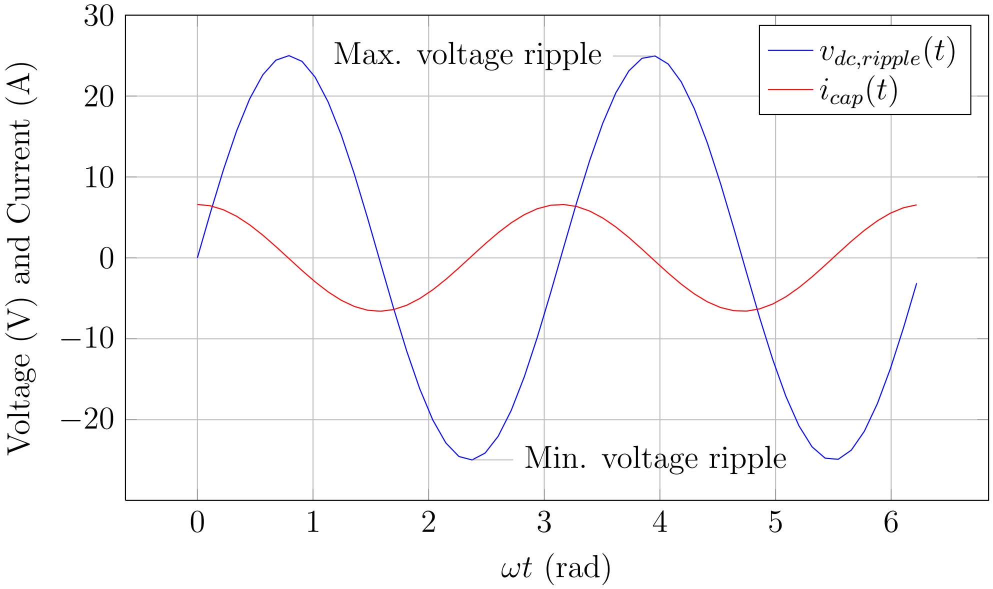

Figure 3.7: Capacitor voltage and current waveforms.

E_{ripple} found in (3.35) is equal to ΔE_{max} in (3.39). This yields that:

$$C_{dc} = \frac{\sqrt{S^2 + \left(\omega L_c \frac{S^2}{V_s^2}\right)^2 - 2\omega L_c \frac{S^2}{V_s^2} Q_s}}{\omega \, \Delta V_{dc} \, V_{dc}} \tag{3.40}$$

The dc link capacitance should be equal or greater than (3.40) to limit the maximum value of the peak-to-peak voltage ripple (ΔV_{dc}) at the dc link. If C_{dc} is selected smaller than (3.40), then ΔV_{dc} will increase. In other words, a higher C_{dc} than (3.40) will result in a smaller ΔV_{dc}. To keep the converter size smaller, the dc-link capacitor should not be oversized, and ΔV_{dc} should be kept at its allowable maximum value.

Figures 3.8 and 3.9 show the effect of the reactive power operation on the minimum required dc link capacitance such that $\Delta V_{dc,max} = 10\%$ and Q_s changes from inductive to capacitive. It is important to note that ΔV_{dc} changes when Q_s changes during the operation of the circuit. However, it experiences a 10% ripple at the worst case which is when Q_s is fully capacitive. The charger input power is always kept at $S = 3.3$ kVA

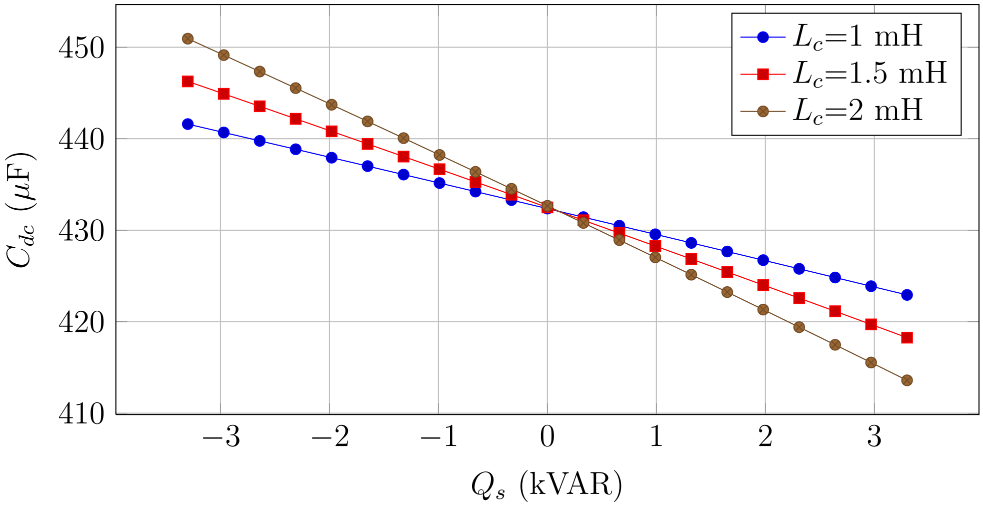

Figure 3.8: Change of C_{dc} with varying Q_s and for different L_c values for the case of $S = 3.3$ kVA.

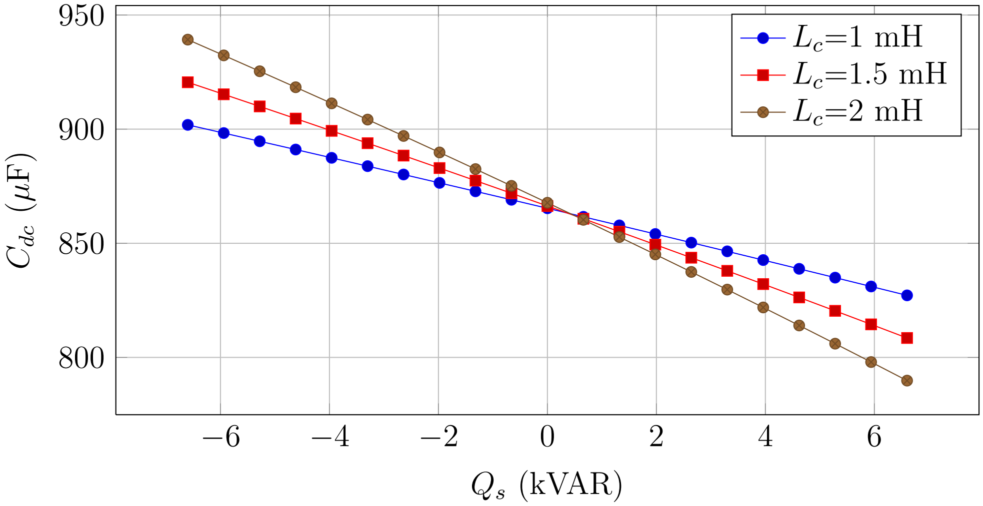

Figure 3.9: Change of C_{dc} with varying Q_s and for different L_c values for the case of $S = 6.6$ kVA.

and $S = 6.6$ kVA for Figs. 3.8 and 3.9, respectively. Initially, the charger is assumed to be in PFC operation with the base parameters given in Table 3.1. Then, the required capacitance is calculated to get the same ΔV_{dc} for different Q_s levels.

For consistency throughout the analysis, the nominal increase in the required capacitance is also calculated. Moreover, if the capacitor size is kept the same, then

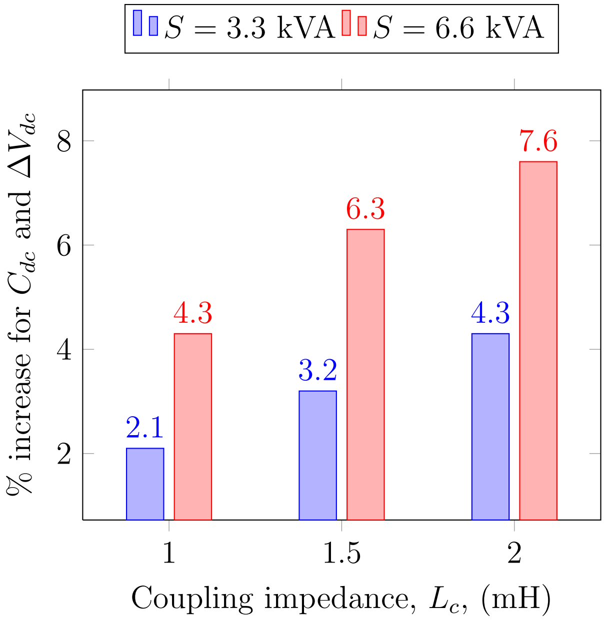

Figure 3.10: The net % change of required C_{dc} and ΔV_{dc} for a 100% capacitive reactive power increase for different L_c values.

ΔV_{dc} is going to increase at the same rate as the dc-link capacitor did. Both of these results are presented in Fig.3.10.

The nominal percent increase on the required C_{dc} or ΔV_{dc} is the same with the required nominal ripple energy increase. This is an expected result because the ripple on the dc-link is a result of the single-phase ac-dc conversion ripple energy. Again, as expected, the increase on the required C_{dc} or ΔV_{dc} increases with greater coupling impedance and with greater charger input power.

3.4.2 Effect of reactive power on the required capacitor ripple rms current

Since the PWM harmonic ripples are neglected, the dc-link voltage of the ac-dc converter is comprised of an average and a second harmonic ripple component. Therefore, it can be expressed with the following equation:

$$v_{dc}(t) = V_{dc} + \frac{\Delta V_{dc}}{2} sin(2\omega t) \tag{3.41}$$

Therefore, the second harmonic current can be found as:

$$\begin{aligned} i_{cap}(t) &= C_{dc}\,\frac{dv_{dc}}{dt} \\ &= \omega\, C_{dc}\,\Delta V_{dc}\, cos(2\omega t) \end{aligned} \tag{3.42}$$

Therefore, the rms value of the current is:

$$I_{cap} = \frac{1}{\sqrt{2}}\,\omega\, C_{dc}\,\Delta V_{dc} \tag{3.43}$$

By using (3.40), it can also be written in terms of circuit parameters:

$$I_{cap} = \frac{\sqrt{S^{\,2} + \left(\omega L_c\,\frac{S^{\,2}}{V_s^{\,2}}\right)^2 - 2\omega L_c\,\frac{S^{\,2}}{V_s^{\,2}} Q_s}}{\sqrt{2}\,V_{dc}} \tag{3.44}$$

An important conclusion of (3.44) is that I_{cap} does not depend on the capacitance, C_{dc}. The required ripple current rating of the dc-link capacitor depends on L_c, V_{dc}, and Q_s for fixed ω, S, and V_s. The base value for the capacitor ripple current, I_{cap} is calculated using PFC operation and the base values given in Table 3.1. The results are plotted in Figs. 3.11 and 3.12. Again, the required capacitor rms current increases with capacitive reactive power, coupling inductance, and higher charger input power. Figure 3.13 also summarizes the net percent increase of capacitor current for a reactive power change from zero to fully capacitive mode.

3.4.3 Effect of reactive power on the required minimum dc-link voltage

Using a single-phase ac-dc active rectifier, the dc voltage has a minimum limit to satisfy the sinusoidal line current operation. If this minimum limit is not satisfied, then the line current harmonics will increase above the utility allowed limits. For a

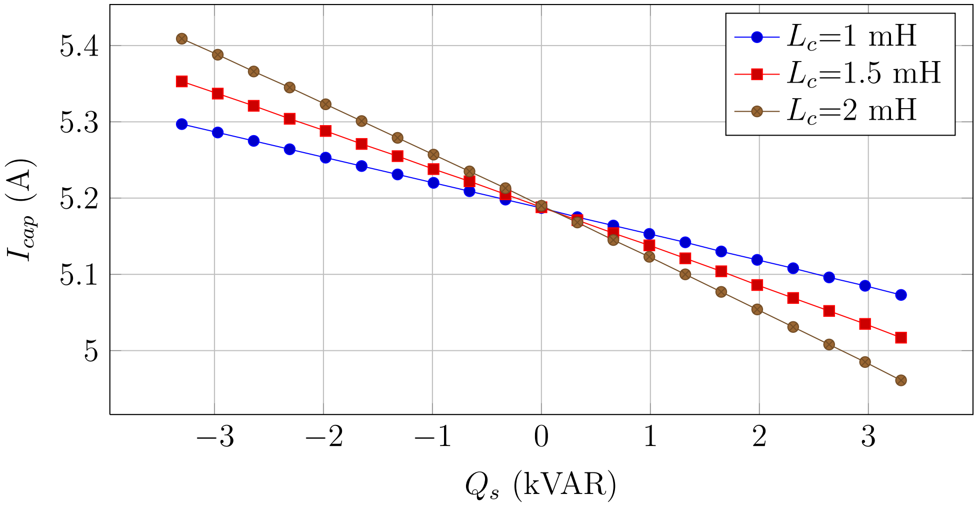

Figure 3.11: Change of I_{cap} with varying Q_s and for different L_c values for the case of $S = 3.3$ kVA.

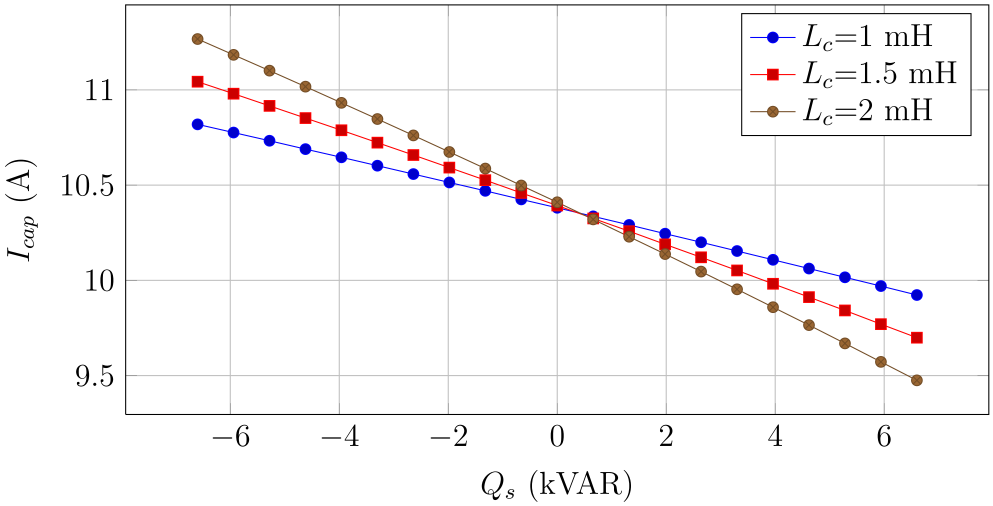

Figure 3.12: Change of I_{cap} with varying Q_s and for different L_c values for the case of $S = 6.6$ kVA.

full-bridge inverter, the requirement for sinusoidal operation is equal to:

$$V_{dc} \geq \sqrt{2}V_c \tag{3.45}$$

In other words, the inverter always operates in the linear modulation index region. If the dc link voltage drops below the minimum limit, then over-modulation occurs

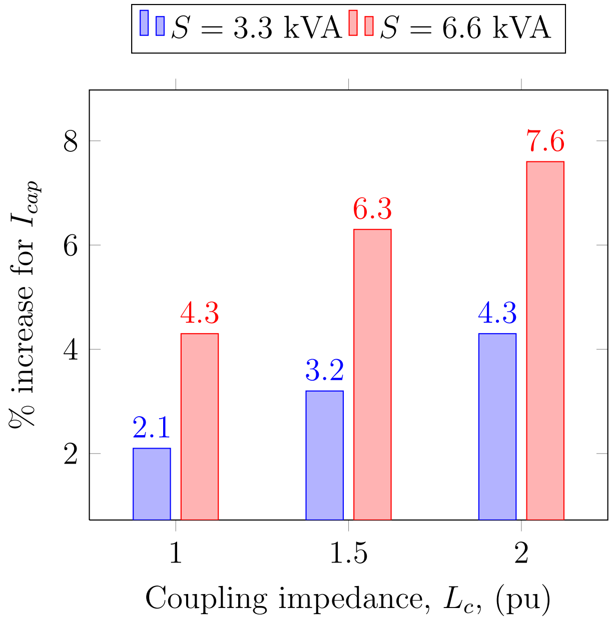

Figure 3.13: The net % change in the capacitor current (I_{cap}) for a 100% capacitive reactive power increase for different L_c values.

which distorts the output current waveform. In order to find the limit on the dc voltage and how this limit changes with the power transfer, the charger voltage, V_c will be derived in terms of reactive power. The steady state solution of Fig. 3.2 using KVL yields:

$$\begin{aligned}
\overline{V_c} &= \overline{V_s} - \overline{V_L} \\
&= \sqrt{2}\,V_s\,e^{-j\frac{\pi}{2}} - j\omega\,L_c\,\overline{I_c} \\
&= -j\sqrt{2}\,V_s - j\omega\,L_c\,(\sqrt{2}\,I_c\,e^{-j\alpha}) \\
&= -j\sqrt{2}\,V_s - j\omega\,L_c\,\{\sqrt{2}\,I_c\,(cos(\alpha) - j sin(\alpha))\} \\
&= -\sqrt{2}\,\omega\,L_c\,I_c\,sin(\alpha) - j\{\sqrt{2}\,V_s + \sqrt{2}\,\omega\,L_c\,I_c\,cos(\alpha)\} \\
&= -\sqrt{2}\,\omega\,L_c\left(\frac{S}{V_s}\right)\left(\frac{P}{S}\right) - j\{\sqrt{2}\,V_s + \sqrt{2}\,\omega\,L_c\left(\frac{S}{V_s}\right)\left(\frac{-Q}{S}\right)\} \\
&= -\sqrt{2}\,\omega\,L_c\,\frac{P}{V_s} - j\sqrt{2}\left(V_s - \omega\,L_c\,\frac{Q}{V_s}\right) \qquad (3.46)
\end{aligned}$$

Using (3.2), it can be written that:

$$V_c = \sqrt{{V_s}^2 + (\omega\, L_c)^2 \left(\frac{S}{V_s}\right)^2 - 2\,\omega L_c\, Q} \tag{3.47}$$

and,

$$\delta = tan^{-1} \left(\frac{\omega\, L_c \dfrac{P}{V_s}}{V_s - \omega\, L_c \dfrac{Q}{V_s}} \right) \tag{3.48}$$

Using 3.45, the limit on the dc-link voltage can be written as:

$$V_{dc} \geq \sqrt{2 \left({V_s}^2 + (\omega\, L_c)^2 \left(\frac{S}{V_s}\right)^2 - 2\,\omega L_c\, Q \right)} \tag{3.49}$$

The result of the analysis for $S = 3.3$ kVA and $S = 6.6$ kVA charger examples are shown in Fig. 3.14 and Fig. 3.15, respectively. The analysis is applied for three different coupling inductances: L_c=1.0, 1.5, and 2.0 mH. In both figures, the minimum dc voltage limit is increasing as the charger supplies more capacitive power to the grid, and the limit decreases as the charger sinks more reactive power from the grid.

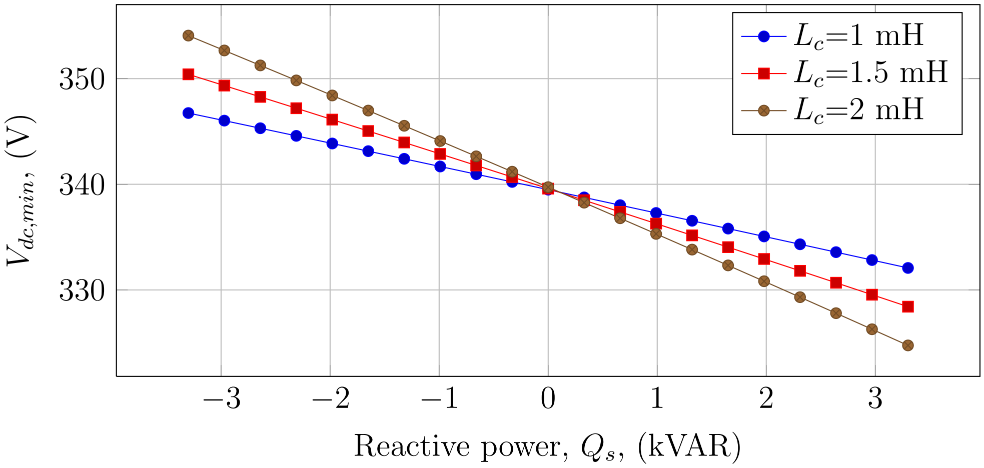

Figure 3.14: Change of the required minimum dc link voltage for different reactive power values for $S = 3.3$ kVA.

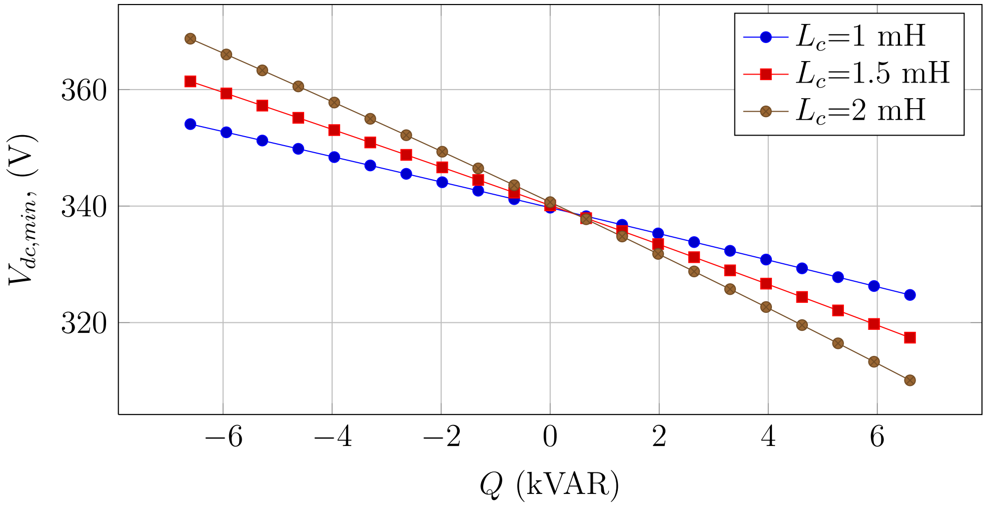

Figure 3.15: Change of the required minimum dc link voltage for different reactive power values for $S = 6.6$ kVA.

The net impact of reactive power change is summarized in Fig. 3.16. The net reactive power change requires a 2.1% increase in the minimum V_{dc} to satisfy sinusoidal operation with limited current THD present. This means that the required minimum dc-link voltage increases by 2.1% when the charger supplies full reactive power to the grid compared to PFC operation. During this operation $S = 3.3$ kVA, $V_s = 240$ V, and $X_c = 1.0$ pu. If the charger is designed at $S = 6.6$ kVA, the net increase for $V_{dc,min}$ becomes 4.3%. The net change in the requirement increases with increasing coupling inductor. Therefore, when a charger is designed to operate at full-reactive power, the minimum dc-link voltage requirement increase should be handled.

3.5 Conclusion

This chapter describes the effect of reactive power on the different system parameters by evaluating this effect on only one parameter while the remaining parameters are kept constant. In summary, all of the parameters ($V_{dc,min}$, C_{dc}, ΔV_{dc}, and I_{cap}) experience a 2.1%-4.3% increase for 3.3 kVA charger system depending on the

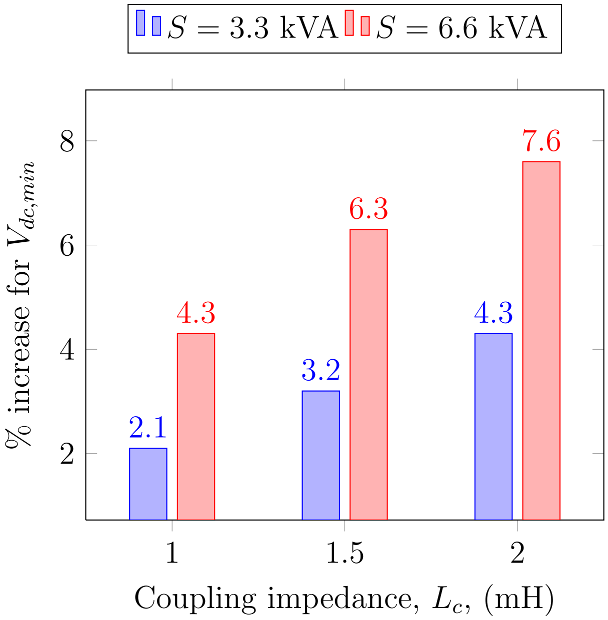

Figure 3.16: The net % change of required $V_{dc,min}$ for a 100% capacitive reactive power increase for different L_c values.

selected L_c for a reactive power change from zero to fully capacitive mode. The effect increases to 4.3%-7.6% when the charger operates at 6.6 kVA. Therefore, the single-phase charger design should handle the increased requirements for the reactive power operation to be able to symmetrically operate at the four quadrants of the power plane.

Chapter 4

Simulation Verification of the Effect of Reactive Power Operation on the Charger

4.1 Introduction

This chapter presents the design stages of the unidirectional PFC charger for full active power operation. The design involves the following stages: ac-dc converter controller design, dc-dc converter controller design, total system controller design, and modeling of the battery pack. The most important requirement of the charger design is to effectively control the line current harmonics. The ac-dc converter input current THD should be limited to 5%.

The objective of the system controller is to follow the charging power and reactive power commands controlled by the grid operator. Three different charger designs are simulated: A Level 1 1.4 kVA charger, a Level 2 3.3 kVA charger, and a Level 2 6.6 kVA charger.

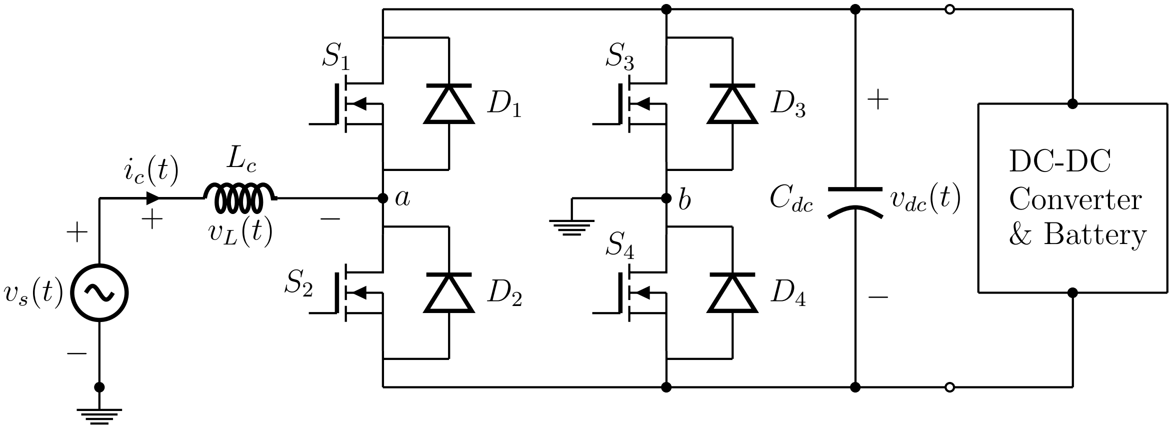

Figure 4.1: Full bridge bidirectional ac-dc converter.

4.2 Modeling and Controller Design of the AC-DC Converter

The configuration of the selected ac-dc full bridge converter is shown in Fig. 4.1. The following sections describe the control method and modulation strategies. Due to inherent advantages to be used in single-phase systems, proportional resonant (PR) current controller is selected for inner current loop control. The selected pulse width modulation (PWM) is sinusoidal bipolar modulation. With this modulation, the input voltage of the ac-dc converter (the voltage difference between points a and b in Fig. 4.1) can have two positions $+V_{dc}$ and $-V_{dc}$. The derivation of the controller is explained below with the following steps: switching model, average model, and small signal model.

Switching model

The switching model diagram is shown in Fig. 4.2. The dc-dc converter and the battery are modeled as a dc voltage source in series with a equivalent resistor. Therefore, the switching PWM components of the dc-dc converter are ignored and will be treated separately during dc-dc converter modeling. Single-pole double-throw

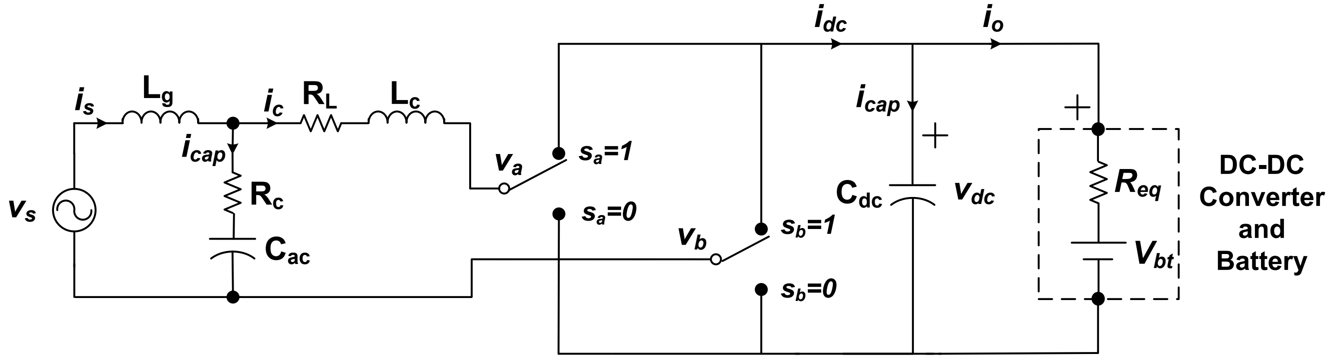

Figure 4.2: AC-DC converter switching model.

switches are used to represent a phase-leg shown in Fig. 4.1. When the switches S_1 and S_4 are on, and S_2 and S_3 are off, the charger current i_c is equal to i_{dc} and v_{ab} equals to V_{dc}. In this case $s_a = 1$ and $s_b = 0$. If the switches S_1 and S_4 are off and S_2 and S_3 are on, i_c is equal to $-i_{dc}$ and v_{ab} is equal to $-V_{dc}$. In this case, $s_a = 0$ and $s_b = 1$. Therefore, following equations are true:

$$\begin{aligned} v_{ab} &= v_a - v_b \\ &= (s_a - s_b) \times v_{dc} \\ &= s_{ab} \times V_{dc} \end{aligned} \tag{4.1}$$

$$\begin{aligned} i_{dc} &= (s_a - s_b) \times i_c \\ &= s_{ab} \times i_c \end{aligned} \tag{4.2}$$

where

$$s_{ab} = s_a - s_b \tag{4.3}$$

Neglecting the ESR of the capacitor (R_c), the state-space equations resulting from application of KVL and KCL in Fig. 4.2 are:

$$\frac{di_s}{dt} = \frac{v_s}{L_g} - \frac{v_{cap}}{L_g} \tag{4.4}$$

$$\frac{di_c}{dt} = \frac{v_{cap}}{L_c} - \frac{R_L\, i_c}{L_c} - \frac{v_{ab}}{L_c} \tag{4.5}$$

$$\frac{dv_{cap}}{dt} = \frac{i_s}{C_{ac}} - \frac{i_c}{C_{ac}} \tag{4.6}$$

where i_s is the grid current, v_s is the grid voltage, v_{cap} is the ac filter capacitor voltage, L_g is the grid inductance, L_c is the coupling inductance, C_{ac} is the ac filter capacitor, R_L is the equivalent series resistance of the coupling inductance.

Average model

The averaging operator over one switching period is applied to the switching model to get the average model of the system. For a time-variant variable x, the averaging operator is defined as:

$$\overline{x(t)} = \frac{1}{T} \int\limits_{t-T}^{t} x(\tau)\, d\tau \tag{4.7}$$

The overline of a variable, $\overline{x(t)}$, stands for the averaged value. Therefore, applying averaging operator to the above state-space equations (4.4)-(4.6), yields the following equations:

$$\frac{d\overline{i_s}}{dt} = \frac{\overline{v_s}}{L_g} - \frac{\overline{v_{cap}}}{L_g} \tag{4.8}$$

$$\frac{d\overline{i_c}}{dt} = \frac{\overline{v_{cap}}}{L_c} - \frac{R_L\, \overline{i_c}}{L_c} - \frac{d_{ab} V_{dc}}{L_c} \tag{4.9}$$

where

$$d_{ab} = \overline{s}_{ab} \tag{4.10}$$

$$\frac{d\overline{v_{cap}}}{dt} = \frac{\overline{i_s}}{C_{ac}} - \frac{\overline{i_c}}{C_{ac}} \tag{4.11}$$

where d_{ab} stands for the averaged value of s_{ab}, and V_{dc} is the average dc-link voltage.

Small-signal model

In order to construct the small signal model, the average model variables are composed of the steady state values and superimposed small ac variations. The resulting small signal equations are:

$$\frac{d\tilde{i}_s}{dt} = \frac{\tilde{v}_s}{L_g} - \frac{\tilde{v}_{cap}}{L_g} \tag{4.12}$$

$$\frac{d\tilde{i}_c}{dt} = \frac{\tilde{v}_{cap}}{L_c} - \frac{R_L\,\tilde{i}_c}{L_c} - \frac{\tilde{d}_{ab}V_{dc}}{L_c} \tag{4.13}$$

$$\frac{d\tilde{v}_{cap}}{dt} = \frac{\tilde{i}_s}{C_{ac}} - \frac{\tilde{i}_c}{C_{ac}} \tag{4.14}$$

To derive the relationship between $\tilde{d}_{ab}$ and $\tilde{i}_c$, Laplace transform is used and then $\tilde{i}_c$ is isolated. Finally, the following equation is found:

$$\begin{aligned} \tilde{i}_c \quad = \quad & \tilde{v}_s \times \frac{L_c}{s^3\,L_g\,L_c\,C_{ac} + s^2\,L_g\,C_{ac}\,R_L + s\,(L_c + L_g) + R_L} \\ & -\tilde{d}_{ab} \times \frac{-V_{dc}\,(s^2\,L_g\,C_{ac} + 1)}{s^3\,L_g\,L_c\,C_{ac} + s^2\,L_g\,C_{ac}\,R_L + s\,(L_c + L_g) + R_L} \end{aligned} \tag{4.15}$$

If the disturbance from the grid voltage is assumed to be zero, the final relationship is found as follows:

$$\tilde{i}_c = \frac{-V_{dc}\,(s^2\,L_g\,C_{ac} + 1)}{s^3\,L_g\,L_c\,C_{ac} + s^2\,L_g\,C_{ac}\,R_L + s\,(L_c + L_g) + R_L} \times \tilde{d}_{ab} \tag{4.16}$$

At high frequencies, the transfer function approaches to:

$$\tilde{i}_c = \frac{-V_{dc}}{sL_c} \times \tilde{d}_{ab} \tag{4.17}$$

Note that, due to negative sign, as d_{ab} increases $\bar{i}_c$ decreases. Therefore, the transfer function of the plant is:

$$G_{id}(s) = \frac{V_{dc}}{sL_c} \tag{4.18}$$

In this study, a PR controller is employed for current control of the ac-dc converter. The transfer function of the PR controller is as follows:

$$G_c(s) = K_p + \frac{K_i\,s}{s^2 + 2\omega_c\,s + \omega_o^2} \tag{4.19}$$

Table 4.1: Parameters of the PR controller.

K_P	K_I	ω_c	ω_o
1.2	1000	3.0	377

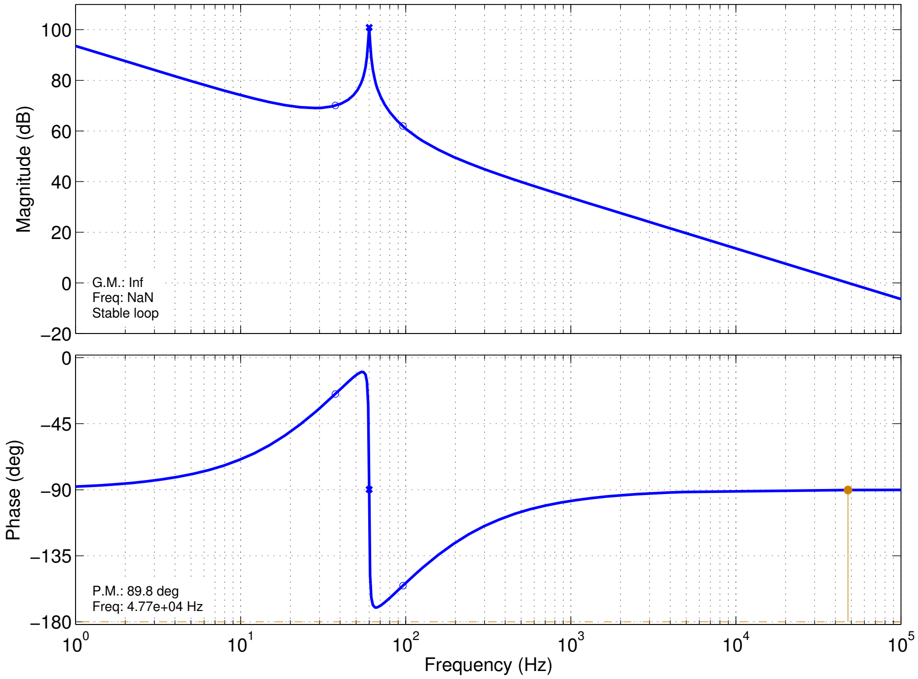

Figure 4.3: Bode diagram of current controller loop gain.

The parameters of the PR controller that satisfy stable operation of the converter is shown in Table 4.1. The resulting closed loop gain of the current controller is:

$$T(s) = G_c(s) \times G_{id}(s) \tag{4.20}$$

The final bode diagram of closed loop gain (T(s)) is presented in Fig. 4.3.

4.3 Modeling of the Battery Pack

Due to its promising capability to be used in vehicular traction applications in the future, a Li-ion battery with an LFP cathode material is selected to be the cell

Table 4.2: Parameters of Li-ion battery cell with LFP cathode composition.

Parameter	Value	Unit
Nominal cell voltage	3.3	V
Nominal capacity	$18,000$	mAh
Cut-off discharge voltage	2.10	V
Maximum charge voltage	3.65	V
Initial internal impedance	< 4	$m\Omega$

structure of the battery pack. The cell parameters of this type of battery are shown in Table 4.2. In this design, the battery cell discharge cut-off voltage is selected to be 2.95 V when the system has a SOC value of 20% of full charge. Similarly, the maximum output voltage requirement of the charger occurs when the battery pack voltage reaches its maximum SOC. Again, the highest voltage level of the cell in this design is limited to 3.6 V when the SOC reaches 90% of full charge. These values present a tighter charge-discharge window than the minimum and maximum values shown in Table 4.2. The reason why the SOC values are kept in a narrower cycling window compared to its manufacturer ratings is to increase the expected lifetime of the battery pack as much as possible before its capacity decreases to 80% of their original manufacturer ratings. This is a common method employed in the industry to preserve the original EV-only mileage rating of the vehicle during the first 10 years/100,000 mi of the vehicle.

The literature and market survey shown in Chapter 1 illustrated that the trend in the battery design pack is for higher battery pack voltages to decrease the semiconductor, passive component, and cabling current ratings in the vehicle power electronics circuits. Therefore, the design of the battery pack system employs a 360 V nominal battery pack voltage which is comparable to the battery pack of the today's EVs/PHEVs. Using the cells given in Table 4.2, the battery pack is designed.

To get 360 V nominal voltage, the number of required cells connected in series in a string is $360/3.3 = 109.09$. Therefore, the closest integer value corresponds to a voltage level of 363 V with 110 cells connected in series. The maximum pack voltage is $3.6 \times 110 = 396$ V. The minimum pack voltage is $2.95 \times 110 = 324.5$ V.

One string in this design corresponds to a nominal energy capacity of 18 Ah×363 V =6.53 kWh. According to the technical market survey in Chapter 1, the energy capacity of the vehicles ranges between 4.4 - 20.1 kWh for PHEVs and between 16 - 53 kWh for EVs. Employing more than one string in parallel will increase the total energy capacity of the battery pack to meet the electric-only mileage requirement of the vehicle.

The charger design of this study is completed for one-string battery pack design. Ideally, if the number of strings is more than one, ripple current per each string would be divided by the number of strings. Therefore, output voltage ripple requirement of the charger will not change.

The employed battery model for this study includes one SOC-mapped variable dc voltage source in series with an equivalent series resistance as shown in Fig. 4.4. Although more sophisticated battery cell models have been developed in the literature, the models are strictly dependent on the chemistry and require experimental verification of the battery cell that is being used. ESR-based model neglects very short time constant battery dynamics that can help the dc-dc converter to filter out the unwanted high frequency PWM current ripple during charging. Therefore, this model presents a worst-case scenario for very short time constant transient dynamics. However, during the long term most of the models are condensed to an SOC dependent voltage source and a series resistance.

The initial internal impedance of the cell is given in the manufacturer data sheet to be less than 4 $m\Omega$ for a 1 kHz ac battery cell charging current. In this study, the following assumptions are made for the battery model:

- Double layer capacitance of the battery pack is neglected
- The equivalent resistance selected is valid for the ripple seen during 10 A (0.55C) charging of the battery cell. Usually, Li-ion battery cells exhibit more internal

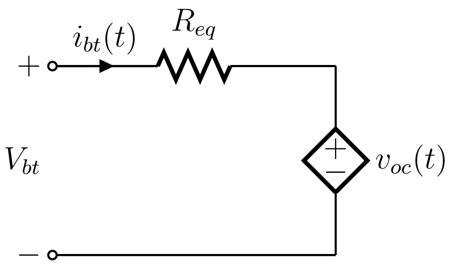

Figure 4.4: Equivalent model of the battery pack.

resistance during the charging of the battery cell proportional to the charging current. Therefore, the internal resistance is selected to be 10 $m\Omega$ per cell during the charging of the battery.

Since there are 110 cells connected in series, the total equivalent series resistance (R_{eq}) of the battery pack can be simplified as $0.01 \times 110 = 1.1\ \Omega$. The battery pack open circuit voltage can be modeled as a dc voltage source that changes with the SOC of the battery pack which is shown as $v_{oc}(t)$ in Fig. 4.4.

4.4 Modeling of the DC-DC Converter

4.4.1 Topology description and operation principle

The selected topology of the dc-dc converter is a bidirectional half-bridge dc-dc converter as explained in Chapter 2. As mentioned before, there are three different charger designs. Here, only Level 2 3.3 kVA design will be explained as it is the most common charger power rating in the market as presented in Chapter 1.

The rated output current of the charger for a 90% efficient system is $3,300 \times 0.90/363 = 8.2$ A. However, when the battery pack SOC is at its lowest value, the maximum charging current occurs for a given charging power. That is $3,300 \times 0.90/324.5 = 9.15$ A. In this study, the rated dc-dc converter output current is selected to be 10 A.

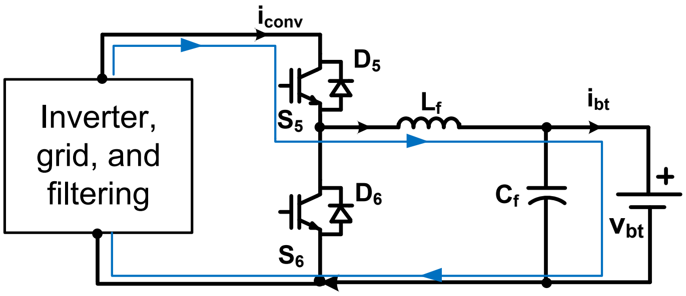

Figure 4.5: Dc-dc converter buck operation during the ON stage.

The selection of the dc-link voltage is critical from the charger efficiency point of view. The switching losses of a MOSFET/IGBT increase proportionally with their operating voltage. Therefore, the dc-link voltage should be selected as low as possible to decrease the switching losses.

The selected dc-link voltage is 425 V considering the minimum required output voltage of the dc-dc converter which is 396 V. Considering the voltage drops in the dc-dc converter, for reliable operation, the minimum voltage should be at least in the range of 420 V to 430 V. The quiescent duty ratio of the converter is:

$$D = \frac{V_{bt}}{V_{dc}} = \frac{363}{425} = 0.85 \tag{4.21}$$

When S_5 in Fig. 4.5 turns on, the input current flows through the switch S_5, filter inductor (L_f) and to the filter capacitor (C_f) and Li-ion battery. The filter capacitor and battery are charged in this stage. The following equation is valid during this time interval:

$$t_{on} = \frac{\Delta I_L \cdot L_f}{V_{dc} - V_{bt}} \tag{4.22}$$

where t_{on} is the conduction time of the switch S_5 (s), and ΔI_L is the peak-to-peak filter inductor ripple current as shown in Fig. 4.6.

When S_5 turns-off, the inductor current circulates using the free wheeling diode D_6 as shown in Fig. 4.7. The filter capacitor discharges to the battery pack. The following equation is valid at this stage:

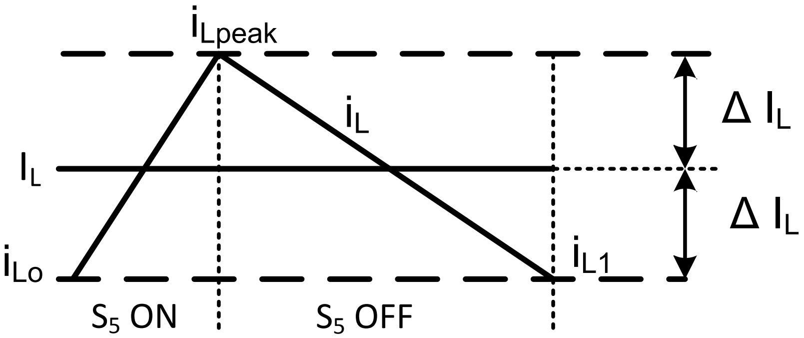

Figure 4.6: Filter inductor ripple current.

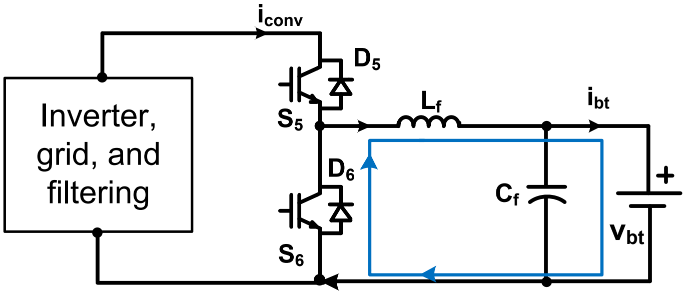

Figure 4.7: Dc-dc converter buck operation during the OFF stage.

$$t_{off} = \frac{\Delta I_L \cdot L_f}{V_{bt}} \tag{4.23}$$

where t_{off} is the blocking time of the switch S_5.

Combining (4.22) and (4.23) yields the required L_f value for a given switching frequency, and a ripple current value:

$$L_f = \frac{(V_{dc} - V_{bt})\, D}{2\, f_{sw}\, \Delta I_L} \tag{4.24}$$

where $1/f_{sw} = t_{on} + t_{off}$.

As a rule of thumb, the selected inductor peak-to-peak ripple current is 40% of the load current. Therefore, $\Delta I_L = 4$ A. For a switching frequency of 40 kHz, the calculated filter inductance value is 329 μH.

The maximum allowed rms voltage ripple (at switching frequency) observed at the battery terminals is calculated as follows:

$$\begin{aligned} \Delta V_{bt} &= R_{eq}\,\Delta I_{bt} \\ &= 1.1\,(0.1 \times 18) \\ &= 2.0\;Vpeak - peak \end{aligned} \tag{4.25}$$

where R_{eq} is total series internal resistance of the battery pack (Ω), and ΔI_{bt} is the peak-peak battery ripple current (A). The selection of the filter capacitor should result in a voltage ripple that has an rms value of less than 2.0 V at the nominal output voltage (363 V). An aluminum capacitor of 100 μF with an effective equivalent series resistance (R_{ESR}) of 0.6 Ω is selected. Assuming that all the ripple current is flowing through the capacitor will present the worst case peak-to-peak voltage ripple seen at the battery pack.

$$\begin{aligned} \Delta V_{bt} &= \Delta I_L \times (R_{ESR} + \frac{D}{f_{sw}\,C_f}) \\ &= 4 \times (0.6 + \frac{0.85}{40,000 \times 100 \times 10^{-6}}) \\ &= 3.25\;Vpeak - peak \end{aligned} \tag{4.26}$$

However, in reality, some of the ripple current flows into the battery pack further decreasing this voltage ripple. This will decrease the voltage ripple seen in the terminals of the battery pack. Therefore, the current design selection is suitable for 0.1C peak-to-peak output current ripple. Also, the current supplying capability of the capacitor is 2.3 A (rms) at 40 kHz which is much higher than the inductor ripple current (4 A peak-peak, 1.15 A rms). Therefore, the filter capacitor will stay in its operating temperature range.

4.4.2 DC-DC converter controller design

The purpose of the dc-dc converter controller is to meet the goals below.

- High loop gain at twice the grid frequency to filter out second harmonic ripple current at the output.
- One second transient response time for the battery current when a charging command is received. Slower transient response will decrease the required dc-link capacitance. However, it will not change the total charging time at all.
- For stability, a minimum phase margin of 30° is required.

The control signal to output voltage transfer function of the dc-dc converter during unidirectional operation is:

$$G_{vd}(s) = G_{d0} \frac{1}{1 + \dfrac{s}{Q_0\,\omega_0} + (\dfrac{s}{\omega_0})^2} \tag{4.27}$$

where $\omega_0 = 2\pi f_0$, f_0 is corner frequency, Q_0 is Q-factor, and G_{d0} is dc gain. Their mathematical definitions are as follows:

$$\begin{aligned} G_{d0} &= \frac{V_{bt}}{D} \\ &= \frac{363}{0.85} = 425\ V \\ &= 20\,log(425) = 52.5\ dB \end{aligned} \tag{4.28}$$

$$\begin{aligned} f_0 &= \frac{1}{2\pi\,\sqrt{L_f\,C_f}} \\ &= \frac{1}{2\pi\,\sqrt{(340 \times 10^{-6})\,(100 \times 10^{-6})}} \\ &= 863\ Hz \end{aligned} \tag{4.29}$$

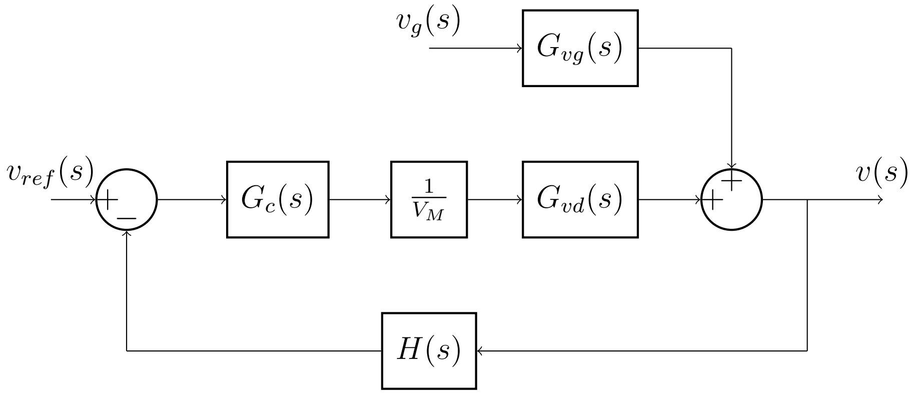

Figure 4.8: Dc-dc converter control diagram.

$$\begin{aligned} Q_0 &= R_{eq}\sqrt{\frac{C_f}{L_f}} \\ &= 1.1\sqrt{\frac{100\times10^{-6}}{340\times10^{-6}}} \\ &= 0.6 \end{aligned} \tag{4.30}$$

The open loop input voltage to output voltage transfer function is also important to evaluate the effect of second harmonic voltage ripple at the dc-link on the battery current.

$$G_{vg}(s) = G_{g0}\,\frac{1}{1+\dfrac{s}{Q_0\,\omega_0}+(\dfrac{s}{\omega_0})^2} \tag{4.31}$$

where $G_{vg}(s)$ is the dc gain and equal to D. This transfer function has the same poles with $G_{vd}(s)$. The closed loop gain of the system is defined as:

$$T(s) = \frac{H(s)\,G_c(s)\,G_{vd}(s)}{V_M} \tag{4.32}$$

The loop gain magnitude, $\|T(s)\|$, is a measure of how well the feedback system works. We want loop gain to be high so that the output voltage follows the input command without any steady state errors. A high loop gain also results in the attenuation of input disturbances. The designed closed-loop system transfer function Bode diagram is shown in Fig. 4.9.

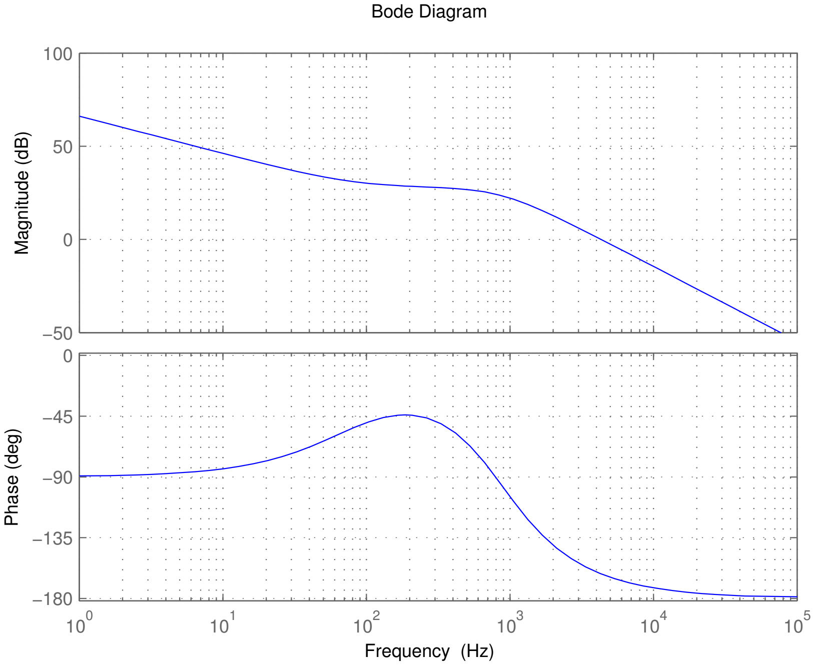

Figure 4.9: DC-DC converter control Bode diagram.

4.5 Total controller design

The total controller of the system should include various other controllers in addition to the previously described current controllers for ac-dc converter and dc-dc converter. The main goal of the controller is to follow active and reactive power commands that are sent by the utility. Therefore, additional controller loops are required to make sure that the charger always consumes the active power and reactive power levels requested by the utility.

Fig. 4.10 shows the total system design. It is a novel design in the way that it only receives two commands from the grid and adjusts the line current and battery current correspondingly. There are one outer loop to calculate the reference reactive power (Q_{ref}) and two outer loops to calculate the reference active power (P_{ref}) as shown in Fig. 4.10. The output of the active power controller has a minimum and a maximum limit of 200 V and 300 V for Level 1 charging, respectively. If the charging command, P_{cmd} increases, ${V_{dc}}^*$ increases and vice versa. Therefore, the dc-link voltage changes during the transition periods (when a command arrives from the grid). This change in the dc-link voltage helps to create a reference command for the battery charging current. If the dc-link voltage increases above V_{dcref} =250 V, the battery charging current increases to decrease the dc-link voltage back to 250 V. If the dc-link voltage drops below V_{dcref} =250 V, the battery charging current decreases to increase the dc-link voltage back to 250 V. Consequenly, when the dc-link voltage stays at V_{dcref}, it means that the system has input-output power balance.

Reference current calculation block uses the following equations in the given order to generate the magnitude and phase angle of the reference charging current (${i_c}^*$):

$$\theta = tan^{-1}\left(\frac{P_{ref}}{Q_{ref}}\right) \tag{4.33}$$

$$I_c = \left(\frac{P_{ref}}{V_s\, cos(\theta)}\right) \tag{4.34}$$

$${i_c}^* = \sqrt{2}\, I_c\, sin(\omega t + \theta) \tag{4.35}$$

Ac-dc converter has the following controllers:

- line current controller (PR)
- dc-voltage controller (PI)
- active power controller (PI)
- reactive power controller (PI)

Dc-dc converter has the following controllers:

- battery current controller (PI)
- power balance controller (PI)

Table 4.3 lists the values used for the associated PI parameters of the controllers for Level 1 operation.

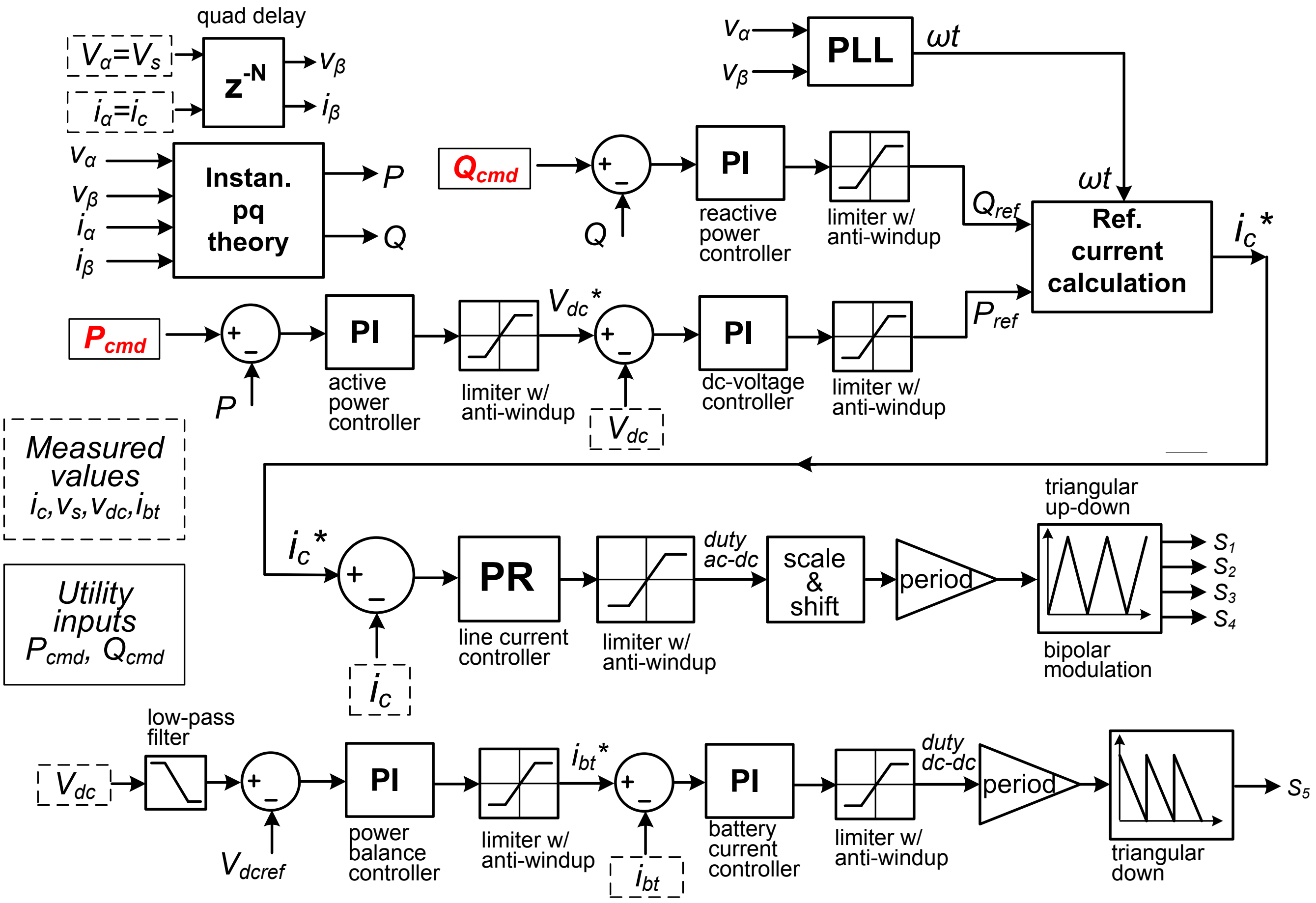

Figure 4.10: Schematic of the total controller.

Table 4.3: Parameters of the PI controllers.

Controller	K_P	K_I
Dc voltage controller	0.10	100
Active power controller	0.01	2.0
Reactive power controller	0.10	10.0
Battery current controller	0.20	10.0
Power balance controller	0.01	0.1

A single-phase PLL is used to synchronize with the grid voltage phase angle and instantaneous pq power theory is used to compute the average active and reactive power value including their directions. To achieve both operations, a quadrature axis is required. This axis is created by delaying the measured grid voltage and charger current by one fourth of the grid cycle.

Table 4.4: The system parameters used in Level 1 charger case.

Parameter	Symbol	Value
Charger apparent power	S	1.4 kVA
Grid voltage	V_s	120 V
Grid frequency	f	60 Hz
Coupling inductance	L_c	0.5 mH and 1.0mH
Switching frequency	f_{sw}	40 kHz
DC-link voltage	V_{dc}	425 V
DC-link capacitance	C_{dc}	432.5 μF
Battery side filter capacitor	C_f	100 μF
Battery side filter inductance	L_f	340 μH

4.6 Simulation Study

The simulation study serves two purposes: (1) to fulfill the closed-loop operation of the system as descried in this chapter, and (2) to verify the results of the mathematical analysis presented in Chapter 3, namely to investigate the effect of full reactive power operation on the charger for three different cases:

a) Level 1, 1.4 kVA charger, b) Level 2, 3.3 kVA charger, and c) Level 2, 6.6 kVA charger. Note that, a Level 1 charger is also evaluated in addition to two Level 2 chargers analyzed in Chapter 3. The analysis results are still valid for the Level 1 charger.

The effect of reactive power for a selected input coupling inductor values are verified in the simulation study. Level 1 charger uses 0.5 mH and 1.0 mH coupling inductors. Level 2 3.3 kVA charger uses 1.0 mH coupling inductors. Level 2 6.6 kVA charger uses 1.5 mH coupling inductor. All other system parameters are calculated based on the unidirectional charging operation and explained previously in this chapter.

4.6.1 Level 1 (1.4 kVA) charger

The designed system parameters for unidirectional PFC operation is shown in Table 4.4.

Two scenarios were simulated to reveal the effect of reactive power operation:

- P_s=1.4 kW and Q_s=0 kVAR charging-only operation for SOC=20% (CC charging stage).
- P_s=0 kW and Q_s=-1.4 kVAR full reactive power operation only.

The investigated system variables are:

- AC line current
- Battery charging current
- DC-link voltage ripple
- DC capacitor ripple current

The following sections describe each case and present the results.

P_s=1.4 kW and Q_s=0 kVAR charging only operation

The charging command starts with a ramp function that takes the battery charging current to its rated value (4.30 A) when the battery has 20% SOC. At this SOC level, the battery voltage is 324.5 V. Therefore, the battery charging power equals to $324.5 \times 4.30 = 1.4$ kW. There are two different design cases for the Level 1 charger. First is with 0.5 mH coupling inductor, and the second with 1.0 mH.

The ac line current during charging operation is shown in Fig. 4.11. The calculated THD for the line current for this operation is 4.67% for L_c=0.5 mH design case and 2.36% for L_c=1.0 mH design case. Therefore, the simulation verifies the goal attaining a less than 5% line current THD.

The dc-link voltage waveform is shown in Fig. 4.12. The greater second harmonic voltage ripple that the dc-link capacitor exhibits, the more distorted the battery charging current will be. Therefore, the dc-link voltage ripple must be limited to the specified battery charging requirements. The calculated (using (3.40)) and simulated

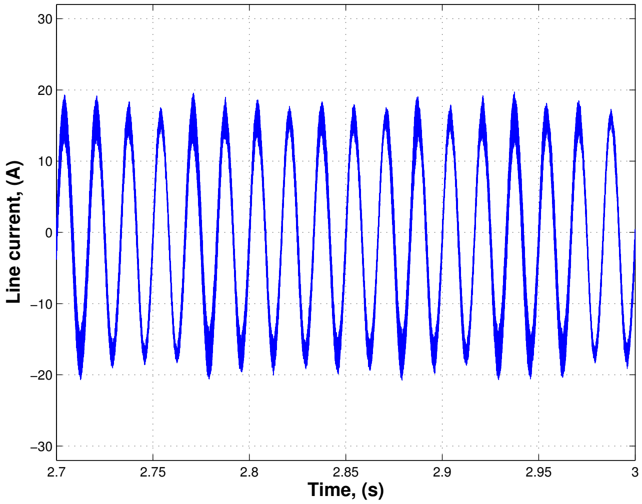

Figure 4.11: Line current for Level 1 P_s = 1.4 kW charging only operation (L_c=0.5 mH).

second harmonic dc-link peak-peak voltage ripple are listed in Table 4.5. As shown, the analysis and simulation results overlap very well.

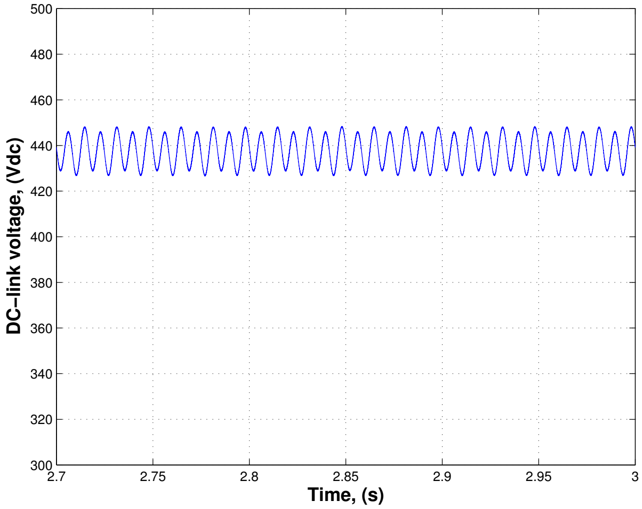

Figure 4.12: DC-link voltage for Level 1 P_s = 1.0 charging only operation (L_c=0.5 mH).

Next, the dc-link capacitor second harmonic ripple current was investigated. Fig. 4.13 shows the dc-link capacitor current during the charging operation. The

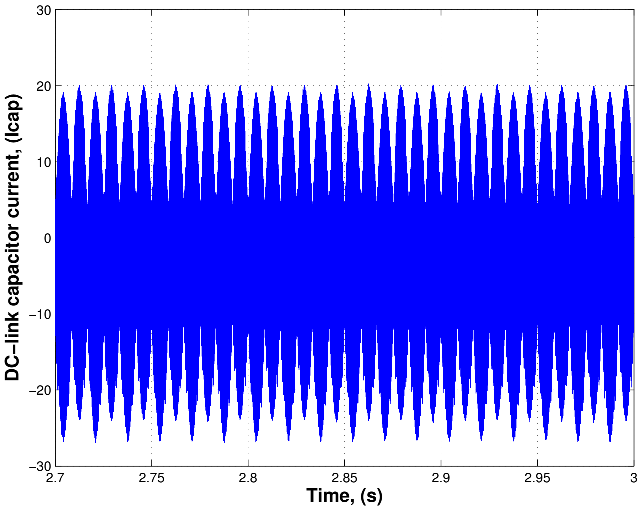

Figure 4.13: DC-link capacitor current for Level 1 $P_s = 1.0$ charging only operation (L_c=0.5 mH).

amount of rms second harmonic ripple current on the dc-link capacitor during steady-state operation attained by the simulation is 2.56 A for L_c=0.5 mH and 2.50 A for L_c=1.0 mH. The analytical values calculated using (3.44) are 2.26 A and 2.56 A, respectively (Table 4.5).

Table 4.5: Result of charging only operation for Level 1 charger.

Parameter	Analysis result		Simulation result	
	L_c=0.5 mH	L_c=1.0 mH	L_c=0.5 mH	L_c=1.0 mH
DC-link peak-peak voltage ripple, ΔV_{dc}	19.6 V	20 V	18.9 V	19.2 V
DC-link capacitor ripple current, I_{cap}	2.26 A	2.30 A	2.56 A	2.50 A

The last figure shows the battery charging current in Fig. 4.14. The battery current harmonic components are listed in Table 4.6. The battery current meets the goals set in the beginning of this chapter. The second harmonic ripple current is less than 4%, and the rms sum of PWM ripple current is less than 10% of the rated charging current which is 18 A for the selected Li-ion battery cell. Therefore, the charger fulfills the goal of charging the battery by achieving the harmonic standards.

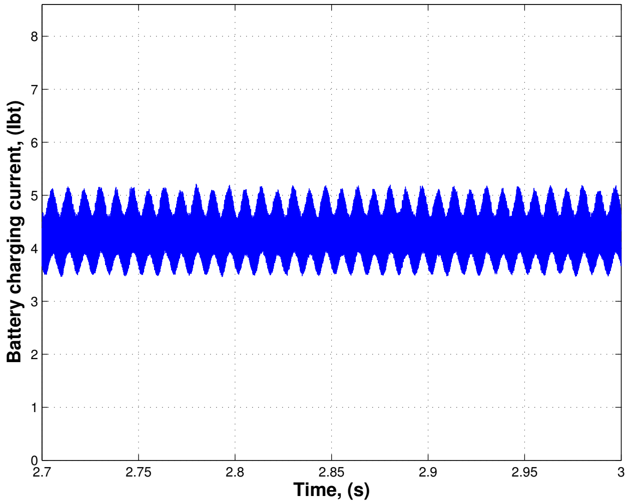

Figure 4.14: Battery charging current for Level 1 $P_s = 1.0$ charging only operation (L_c=0.5 mH).

Table 4.6: The battery charging current harmonic component summary for Level 1 charger.

Parameter	Value		Percentage of rated charging current	
	L_c=0.5 mH	L_c=1.0 mH	L_c=0.5 mH	L_c=1.0 mH
DC component	4.3 A	4.3 A	24% (0.24C)	24% (0.24C)
120 Hz component	0.16 A	0.17 A	0.89%	0.94%
RMS sum of PWM ripple components	0.28 A	0.31	1.5%	1.7%

In the following section, the Level 1 charger will be operated in full capacitive operation mode, and the same circuit variables will be investigated.

P_s=0 kW and Q_s=-1.4 kVAR capacitive power only operation

The line current THD observed in this operation mode is 5.37% for a 0.5 mH inductor and 3.93% for a 1.0 mH inductor. The battery charging current is zero for this case. The dc-link variables are compared with the mathematical analysis results presented by the equations in Chapter 3. The results are presented in Table 4.7.

Table 4.7: Result of full-reactive power operation for Level 1 charger.

Parameter	Analysis result L_c=0.5 mH	 L_c=1.0 mH	Simulation result L_c=0.5 mH	 L_c=1.0 mH
DC-link peak-peak voltage ripple, ΔV_{dc}	19.8 V	20.7 V	18.8 V	19.7 V
DC-link capacitor ripple current, I_{cap}	2.28 A	2.39 A	2.40 A	2.52 A

4.6.2 Summary of effect of reactive power operation on Level 1 1.44 kVA charger

The results of two design cases (0.5 mH and 1.0 mH) reveal that the reactive power operation of the Level 1 charger does not affect ΔV_{dc} and I_{cap} even in the worst case (full capacitive operation mode, Q_s=-1.4 kVAR) at any considerable level. The battery charging is safe at any point of the PQ power plane provided that the charger power rating is not exceeded. Therefore, a Level 1 charger can be operated at any point of its PQ plane as it is needed by the utility grid.

4.6.3 Level 2 (3.3 kVA) charger

The Level 2 charger input voltage is 240 V and its input power is 3.3 kVA. The coupling inductance selected for this charger is 1.0 mH. All the other parameters are the same with the Level 1 charger and are presented in Table 4.4.

P_s=3.3 kW and Q_s=0 kVAR charging only operation

The ac line current is shown in Fig. 4.15 for this operation mode. The measured THD is 5.3%. The dc link voltage during the operation is shown in Fig. 4.16. The rms current ripple of the dc link capacitor is shown in Fig. 4.17. The results of dc-link variables are listed in Table 4.8. The simulation results coincide with the analytical results presented in Chapter 3. DC-link peak-to-peak ripple voltage and dc-link rms

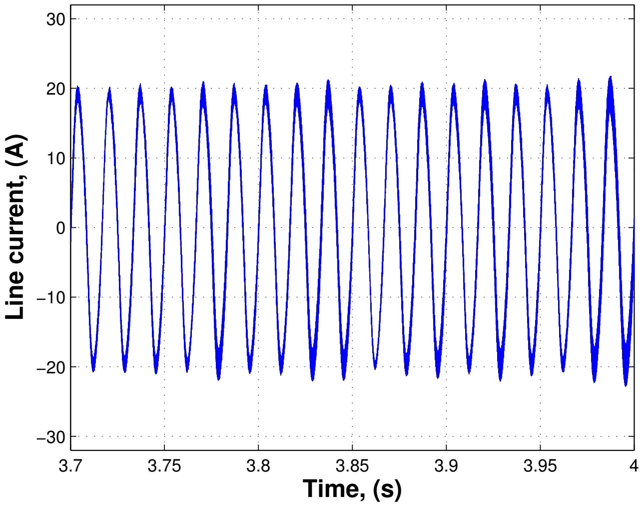

Figure 4.15: Line current for Level 2 3.3 kVA $P_s = 1.0$ charging only operation (L_c=1.0 mH).

Table 4.8: Result of charging-only operation for Level 2 3.3 kVA charger.

Parameter	Analysis result	Simulation result
DC-link peak-peak voltage ripple, ΔV_{dc}	49.1 V	47.2 V
DC-link capacitor ripple current, I_{cap}	5.66 A	5.64 A

Table 4.9: The battery charging current harmonic component summary for Level 2 3.3 kVA charger.

Parameter	Value	Percentage of rated charging current
DC component	10 A	55% (0.55C)
120 Hz component	0.48 A	2.7%
RMS sum of PWM ripple components	1.80 A	10%

ripple current values measured in the simulation and calculated using (3.40) and (3.44) are very close to each other.

The battery charging current is illustrated in Fig. 4.18. Its harmonic components are summarized in Table 4.9. Using the battery model described before, the converter fulfills the battery charging requirements set earlier.

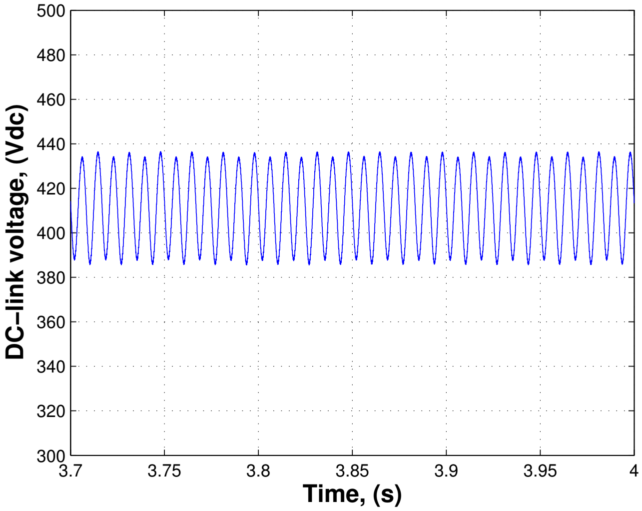

Figure 4.16: DC-link peak-peak voltage ripple for Level 2 3.3 kVA $P_s = 1.0$ charging only operation (L_c=1.0 mH).

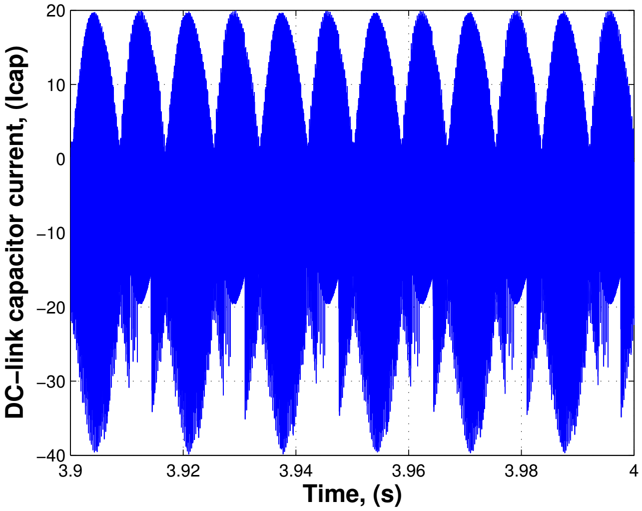

Figure 4.17: DC-link capacitor current ripple for Level 2 3.3 kVA $P_s = 1.0$ charging only operation (L_c=1.0 mH).

4.6.4 Summary and discussion of effect of reactive power operation on Level 2 3.3 kVA charger

Comparing the results for charging-only operation and full capacitive operation, the major changes in the operation of the circuit is the increase in the dc-link capacitor

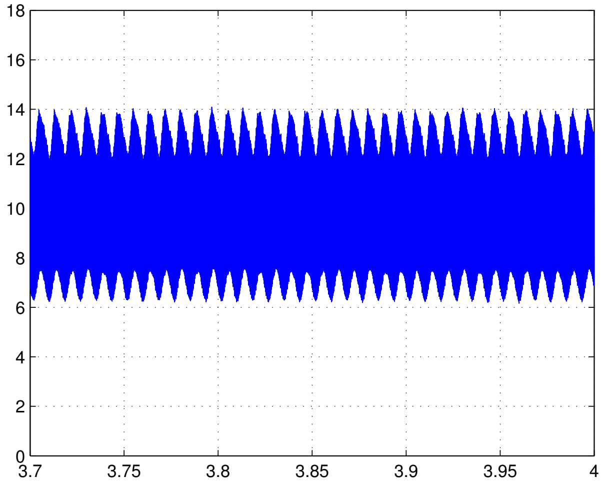

Figure 4.18: Battery charging current for Level 2 3.3 kVA P_s = 1.0 charging only operation (L_c=1.0 mH).

second harmonic current ripple and increased voltage ripple at the dc-link. The net changes overlap with the mathematical analysis results in Chapter 3. The dc-link second harmonic current ripple and voltage ripple showed a net increase of 2.1% after simulation analysis. This was calculated and shown in Fig. 3.10 for L_c=1 mH case in Chapter 3.

The net effect of full-reactive power operation on the dc-link components is concluded to be negligible using an L_c=1.0 mH coupling inductor design for 3.3 kVA Level 2 charger. Furthermore, the maximum ripple seen on the dc-link satisfies the battery charging requirements for the same battery output filter used for charging-only operation. The input voltage to output voltage attenuation of the dc-dc converter is enough to filter out increased second harmonic voltage ripple on the dc-link satisfying safe charging operation of the battery. Therefore, if charging operation is required at any point of the PQ power plane, even during a very high capacitive power operation (i.e. Q_s=-2.97 kVAR and P_s=1.42 kW), the charging current harmonics will still stay below the requirements.

Quantitatively, the second harmonic battery current ripple in this case is

$$\begin{aligned} \Delta V_{bt} &= \Delta V_{dc} \times (-32dB) \\ &= 48 \times 0.0251 \\ &= 1.2\ Vp-p \end{aligned} \tag{4.36}$$

Note that -32 dB was calculated previously during the dc-dc converter design parameters and ΔV_{dc} is computed using (3.40) for Q_s=-2.97 kVAR and P_s=1.42 kW. Using the battery model developed previously, the above result corresponds to a 0.42 A rms second harmonic current ripple. This is 2.37% of the rated charging current and below the maximum allowed ripple value.

4.6.5 Level 2 (6.6 kVA) charger

Level 2 charger input voltage is 240 V and its input power is 6.6 kVA. The coupling inductance selected for this charger is 1.5 mH. The required dc-dc converter output filter inductance is increased to 680 μH to reduce high frequency harmonics of the battery charging current. The dc link capacitance is increased to 865 μF as explained in the previous chapter.

P_s=6.6 kW and Q_s=0 kVAR charging only operation

The ac line current is shown in Fig. 4.19 for this operation mode. The measured THD is 2.80%. The dc link voltage during the operation is shown in Fig. 4.20. The current ripple of the dc link capacitor is shown in Fig. 4.21. The simulation results of dc-link variables are listed in Table 4.10 and compared with the analysis results.

The battery charging current is illustrated in Fig. 4.22. Its components are summarized in Table 4.11.

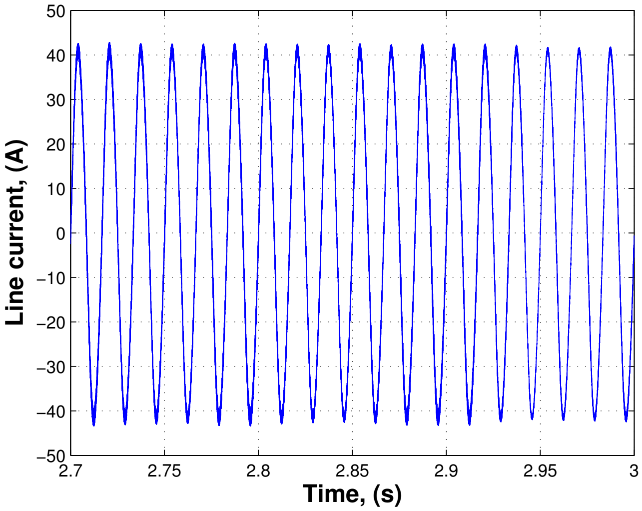

Figure 4.19: Line current for Level 2 6.6 kVA $P_s = 1.0$ charging only operation (L_c=1.5 mH).

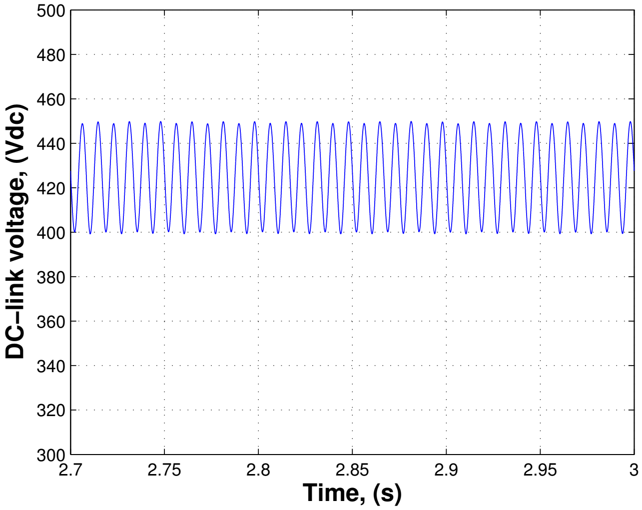

Figure 4.20: DC-link voltage for Level 2 6.6 kVA $P_s = 1.0$ charging only operation (L_c=1.5 mH).

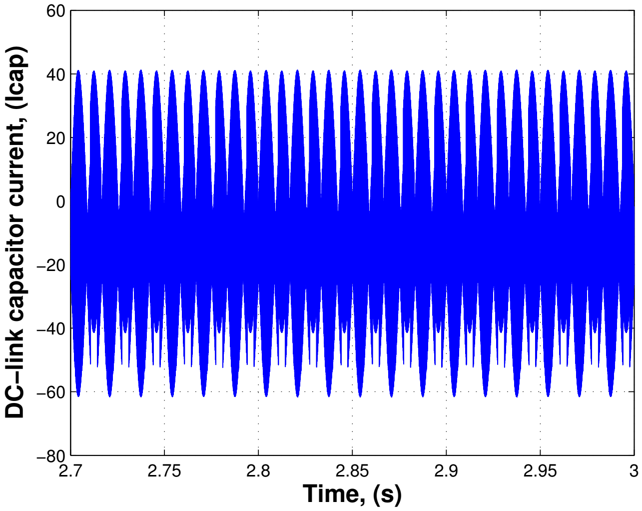

Figure 4.21: DC-link capacitor current for Level 2 6.6 kVA $P_s = 1.0$ charging only operation (L_c=1.5 mH).

Table 4.10: Result of charging-only operation for Level 2 6.6 kVA charger.

Parameter	Analysis result	Simulation result
DC-link peak-peak voltage ripple, ΔV_{dc}	47.7 V	49.5 V
DC-link capacitor ripple current, I_{cap}	12 A	11 A

Table 4.11: The battery charging current harmonic component summary for Level 2 6.6 kVA charger.

Parameter	Value	Percentage of rated charging current
DC component	20 A	110% (1.1C)
120 Hz component	0.47 A	2.7%
RMS sum of PWM ripple components	negligible	–

4.6.6 Summary of effect of reactive power operation on Level 2 6.6 kVA charger

The 6.6 kVA charger with L_c=1.5 mH design case shows some change in dc-link variables between charging only operation and full capacitive operation. Those are listed below:

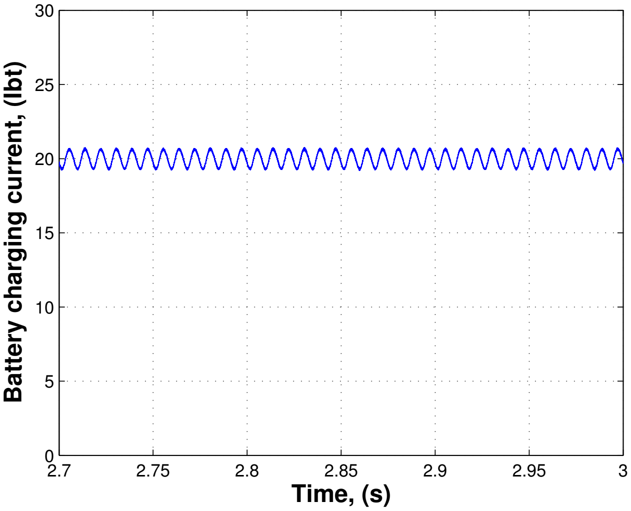

Figure 4.22: Battery charging current for Level 2 6.6 kVA $P_s = 1.0$ charging only operation (L_c=1.5 mH).

- DC-link second harmonic current ripple: I_{cap} changes from 11 A to 11.7 A which is a 6.3% increase.
- DC-link voltage ripple increase: V_{dc} displays a change from 47 V to 50.7 V which is again a 6.3% increase.
- The attenuation of the effect of dc-link voltage ripple to the output of dc-dc converter is -32 dB at 120 Hz. The worst case 120 Hz charging current component is calculated using the highest peak-peak voltage ripple at the dc-link as follows:

$$\begin{aligned} \Delta V_{bt} &= \Delta V_{dc} \times (-32dB) \\ &= 50.7 \times 0.0251 \\ &= 1.27\ Vp-p \end{aligned} \tag{4.37}$$

This corresponds to a 0.45 A rms current ripple which is 2.47% of the rated current. Even in this worst case condition, the battery charging could be achieved without exceeding the limits.

In conclusion, the 6.6 kVA charger can work in full symmetric four quadrant operation in PQ plane with ripple current capacity increase in the dc link capacitor using a 1.5 mH coupling inductor. If larger input inductances are used for the input filter design of the charger, the current ripple requirement will increase according to (3.44).

4.7 Summary and Conclusion of the Chapter

There are three different chargers under investigation in this chapter: Level 1 1.4 kVA charger, Level 2 3.3 kVA charger, and Level 2 6.6 kVA charger. The chapter includes the simulation of all of the chargers in full capacitive mode of operation. The results show and verify the maximum amount of reactive power can be achieved with no change in Level 1 1.4 kVA and Level 2 3.3 kVA chargers and minimal change in Level 2 6.6 kVA charger (6.3% increase in current requirement of system dc-link capacitor). The battery charging is free of any disturbance for all three designs which means that the initial charging requirements are satisfied. In other words, all of the three systems operate while there is no compromise in charging and grid current quality.

Chapter 5

Design and Experimental Verification of Bidirectional Charger with Reactive Power Operation

5.1 Introduction to Experimental Set-up

The system is designed using a modular structure. The layout design starts with configuring the placement of the semiconductors on the heat-sink. Each of the phase leg unit is identical to each other. Fig. 5.1 shows the layout of the MOSFETs and diodes. Each string corresponds to one phase-leg unit. The technical parameters of the MOSFET and SiC diode are presented in Table 5.1. All of the boards are designed using Altium Designer and fabricated in Sierra Proto Express, a printed circuit board (PCB) manufacturer.

Each phase leg has the identical gate drive units. Each gate drive unit per phase leg is mounted on the phase-leg MOSFETs mechanically using the SOT-227 package outline of the MOSFETs. Then, the SiC Schottky diodes are soldered to each of the

Figure 5.1: Lay-out of the MOSFETs and SiC Diodes.

Table 5.1: Specifications of APT34M120J Si MOSFET (by Microsemi) and C2D20120D SiC Schottky Diode (by Cree) used in the design of the bidirectional charger.

Diode Parameters				
Symbol	Parameter	Value	Unit	Conditions
V_{RRM}	Repetitive peak reverse voltage	1200	V	
I_F	Average forward current	20	A	$T_c = 150$ °C
		34		$T_c = 125$ °C
R_d	Equivalent on resistance	93.75	$m\Omega$	$T_c = 75$ °C
V_{fd}	Equivalent forward voltage drop	0.75	V	$T_c = 75$ °C
Mosfet Parameters				
Symbol	Parameter	Value	Unit	Conditions
I_D	Continuous drain current	22	A	$T_c = 25$ °C
		34	A	$T_c = 100$ °C
$V_{BR(DSS)}$	Drain-source breakdown voltage	1200	V	
$R_{DS(on)}$	Drain-source on resistance	0.30	Ω	
t_r	Current rise time	60	ns	
t_f	Curent fall time	90	ns	

gate drive boards. The power board is mechanically mounted on the gate drive boards which provided a strong connection. The digital signal processor (DSP) interface board is mechanically mounted on the power board and the DSP is mounted mechanically on the interface board.

In this study, a floating point Texas Instruments (TI) C2000 F28335 DSP is used for easy and fast code developing feature of floating-point coding. Code Composer Studio V5.1 is used to compile and download the code to the DSP.

The modular structure of the charger provided flexibility in developing the system by easily replacing the faulty modules. Each of the modular units are described in the following sections.

5.2 Gate Drive Board

The gate drive board includes two units for upper and lower MOSFETs. Each unit has the circuit configuration shown in Fig. 5.2. The PWM input to the unit comes from the DSP interface board after protection processing. The PWM input shares the same ground for low-power level logic circuits. The ADuM 5241 isolator is used to isolate logic-level ground from the MOSFET source. Only one channel of the isolator is used here. The on-chip isolated power output of the isolator is not used. The logic-level output of the isolator is connected to the gate drive chip. Gate drive chip is powered by a 12 V-to-15 V isolated dc-dc converter by Murata Power. It has 70 pF isolation capacitance.

The gate resistance is selected to be 20 Ω to limit di/dt noise. The gate drive chip has a maximum current output of 9 A and it is capable of supplying the required gate current. However, it is important to mention that the capacitors connected to the supply of the gate drive should have enough values to supply instantaneous current at the switching instant to prevent any dips in the gate voltage. In this study, 47 μF, 10 μF, and 1 μF tantalum capacitors and 0.1 μF ceramic capacitor are used for each gate drive chip. The loop that is shown with the red line in Fig. 5.2 is kept as short as possible to reduce inductance introduced by the traces. Two back to back connected zener diodes are used to protect MOSFET gate from any positive or negative spikes.

The first version of the gate drive board is shown in Fig. 5.3. In this version, the ADuM 5241 isolator could not achieve isolation that is required by the upper

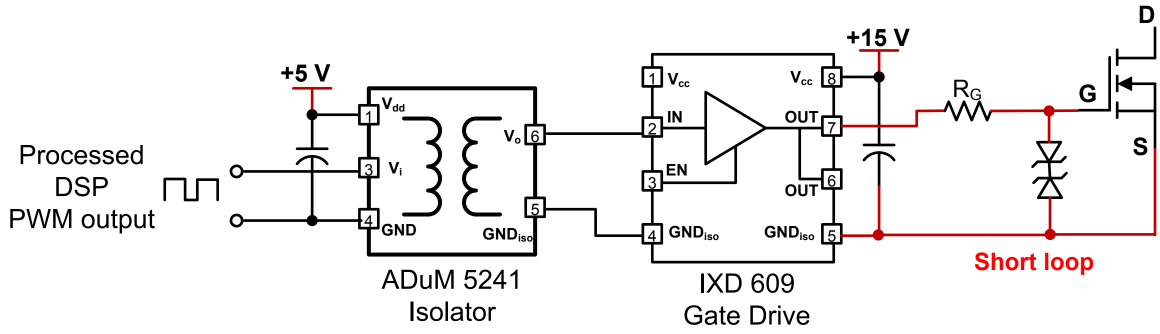

Figure 5.2: Gate drive circuit.

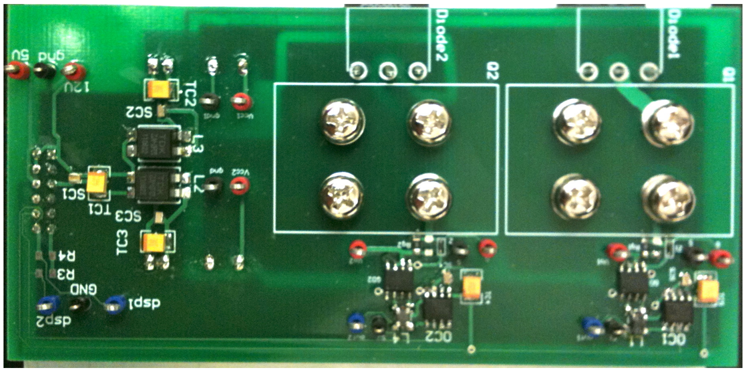

Figure 5.3: First version of the gate drive circuit.

MOSFET. After rigorous testing, it is concluded that a layout problem during the PCB design has occurred disrupting the isolation. Therefore, a second version of the gate drive board is designed and tested. The revised version is shown in Fig. 5.4 and it is installed on top of the SOT-227 MOSFET package.

5.3 Main Power Board

The main power board includes power circuit connections (ac-side, battery-side, optional dc-source connection, and ac and dc inductors), protection fuses, bleeder resistors for the electrolytic capacitors, voltage and current sensors, post-sensor signal scaling and shifting circuits, connections to gate drive circuits, and DSP interface board connection.

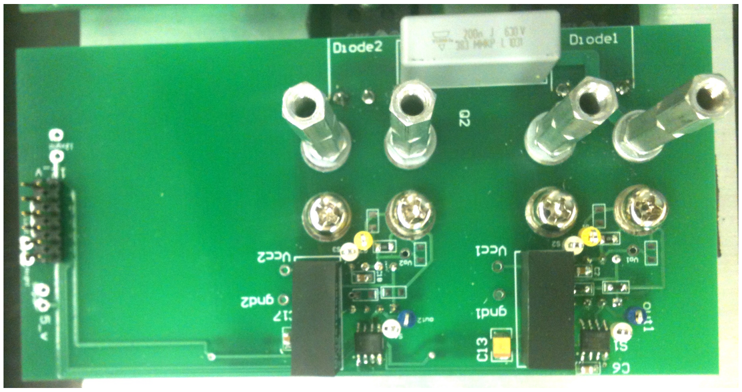

Figure 5.4: Second version of the gate drive circuit.

The first version of the power board has been revised to reduce the sensor output traces and included a shorter connection with the DSP interface board. Some of these elements of the power board are described in the following sections.

5.3.1 Voltage measurements

The first choice for the voltage sensing equipment was an Analog Devices AD204 isolation amplifier. However, the performance of the AD204 was not as good as expected to reduce the EMI noise during the operation of the charger especially, at higher power levels. Therefore in the second version, a LEM LV-20P isolated voltage transducer is used for the voltage measurements which are grid voltage, dc-link voltage, and battery voltage.

Figure 5.5 shows the configuration of the voltage sensor used. The values used for the voltage sensing circuitry is given in Table 5.2 for different voltage measurements. The final scaling is done in the interface board just before the analog to digital converter (ADC) of the DSP.

5.3.2 Current measurements

There are two current measurements in the circuit: one is the grid current and the other is the battery current. The first current sensor used for the circuit was a LEM

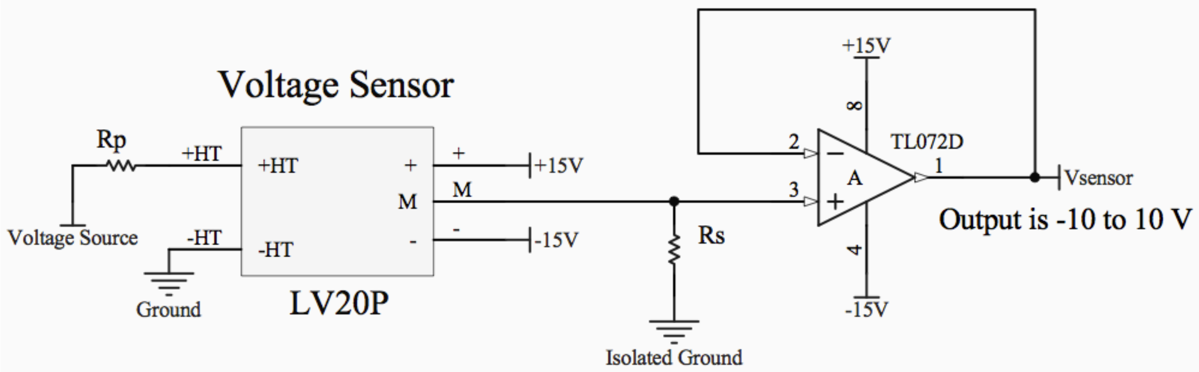

Figure 5.5: Voltage sensor circuit.

Table 5.2: The parameters of the voltage sensor circuit.

Parameter	Grid voltage sensor param.	DC-link voltage sensor param.	Battery voltage sensor param.
Sensor range	-340 - 340 V	0 - 500 V	0 - 200 V
Primary resistance (R_p)	33k Ω	40k Ω	20k Ω
Secondary resistance (R_s)	300 Ω	300 Ω	300 Ω

lts25-np hall effect current sensor. However, the output voltage range of the sensor was limited to 1.5 V for ±15 A instantaneous current measurement. The voltage measurement rate is 0.05 V/A which made the sensor prone to noises. Therefore, LEM HY15P current sensor is used for the revised design. This sensor has an output voltage range of 8 V for ±17 A instantaneous current measurement. Therefore, it has 0.235 V/A measurement rate, almost five times the previous sensor. It can measure ±45 A of instantaneous current.

LEM HY15P provides galvanic isolation between primary power circuit and the secondary signal circuit. The current sensor output does not have another stage at the main board and directly connected to the interface board.

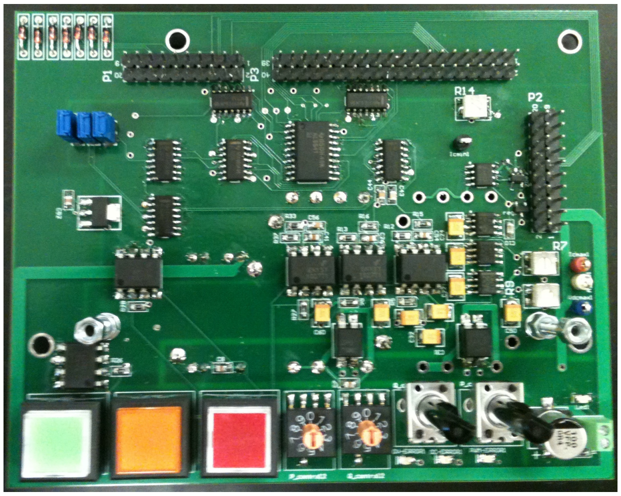

Figure 5.6: DSP interface board circuit revision 1.

5.4 DSP Interface Board

The interface board serves two purposes. One is to filter, shift, and scale the analog measurements so that they are suitable for 0-3 V analog input of the ADC. The second purpose is to provide protection for the system if a faulty operation occurs.

The first version of the interface board was designed and shown in Fig. 5.6. However, long analog traces caused increased noise on top of the analog measurement signals. Therefore, a second revised version is designed and shown in Fig 5.7.

The following protections are embedded in this interface board:

- PWM shoot through protection: if two gate signals of the same phase leg turn on at the same time, a PWM error signal is generated, and all of the six gate signals turn off. A light emitting diode (LED) signal is generated to warn the user that a PWM shoot through has happened.

- Grid over-current protection: if the line current goes above the maximum value limited by the protection circuit either in a positive or in a negative cycle, an over-current signal is generated, and all of the six gate signals turn off. An LED signal is generated to warn the user that an over-current error has happened.

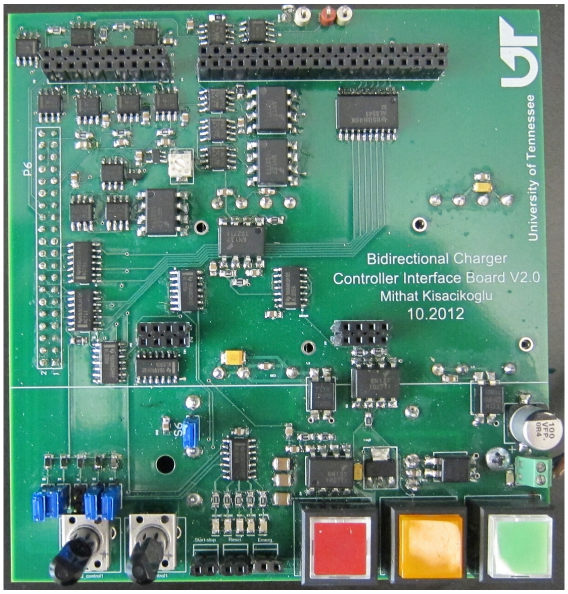

Figure 5.7: DSP interface board circuit revision 2.

- DC-link over-voltage protection: if the dc-link voltage goes above the maximum value set by the protection circuit, an over-voltage signal is generated and all of the six gate signals turn off. A LED signal is generated to warn the user that an over-voltage error has happened.

- Battery pack over-voltage protection: if the battery pack voltage goes above the maximum value set by the protection circuit, an over-voltage signal is generated, and all of the six gate signals goes off. A LED signal is generated to warn the user that an over-voltage error has happened.

- Battery over-current protection: if the battery current goes above the maximum value limited by the protection circuit either during charging or discharging, an over-current signal is generated, and all of the six gate signals turn off. A LED signal is generated to warn the user that an over-current error has happened.

- Emergency stop button: if for any reason the user wants to stop the operation of the circuit, it can directly do so by pressing the emergency stop button shown as the red push button in Fig. 5.6. The emergency button opens all of the switches instantly.

All of the protection items can be temporarily turned off for testing purposes using the blue jumpers shown in Fig. 5.6. The orange reset button can be used to reset all of the error signals after fixing the corresponding problem of the circuit. The interface board also includes a start button shown with the green color in Fig. 5.6. When the DSP receives the signal from the start button, it goes into soft start mode to start the operation of the system.

5.5 Total System Integration

Fig. 5.8 shows the final configuration of the charger. As shown, the interface board and the DSP are placed very close to the sensors providing shorter lengths for the sensor-to-ADC traces. Fig. 5.9 also shows the side view of the charger. Fig. 5.10 also provides a view of the charger from an angle.

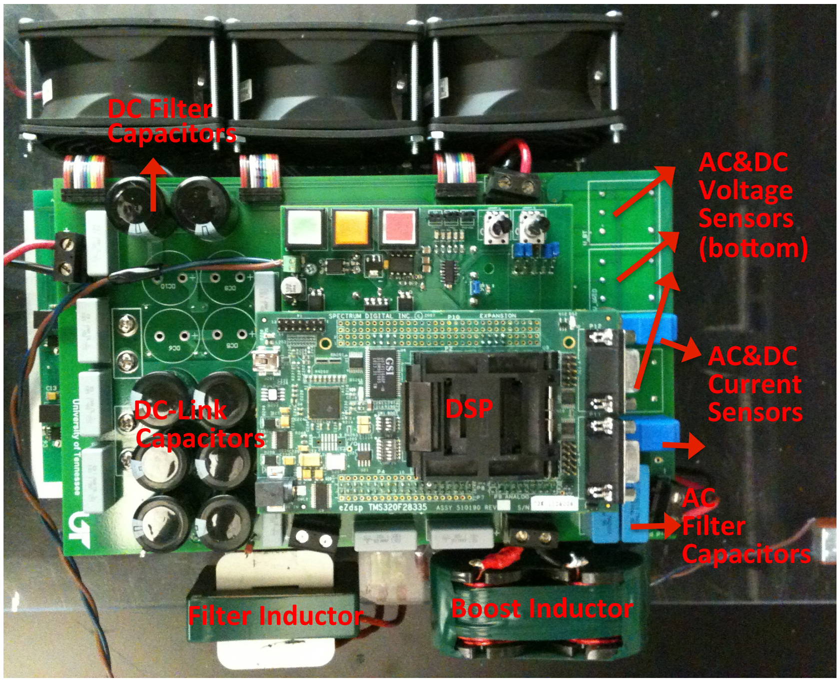

Figure 5.8: Final configuration of the charger (top view).

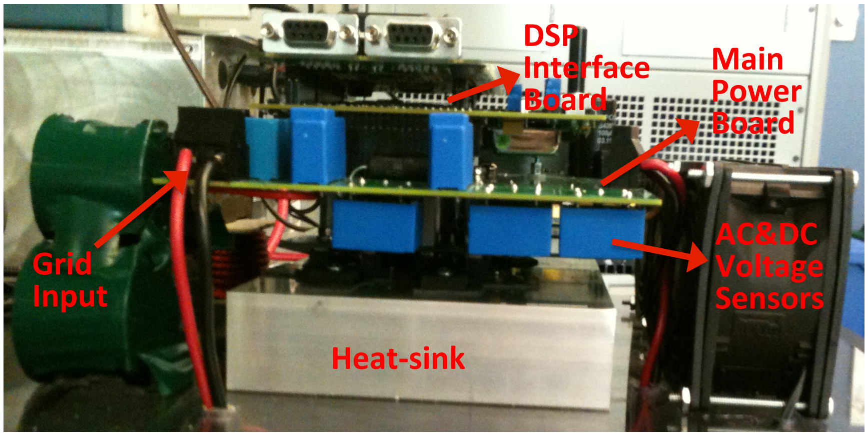

Figure 5.9: Final configuration of the charger (side view).

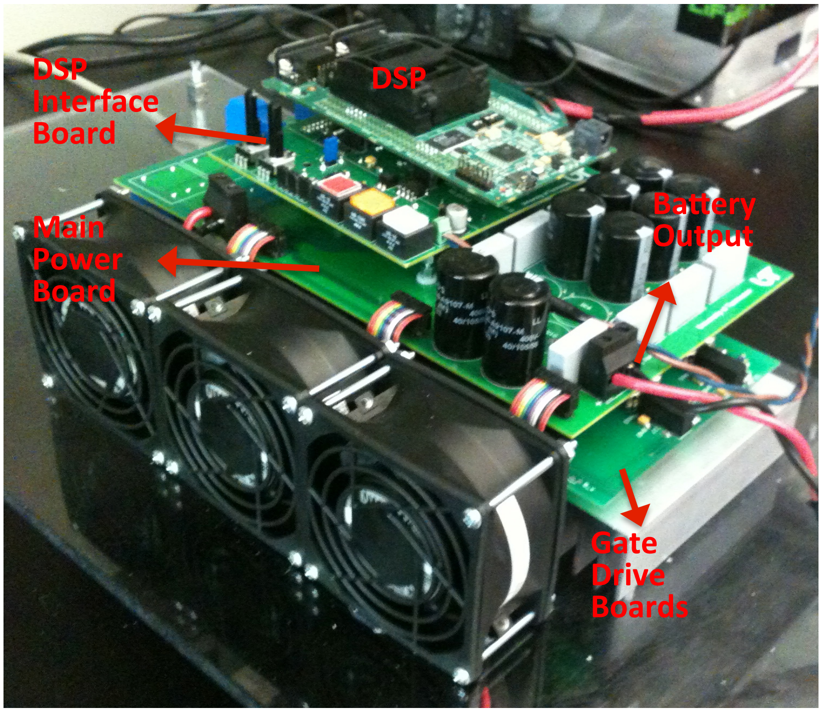

Figure 5.10: Final configuration of the charger (angle view).

5.6 Code development

Before going into the implementation stage, the controller code is first tested and developed using PSIM. Fig. 5.11 shows the ac-dc converter and the c-code development. The PSIM environment for code development helped with the following items:

- easy transfer of the controller code from simulation to hardware
- very similar behavior is possible to observe
- more efficient and less costly debugging process

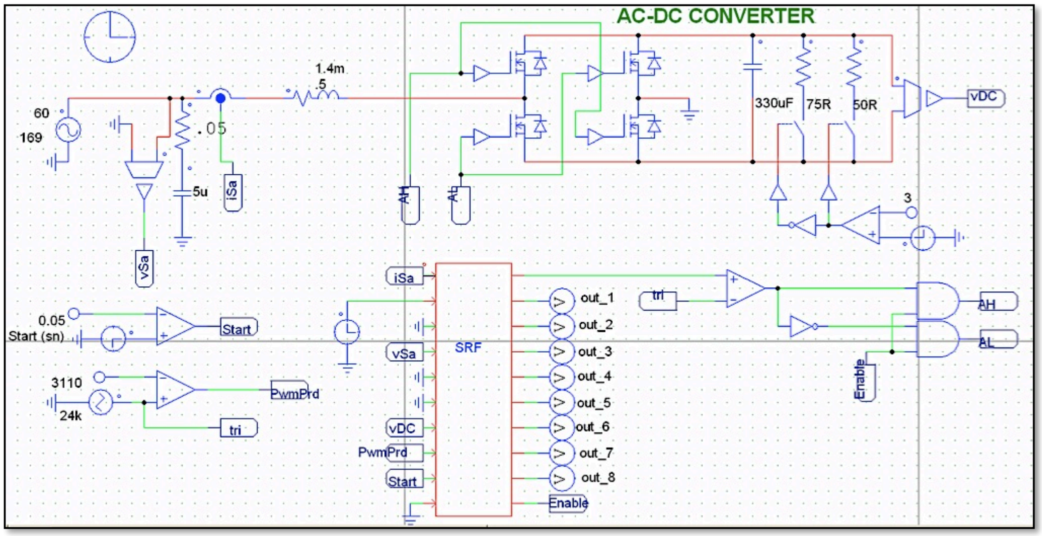

Figure 5.11: Code development using PSIM.

The hardware interrupt is emulated as PwmPrd in Fig. 5.11. It calls for the execution of the closed loop control at every period event, similar to the real DSP execution. The main c code, definitions, all the modules and Run code is embedded in the simulation using the c-code module of PSIM (shown as SRF block in Fig. 5.11).

5.7 Controller Implementation in the DSP

After the development of the C code, the code is transferred to the DSP. The C code to control the system is downloaded to the DSP using Code Composer Studio v5.1.The system clock frequency is defined to be 150 MHz. The system controller flow diagram is shown in Fig. 5.12. Fig. 5.12 shows how the main code of the system works. The system main code initializes the system, configures the DSP, and operates in an infinite while loop until the start button is pushed. If the conditions of Fig. 5.12

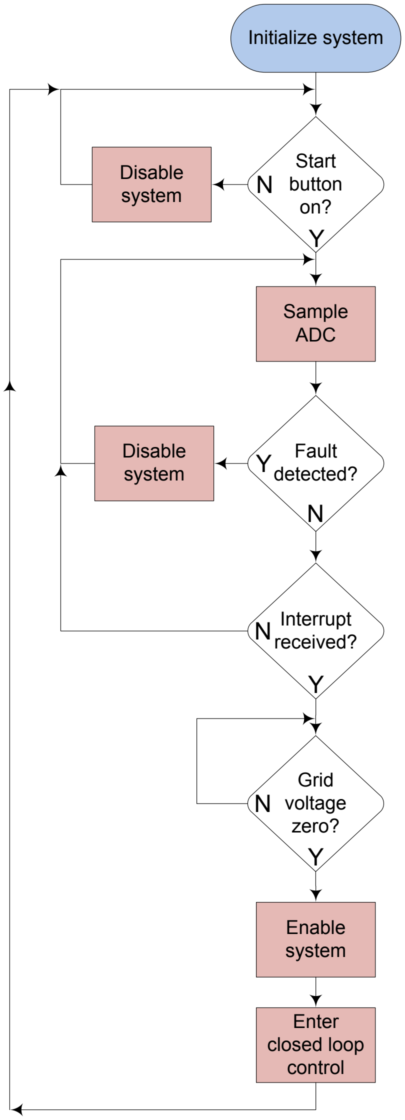

Figure 5.12: Controller C-code flow chart.

are met, the system enters into the closed loop function. The initialization code first loads the header and c files for configuring the DSP and the definition of the functions used by the code. The system is configured at a switching frequency of 24 kHz.

The system starts with pushing the start button and can be stopped with pushing the start button again anytime. Three ePWM modules are used to drive the six switches: ePWM1, ePWM2, and ePWM3. The dead-band generator module is used to create dead-band between the upper and lower switches of the ac-dc converter.

Table 5.3: The system parameters of the designed charger.

Parameter	Symbol	Value
Charger apparent power	S	3.3 kVA
Grid voltage	V_s	120/240 V
Grid frequency	f	60 Hz
Coupling inductance	L_c	1.0 mH
Switching frequency	f_{sw}	24 kHz
AC filter capacitance	C_{ac}	10 μF
DC-link voltage	V_{dc}	250 V (Level 1) 400 V (Level 2)
DC-link capacitance	C_{dc}	330 μF
Battery side filter capacitor	C_f	200 μF
Battery side filter inductance	L_f	0.4 μH

The third-leg used for the dc-dc converter is driven separately and only one switch is active at a time and the other switch is off all the time. ePWM1 and ePWM2 use up-down counter and bipolar modulation is realized. When the maximum point of the up-down counter is reached, it equals to 3125 counts. This corresponds to a switching frequency of 24 kHz which is the ac-dc converter switching frequency.

5.8 Experimental Analysis

The experiment is completed for three different operation modes: a)charging operation, b) charging and capacitive operation, and c) charging and inductive operation.

The charger designed is Level 1 and Level 2 compatible and can accept either 120 V or 240 V voltage input and rated at 13.75 A grid current rating. The maximum power that it can accept is 3.3 kW. Other parameters of the charger are listed in Table 5.3. Results show line voltage ($v_s(t)$) in navy, charger current (i_c) in light blue, dc-link voltage (V_{dc}) in green, and battery current (i_{bt}) in magenta.

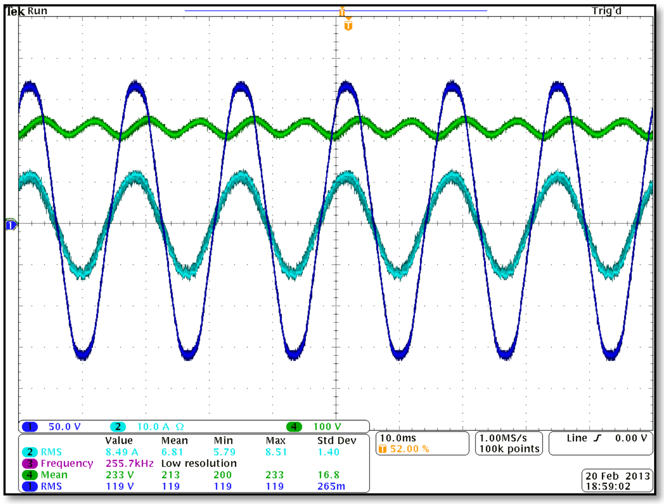

	Value	Mean	Min	Max	Std Dev
2 RMS	8.49 A	6.81	5.79	8.51	1.40
3 Frequency	255.7kHz	Low resolution			
4 Mean	233 V	213	200	233	16.8
1 RMS	119 V	119	119	119	265m

Figure 5.13: AC-DC converter operation with dc load.

5.8.1 Charging only operation

The system is tested at Level 1, 1.0 kW charging only operation. Fig. 5.13 shows the ac-dc converter operation. As shown in Fig. 5.14, the line current is in line with the utility voltage satisfying almost a unity displacement power factor. The THD calculated for this current is less than 5%.

Fig. 5.14 shows the operation of the total charger including the dc-dc converter. The controller for the whole system satisfies stable operation by converging to an equilibrium point. Charging current stays around 5 A, dc link voltage is around 250 V, and line current settles around 8.5 A rms during Level 1 charging operation. The total efficiency of the charger is 90%. The converter is run for more than five minutes to make sure that it does not diverge from the equilibrium point.

5.8.2 Charging and capacitive operation

Fig. 5.15 shows the operation of the ac-dc converter for charging and capacitive operation mode. The charging power command for the controller is P_s=1.1 kW, and the reactive power command is Q_s=-0.5 kVAR. The controller satisfies the stable

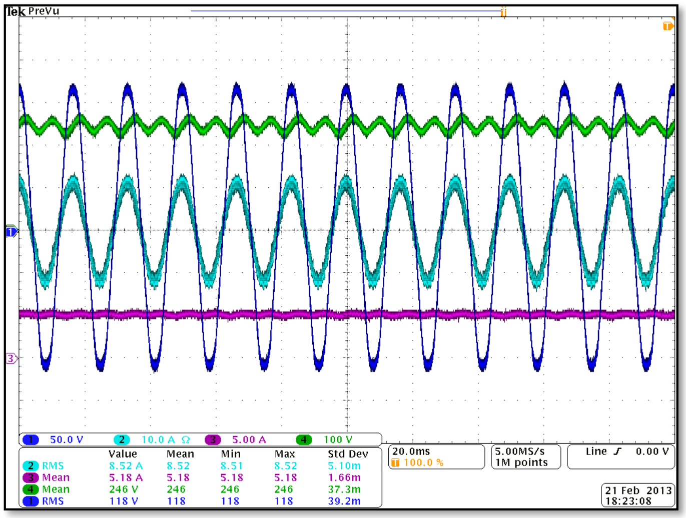

	Value	Mean	Min	Max	Std Dev
2 RMS	8.52 A	8.52	8.51	8.52	5.10m
3 Mean	5.18 A	5.18	5.18	5.18	1.66m
4 Mean	246 V	246	246	246	37.3m
1 RMS	118 V	118	118	118	39.2m

Figure 5.14: Charging only operation of the total system.

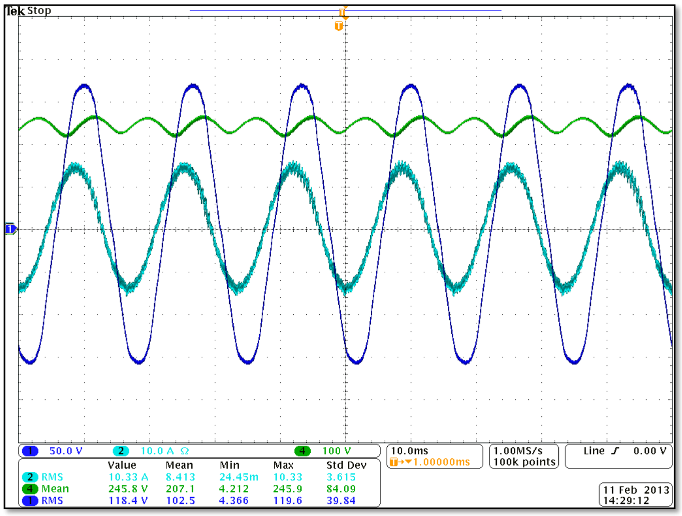

	Value	Mean	Min	Max	Std Dev
2 RMS	10.33 A	8.413	24.45m	10.33	3.615
4 Mean	245.8 V	207.1	4.212	245.9	84.09
1 RMS	118.4 V	102.5	4.366	119.6	39.84

Figure 5.15: Charging and capacitive reactive power operation of the ac-dc converter for pf=0.91 leading.

operation of the system with line current THD is less than 5%. The total apparent power is S=1.2 kVA.

Fig. 5.16 shows the same operation at P_s=0.9 kW and Q_s=-1.0 kVAR. The total apparent power is S=1.35 kVA.

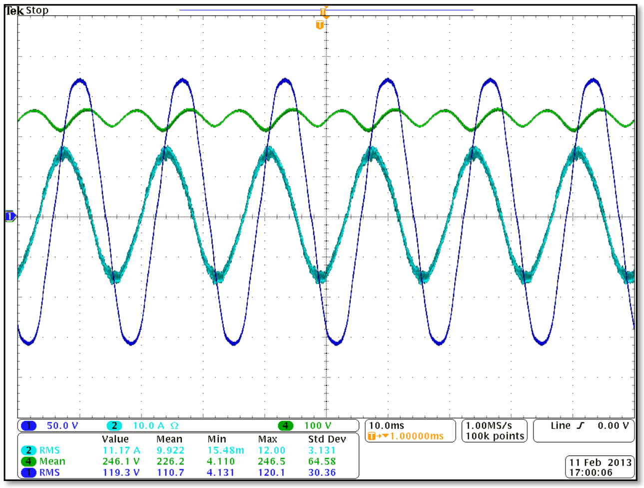

Figure 5.16: Charging and capacitive reactive power operation of the ac-dc converter for pf=0.67 leading.

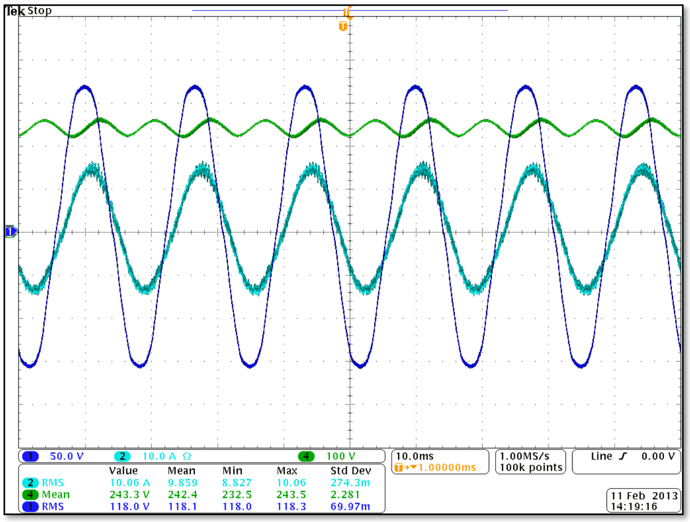

Figure 5.17: Charging and capacitive reactive power operation of the ac-dc converter for pf=0.91 lagging.

5.8.3 Charging and inductive operation

Fig. 5.17 shows the operation of the ac-dc converter for charging and inductive operation mode. The charging power command for the controller is P_s=1.1 kW, and the reactive power command is Q_s=0.5 kVAR. The controller satisfies the stable operation of the system with line current THD is less than 5%. The total apparent power is S=1.2 kVA.

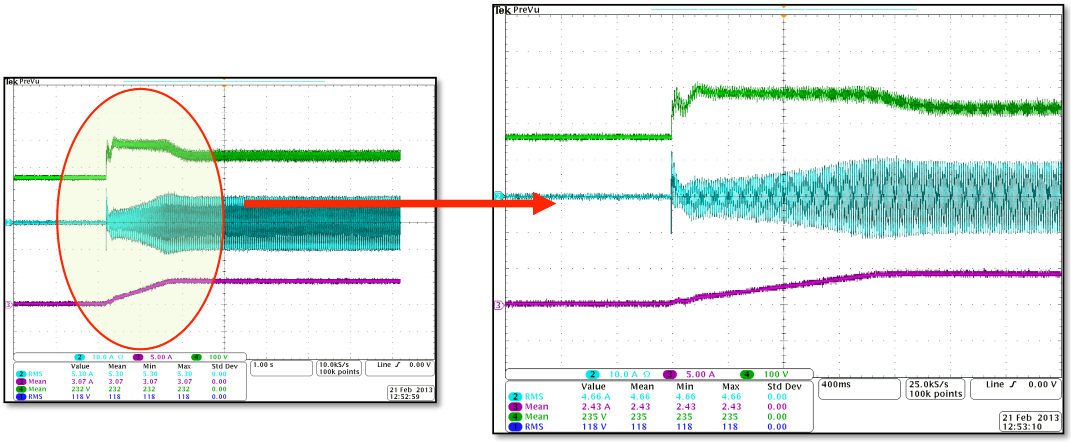

Figure 5.18: Start-up of the charger.

5.8.4 Charger dynamic control tests

In this section, the charger has been tested for its dynamic performance. First, start-up of the system is tested. Then, the response of the charger is tested for the following utility commands: 100% step-up of active power command, 100% step-down of active power command, 100% step-up of capacitive power command, and 100% step-up of inductive power command.

Start-up of the charger

Charger start-up performance is shown in Fig. 5.18. The color code for the variables is the same as the previous experiments. The charger is connected to the grid when the user plugs in to the grid. However, no current is drawn from the grid until the start button is pushed. When the start button is pushed, the charger starts without exceeding the over current limit and the load current gradually increases.

Dynamic performance of the charger

First, the charger input power command has a 100% step up change from 0.5 kW to 1.0 kW. The charger responded to the command in nearly 850 ms (45 cycles) as shown in Fig. 5.19. The second test included a 50% step down change from 1.0 kW

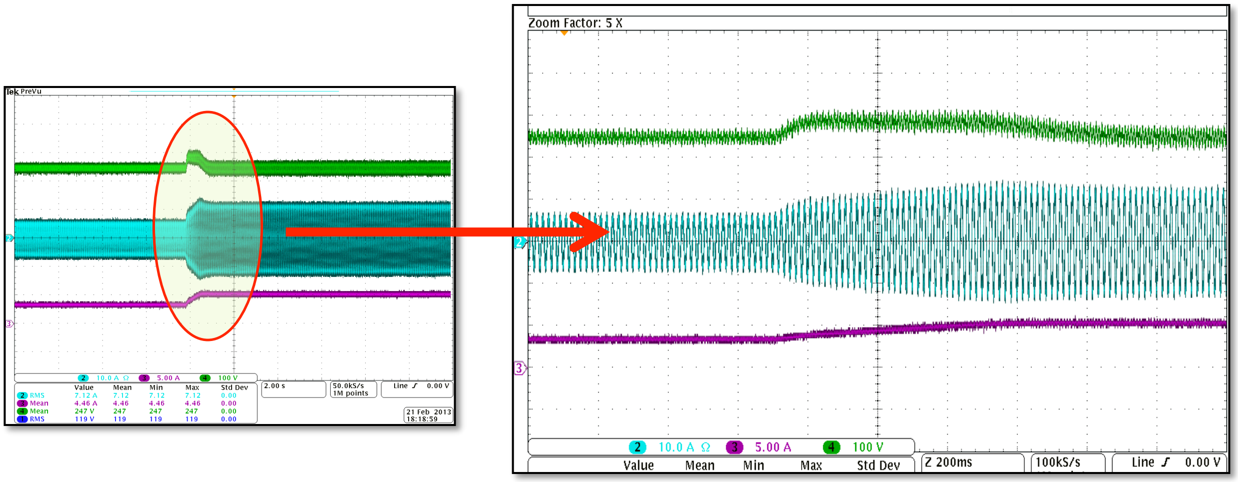

Figure 5.19: 100% active power step-up response of the charger.

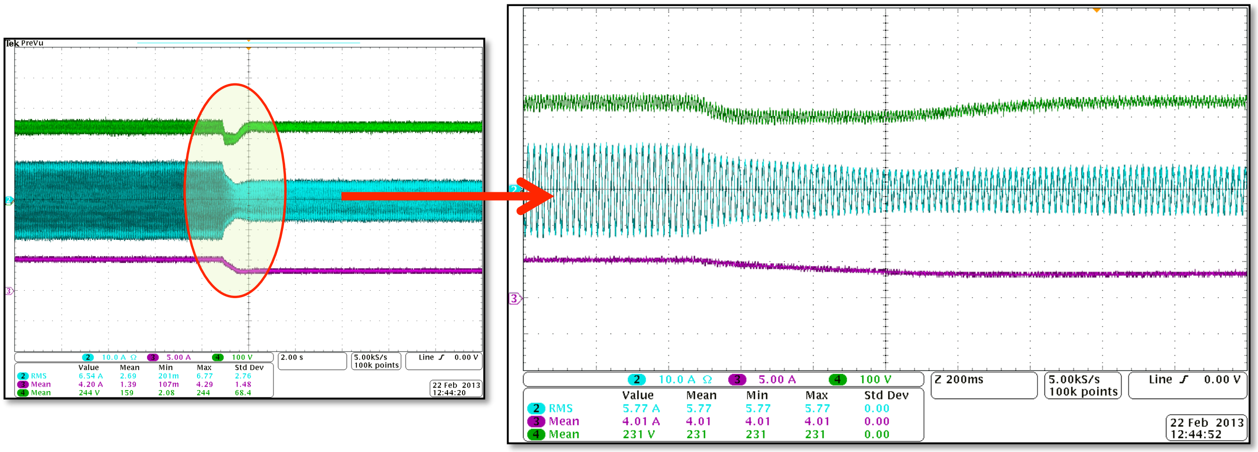

Figure 5.20: 50% active power step-down response of the charger.

to 0.5 kW. The charger responded to the command in nearly 500 ms (30 cycles) as shown in Fig. 5.20.

Next, the reactive power response of the charger is tested. A 100% increase of capacitive reactive power (0 kVAR to -1.0 kVAR) is shown in Fig. 5.21. The settling time is 225 ms (13 cycles). In addition, a 100% increase of inductive reactive power (0 kVAR to 1.0 kVAR) is shown in Fig. 5.22. The settling time is 260 ms (16 cycles).

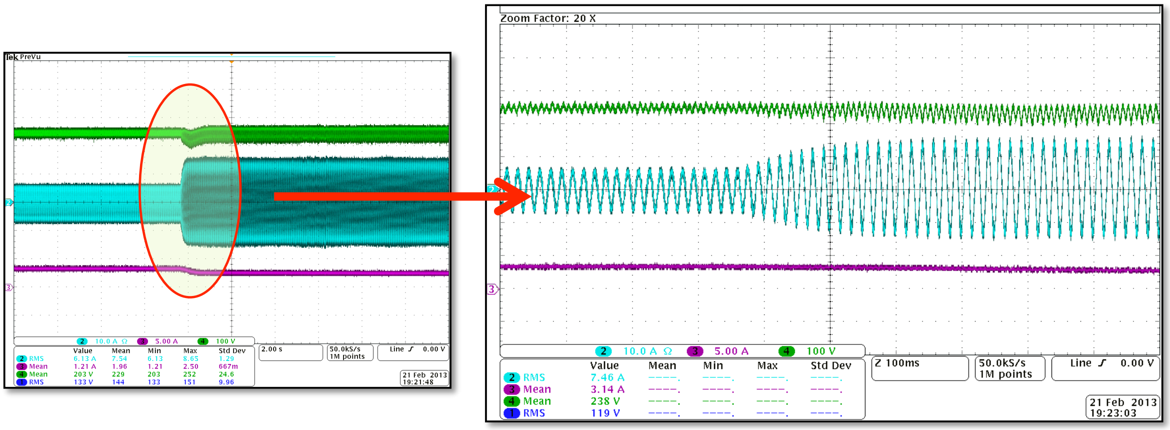

	Value	Mean	Min	Max	Std Dev
2 RMS	6.13 A	7.54	6.13	8.65	1.29
3 Mean	1.21 A	1.96	1.21	2.50	667m
4 Mean	203 V	229	203	252	24.6
1 RMS	133 V	144	133	151	9.96

	Value	Mean	Min	Max	Std Dev
2 RMS	7.46 A	----	----	----	----
3 Mean	3.14 A	----	----	----	----
4 Mean	238 V	----	----	----	----
1 RMS	119 V	----	----	----	----

Figure 5.21: 100% capacitive reactive power step-up response of the charger.

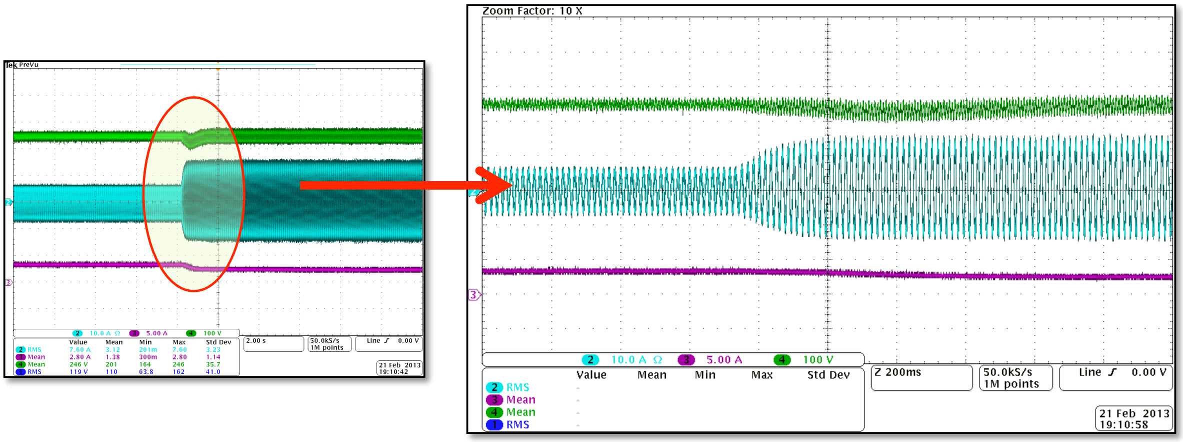

	Value	Mean	Min	Max	Std Dev
2 RMS	7.60 A	3.12	201m	7.60	3.23
3 Mean	2.80 A	1.38	300m	2.80	1.14
4 Mean	246 V	201	164	246	35.7
1 RMS	119 V	110	63.8	162	41.0

	Value	Mean	Min	Max	Std Dev
2 RMS	-				
3 Mean	-				
4 Mean	-				
1 RMS	-				

Figure 5.22: 100% inductive reactive power step-up response of the charger.

5.9 Comparison of Experimental and Analysis Results

The comparison of experimental results and analysis results are presented in this section. The following equation that describes the relation between dc-link capacitor and reactive power is rewritten here:

$$C_{dc} = \frac{\sqrt{S^2 + \left(\omega L_c \frac{S^2}{V_s^2}\right)^2 - 2\omega L_c \frac{S^2}{V_s^2} Q_s}}{\omega \, \Delta V_{dc} V_{dc}} \tag{5.1}$$

5.9.1 Charging only operation

The system parameters are V_s=120 V, L_c=1 mH, C_{dc}=330 μF, and V_{dc}=250 V. During the charging only operation, P_s=1 kW, and Q_s=0 kVAR. Using (5.1), the calculated ΔV_{dc}=32.2 V. The second harmonic peak-to-peak voltage ripple measured using oscilloscope during 1 kW charging only operation is 32.5 V. Therefore, the measured and calculated values match very well providing further verification of the calculated reactive power impact.

5.9.2 Charging and capacitive reactive power operation

Again, the system parameters are V_s=120 V, L_c=1 mH, C_{dc}=330 μF and V_{dc}=250 V. During the operation, P_s=0.9 kW and Q_s=-1.0 kVAR. Using (5.1), the calculated ΔV_{dc}=44.4 V. The second harmonic peak-to-peak voltage ripple measured using oscilloscope during charging and capacitive reactive power operation is 44.1 V. Therefore, the measured and calculated values match very well.

5.9.3 Charging and inductive reactive power operation

Again, the system parameters are V_s=120 V, L_c=1 mH, C_{dc}=330 μF and V_{dc}=250 V. During the operation, P_s=1.1 kW and Q_s=0.5 kVAR. Using (5.1), the calculated ΔV_{dc}=38.4 V. The second harmonic peak-to-peak voltage ripple measured using oscilloscope during charging and capacitive reactive power operation is 36.5 V. Therefore, the measured and calculated values match well.

5.10 Chapter Summary

This chapter explains the design of the charger hardware set-up. The charger is designed with three different modules: gate drive board, main power board, and DSP interface board. All of the boards have been designed in two versions because of the further updates required to increase the system performance. The controller employed for the current control is single-phase PR control. The dynamic performance of the system is tested and verified. The charger can operate in all four quadrants while maintaining that the battery charging current and grid current THD is below the required values. Experimental results are compared with the analysis results for further verification. The results helped us to further interpret the reactive power operation to evaluate the impact of supplying reactive power to the grid. Capital impact is explained in the next section.

Chapter 6

Cost Analysis of Reactive Power Support Using Single-phase On-board Bidirectional Chargers

This chapter describes the cost of providing reactive power using on-board single-phase bidirectional chargers based on the mathematical analysis of reactive power support (Chapters 3 and 4), and the experiments shown in Chapter 5.

Traditional PEV customers who are not interested in providing reactive power support are excluded in the study. There are two types of customers investigated in this study. The first customer profile is the one that is interested in providing reactive power support to the grid but at the same time not willing to sacrifice from the charging time promised over an agreement. This customer will select a charger that comes with an increased kVA rating on top of the charging active power rating. The charger can support maximum 0.8 power factor (pf) whenever requested by the utility grid (leading or lagging). Customer 2 is willing to sacrifice the battery charging time with reactive power support that is equal to charger's kVA rating. This comes with increased charging time but no kVA increase is required.

Two types of cost analyses are investigated. The first calculation shows the annual cost of reactive power support in dollar amount to get the net annual capital value of the reactive power support. The second calculation shows \$/kVAR-annual value to compare with the other options of reactive power support of the utility that are readily available in today's grid [88]. This calculation gives a better idea of the cost in terms of power system perspective. The following assumptions are made for the cost calculations.

- communication cost with the utility grid to realize reactive power operation is not included.
- total bulk cost of components are half of the total unit cost of the components.
- the increased cost of maintenance of the charger components due to reactive power operation is not included.
- EVSE cost increase due to reactive power communication requirement is 5% of the total EVSE cost.
- EVSE cost is 1,000 and charger cost is \$250/kVA

6.1 Customer Profile 1

6.1.1 Incremental costs

The up front incremental costs can be found by comparing the currently used unidirectional charger ac-dc converter and the full-bridge ac-dc converter that are shown in Fig. 6.1. Table 6.1 lists the cost of the additional components required. The total incremental component cost increase is \$49 irrespective of kVA increase.

The kVA increase for customer 1 also adds more cost to the charger. Considering a cost of \$250/kVA for the charger, 0.8 pf reactive power support requires \$75 more incremental cost. Also, with bidirectional support capability, EVSE is assumed to

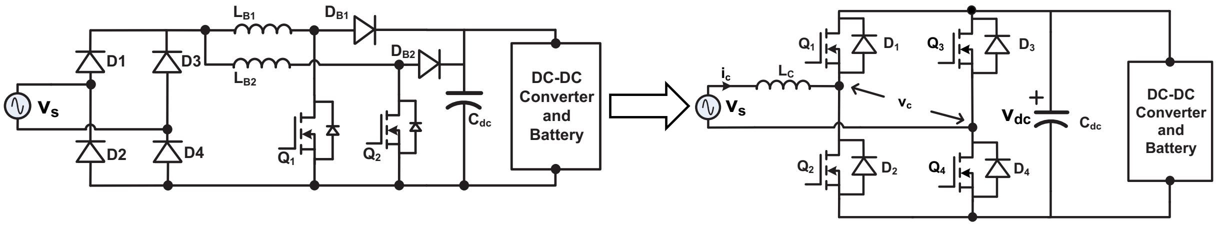

Figure 6.1: Reqiured changes for V2G reactive power support capability.

Table 6.1: Incrimental cost of ac-dc converter for bidirectional charger.

Component	Unidirectional charger	Bidirectional charger	Cost increase
Slow diodes	4	0	−$12
Fast diodes (SiC)	2	4	$74
MOSFET (Si)	2	4	$17
MOSFET driver	2	4	$20
Total unit cost increase			$98
Total bulk cost increase			$49

have a 5% initial cost increase. For a $1,000 EVSE, this corresponds to $50. These are listed in Table 6.2. Total initial incremental costs become $125+$49=$174.

6.1.2 Operating costs

The electricity cost due to the converter losses during reactive power operation will be the operating cost of the charger.

The charger normally operates at 1.2 kW charging operation. If utility allocates a 0.9 kVAR capacitive/inductive reactive power on top of the charging active power,

Table 6.2: Additional incremental cost of charger and EVSE.

Component	Unidirectional charger	Bidirectional charger	Cost increase
kVA increase for 0.8 pf support	1.2 kVA	1.5 kVA	$75
EVSE cost increase (5%)			$50
Total cost increase			$125

then the charger operates at 0.8 pf with 1.5 kVA apparent power. The experimental studies showed that this adds a 70 W more as losses.

The grid operator can always allocate this 0.9 kVAR of reactive power support from the customer 1 whenever needed. However, the minimum added losses are 70 W. Considering the price of electricity ($0.1/kWh), availability of the vehicle at the residential outlet (6:00pm-8:00am, 14 hours/day), and including a capacity factor of 0.25, the total annual cost of the electricity is calculated as follows:

$$C = 0.07kW \times \$0.1/kWh \times 14h \times 0.25 \times 365days = \$8.95 - annual \tag{6.1}$$

The capacity factor was required for the calculation. Utility will not always ask for 0.9 kVAR all the time, but as an assumption it demands one-fourth of the reactive power capability on average during 14 hours of operation. Including a 3% inflation over 10 years of usage, the annual cost becomes $10.25.

6.1.3 Net cost

Net annual cost of the reactive power operation for customer 1 is $174/10+$10.25=$27.65 for 0.9 kVAR of reactive power operation. Another way of calculating the cost of reactive power is as follows:

$$\begin{aligned} \$/\text{kVAR} &= \frac{\text{Total annual VAR support cost}}{\text{Total inductive and capacitive range}} \\ &= \frac{\$(174/10 + 10.25)}{1.8\text{kVAR}} \\ &= \$15.3/\text{kVAR-annual} \end{aligned} \tag{6.2}$$

A similar calculation is also done for a charger rated at 3.3 kVA. Using the same calculations above, the charger's annual cost of providing 2.46 kVAR of reactive power to the grid is $67.6. Using the second way of calculation, it costs $13.75/kVAR-annual for total inductive and capacitive range.

6.2 Customer Profile 2

6.2.1 Incremental costs

The total component cost increase is the same with customer 1 and \$49. Since there is no kVA increase required, only EVSE cost increase will be added. Therefore, the total cost increase is \$49+\$50=\$99.

6.2.2 Operating costs

The electricity cost due to the converter losses during reactive power operation will be the operating cost of the charger. If utility allocates all the available power output of the converter and demands -1.44 kVAR of reactive power, the experimental studies showed that this causes a 200 W as losses.

The grid operator can always allocate this 1.44 kVAR of reactive power support from the customer 2 whenever needed. However, the minimum added losses are 200 W. Considering the price of electricity (\$0.1/kWh), availability of the vehicle at the residential outlet (6:00pm-8:00am, 14 hours/day), and including a capacity factor of 0.25, the total annual cost of the electricity is calculated as follows:

$$C = 0.2kW \times \$0.1/kWh \times 14h \times 0.25 \times 365days = \$25.55 - annual \tag{6.3}$$

The capacity factor was required for the calculation. Utility will not always ask for 1.44 kVAR all the time, but as an assumption it demands one-fourth of the reactive power capability on average during 14 hours of operation. Including a 3% inflation over 10 years of usage, the annual cost becomes \$30.1.

6.2.3 Net cost

Net annual cost of the reactive power operation for customer 2 is \$99/10+\$30.1=\$40 for 1.44 kVAR of reactive power operation. Another way of calculating the cost of reactive power is as follows:

$$\begin{aligned}\$/\text{kVAR} &= \frac{\text{Total annual VAR support cost}}{\text{Total inductive and capacitive range}} \\ &= \frac{\$(99/10+30.1)}{2.88\text{kVAR}} \\ &= \$13.8/\text{kVAR-annual} \qquad (6.4)\end{aligned}$$

A similar calculation is also done for a charger rated at 3.3 kVA. Using the same calculations above, the charger's annual cost of providing 3.3 kVAR of reactive power to the grid is $55.1. Using the second way of calculation, it costs $8.4/kVAR-annual for total inductive and capacitive range.

6.3 Summary and Conclusion of the Chapter

In this chapter, the cost of supplying reactive power using a single-phase on-board bidirectional charger is analyzed for two different customer scenarios. The experimental data of the previous chapter is used to compute the operating cost of the charger. A power loss estimation is done for 3.3 kVA case to conclude the cost results.

Today, the cost of supplying reactive power using distribution system capacitor banks is $2.8/kVAR [88]. This amount is almost one-third of the reactive power supplied by customer 2 using a Level 2 charger. However, the following benefits are included using the on-board charger for reactive power support which are not readily available with capacitor banks:

- dynamic compensation instead of stepped compensation.
- increased power quality with active harmonic filtering.
- inductive reactive power support is possible.
- elimination of residential reactive power consumption penalty in the future.

Chapter 7

Conclusions and Future Study

7.1 Summary of the Study

This study focuses on reactive power operation analysis of single-phase on-board bidirectional chargers. The first chapter described the alternative energy vehicles and different battery technologies. Furthermore, the charging specific terms, profiles, charging standards and grid connection codes were discussed. The second chapter presented a review of available single-phase on-board charger topologies and specifically focused on bidirectional operation. The discussion further extended to dc-dc converters and integrated chargers.

In Chapter 3, a mathematical analysis of bidirectional operation was performed. The relationship between reactive power operation, coupling inductance, dc-link second harmonic ripple current and voltage have been quantified. The net effect of reactive power operation has been a 2.1%-4.3% increase on dc ripple current and capacitance depending on the charger power rating.

Chapter 4 discussed the MATLAB simulations developed to test system performance and overall system control. Switching and average models of the system are presented. Single-phase dq control was tested for the line current control.

Chapter 5 is devoted to explain the hardware development to demonstrate the bidirectional operation. Modular development of the system helped with debugging of the faulty boards and easier changes/upgrades. While a MATLAB simulation is developed with the control system blocks in Chapter 4, a PSIM simulation is used to directly develop the hardware C code in Chapter 5. This helped with debugging of the hardware. A TI F28335 floating point DSP is used to control the system. Three different operation modes are tested: charging only operation, charging and capacitive operation, and charging and inductive operation. The dynamic tests verified the performance of the controller.

Chapter 6 showed the analysis of the net cost calculation of the reactive power operation which includes incremental costs and operating costs. Two PEV customer profiles were investigated. Customer 1 represents customers that do not want charging time increase with added reactive power operation. Customer 2 is more flexible with charging time and can supply more reactive power. The cost of reactive power drops as the charger rating increases. Also, reactive power cost of customer 2 is cheaper than customer 1 due to decreased incremental costs.

7.2 Contributions of the Dissertation

The contributions of this study can be summarized as follows:

- The available topologies for reactive power operation using on-board single-phase chargers are analyzed. The pros and cons of each different ac-dc topology are discussed to shed light on their suitability for reactive power support.

- The analysis of reactive power operation for single-phase ac-dc converter is analyzed. The relationship between dc-link variables and reactive power is quantified. Reactive power operation results in increased demand from the dc-link capacitor (more charge/discharge cycles and increased second harmonic ripple current). However, battery SOC is spared from losses during reactive power operation.

- A new controller for active and reactive power command following for EV/PHEV bidirectional charger is designed and experimentally demonstrated. The controller receives active and reactive power inputs from the utility grid and adjusts the line current and battery current without any over-shoot or under-shoot of DC-link voltage. DC-link voltage changes between its maximum and minimum values based on the received power commands.
- Cost analysis of reactive power operation is achieved to quantify the real value of reactive power support using bidirectional on-board chargers.

7.3 Future Study

There are two future studies that can be further investigated:

- The single-phase on-board charger can be reconfigured to a three-phase on-board charger with minimal modification to the current charger. Using the three phase-legs already available in the single-phase charger, it is possible to skip the dc-dc converter and directly convert three-phase ac voltage into dc voltage and charge the battery. This will increase the total efficiency, and decrease the dc-link voltage ripple thanks to the three-phase system.
- Another future study is the reactive power analysis of the three-phase off-board chargers. It is possible that these chargers will be available to the public in shopping malls, big parking lots, or in fast charging stations. The incremental cost analysis will be done between unidirectional off-board chargers and bidirectional off-board chargers. It is expected that the annual cost of

supplying reactive power (per kVAR) to the grid may be lower than the single-phase on-board chargers. What is more, they are stationary making them more valuable for grid support.

Bibliography

Bibliography

[1] J. Axsen, A. Burke, and K. Kurani, “Batteries for plug-in hybrid electric vehicles (PHEVs): Goals and the state of technology circa 2008,” Inst. Transportation Stud., Univ. California, Davis, CA, Tech. Rep., 2008.

[2] D. Anderson. (2008, Summer) Status and trends in the HEV/PHEV/EV battery industry. Rocky Mountain Inst.

[3] A. Burke and M. Miller, “Emerging lithium-ion battery technologies for PHEVs: test data and performance comparisons,” presented at the Pre-conf. battery workshop, Plug-in 2008, San Jose, CA, Jul. 2008.

[4] G. Nagasubramanian, “Current trends in materials development for Li-ion batteries,” presented at the Workshop on Batteries, Indiana Univ., Nov. 2009.

[5] P. G. Patil, “Developments in lithium-ion battery technology in The People’s Republic of China,” Argonne Nat. Lab., Tech. Rep. ANL/ESD/08-1, January 2008.

[6] R. F. Nelson and M. A. Kepros, “Ac ripple effects on VRLA batteries in float applications,” in *Battery Conf. Appl. Advances*, Long Beach, CA, Jan. 1999.

[7] *IEEE Recommended Practices and Requirements for Harmonic Control in Electrical Power Systems*, IEEE Std. 519-1992, issued in 1993, updated in 2002.

[8] *IEEE Standard for Interconnecting Distributed Resources with Electric Power Systems*, IEEE Std. 1547-2003, issued in 2003, reaffirmed in 2008.

[9] O. C. Onar, “Bi-directional ac/dc and dc/dc converters for plug-in hybrid electric vehicles with hybrid battery/ultra-capacitor energy storage systems,” Ph.D. dissertation, Illinois Inst. Technology, Chicago, IL, Jul. 2010.

[10] (2008, Aug.) Lithium ion. [Online]. Available: www.sanyo.com

[11] E. Partington, “Plug-in hybrid electric vehicle charging systems: Battery chargers,” presented at the The Bussiness of Plugging In, Detroit, MI, Oct. 2010.

[12] L. Tang and G.-J. Su, “A low-cost, digitally-controlled charger for plug-in hybrid electric vehicles,” in *IEEE Energy Conversion Congr. Expo. (ECCE)*, San Jose, CA, Sep. 20–24 2009, pp. 3923–3929.

[13] “International energy outlook 2011,” U.S. Dept. Energy, Tech. Rep. OE/EIA-0484(2011), Sep. 2011. [Online]. Available: http://www.eia.gov/forecasts/ieo/pdf/0484(2011).pdf

[14] S. E. Letendre and W. Kempton, “The V2G concept: a new model for power?” *Public Utilities Fortnightly*, pp. 16–26, Feb. 2002.

[15] W. Kempton and S. E. Letendre, “Electric vehicles as a new power source for electric utilities,” *Transpn. Res.*, vol. 2, no. 3, pp. 157–175, 1997.

[16] B. Ozpineci. Grid support services from PHEVs and BEVs.

[17] M. Yilmaz and P. T. Krein, “Review of the impact of vehicle-to-grid technologies on distribution systems and utility interfaces,” *IEEE Trans. Power Electron.*, to be published.

[18] J. Kessen. (2012, Sep.) Vehicle-to-grid: An intriguing, but challenging, opportunity. [Online]. Available: http://info.a123systems.com/blog/bid/158802/Vehicle-to-Grid-An-Intriguing-but-Challenging-Opportunity

[19] C. Zhou, K. Qian, and W. Zhou, “Modeling of the cost of EV battery wear due to V2G application in power systems,” *IEEE Trans. Energy Convers.*, vol. 26, no. 4, pp. 1041–1050, Dec. 2011.

[20] E. Sortomme and M. A. El-Sharkawi, “Optimal charging strategies for unidirectional vehicle-to-grid,” *IEEE Trans. Smart Grid*, vol. 2, no. 1, pp. 131–138, Mar. 2011.

[21] “Principles for efficient and reliable reactive power supply and consumption,” Federal Energy Regulatory Commission, Tech. Rep., Feb. 2005. [Online]. Available: http://www.ferc.gov/eventcalendar/files/20050310144430-02-04-05-reactive-power.pdf

[22] F. Musavi, M. Edington, W. Eberle, and W. G. Dunford, “Energy efficiency in plug-in hybrid electric vehicle chargers: evaluation and comparison of front end ac-dc topologies,” in *IEEE Energy Conversion Congr. Expo. (ECCE)*, Phoenix, AZ, Sep. 2011, pp. 273–280.

[23] A. Khaligh and S. Dusmez, “Comprehensive topological analysis of conductive and inductive charging solutions for plug-in electric vehicles,” *IEEE Trans. Veh. Technol.*, vol. 61, no. 8, pp. 3475–3489, Oct. 2012.

[24] D. C. Erb, O. C. Onar, and A. Khaligh, “Bi-directional charging topologies for plug-in hybrid electric vehicles,” in *IEEE Applied Power Electron. Conf. Expo. (APEC)*, Palm Springs, CA, Feb. 21–25 2010, pp. 2066–2072.

[25] M. Yilmaz and P. T. Krein, “Review of battery charger topologies, charging power levels and infrastructure for plug-in electric and hybrid vehicles,” *IEEE Trans. Power Electron.*, vol. 28, pp. 2151–2169, May 2013.

[26] B. Singh, B. N. Singh, A. Chandra, K. Al-Haddad, A. Pandey, and D. P. Kothari, “A review of single-phase improved power quality ac-dc converters,” *IEEE Trans. Ind. Electron.*, vol. 50, no. 5, pp. 962–981, Oct. 2003.

[27] R. Wang, F. Wang, D. Boroyevich, R. Burgos, R. Lai, P. Ning, and K. Rajashekara, “A high power density single-phase PWM rectifier with active ripple energy storage,” *IEEE Trans. Power Electron.*, vol. 26, no. 5, pp. 1430–1443, May 2011.

[28] D. Dong, D. Boroyevich, R. Wang, and I. Cvetkovic, “A two-stage high power density single-phase ac-dc bi-directional PWM converter for renewable energy systems,” in *IEEE Energy Conversion Congr. Expo. (ECCE)*, Atlanta, GA, Sep. 12–16 2010, pp. 3862–3869.

[29] “Energy independence and security act of 2007,” H.R.6, 110^{th} U.S. Congress, 2007.

[30] (2010, Aug.) 2011 Chevrolet Volt plug-in hybrid electric car. [Online]. Available: http://www.chevrolet.com/pages/open/default/future/volt.do

[31] (2010, Aug.) Nissan Leaf electric car. [Online]. Available: http://www.nissanusa.com/leaf-electric-car/index#/leaf-electric-car/index

[32] M. C. Kisacikoglu, A. Bedir, B. Ozpineci, and L. M. Tolbert, “PHEV-EV charger technology assessment with an emphasis on V2G operation,” Oak Ridge Nat. Lab., Tech. Rep. ORNL/TM-2010/221, Mar. 2012.

[33] (2011, Nov.) Mini E specifications. [Online]. Available: http://www.miniusa.com/minie-usa/pdf/MINI-E-spec-sheet.pdf

[34] (2011, Nov.) BMW media information. [Online]. Available: http://www.abrbuzz.co.za/BMW_ActiveE_EN.pdf

[35] (2011, Nov.) The new BMW Active E. [Online]. Available: http://www.bmw.com/com/en/newvehicles/1series/activee/2011/showroom/_shared/catalogue/pdf/active_e_flyer.pdf

[36] (2011, Nov.) Wiki: BYD F3DM. [Online]. Available: http://wapedia.mobi/en/BYD_F3DM

[37] (2011, Nov.) 2012 Fisker Karma specifications. [Online]. Available: http://www.fiskerautomotive.com/Content/pdf/Fisker_Karma_Specs%20V2.pdf

[38] (2011, Nov.) Ford Focus Electric technical specifications. [Online]. Available: http://media.ford.com/images/10031/2012_Focus_Elec_Specs.pdf

[39] (2011, Nov.) Ford Transit Connect EV specifications. [Online]. Available: http://media.ford.com/images/10031/2011_TCElectric_Specs.pdf

[40] (2011, Nov.) Transit Connect Electric- specifications and ordering guide. [Online]. Available: http://www.azuredynamics.com/products/documents/SPC501074-A_TCE_Specifications_and_Ordering_Guide.pdf

[41] (2011, Nov.) General Motors EV1. [Online]. Available: http://en.wikipedia.org/wiki/General_Motors_EV1#Battery

[42] (2011, Jan.) Mitsubishi MiEV. [Online]. Available: http://www.mitsubishi-motors.com/special/ev/whatis/index.html

[43] S. Albertus. (2011, Nov.) Z.E. [Online]. Available: http://www.energythink.it/materiale/firenze/Abstract%20relatori/4_Albertus_presentation_firenze.pdf

[44] (2011, Jan.) Tesla Motors. [Online]. Available: http://www.teslamotors.com/goelectric/charging

[45] (2011, Nov.) Think City specifications. [Online]. Available: http://www.thinkev-usa.com/why-think-city/specs

[46] (2010) Hybrid vehicle dismantling manual. [Online]. Available: https://techinfo.toyota.com/techInfoPortal/staticcontent/en/techinfo/html/prelogin/docs/priusphvdisman.pdf

[47] A. Mendoza and J. Argueta, “Performance characterization of 1999 Toyota RAV4 EV- conductive,” Southern California Edison, Tech. Rep., Jan. 2000.

[48] J. Hartline, “Advanced technology vehicle overview,” presented at the Sustainability mobility seminar, 2011. [Online]. Available: http://www.toyota.com/esq/pdf/2011_SMS_Hartline&Soto.pdf

[49] (2010, Sep.) DOE vehicle technologies program: Energy storage. [Online]. Available: http://www1.eere.energy.gov/vehiclesandfuels/technologies/energy_storage/index.html

[50] R. C. Stempel, S. R. Ovshinsky, P. R. Gifford, and D. A. Corrigan, “Nickel-metal hydride: ready to serve,” *IEEE Spectr.*, pp. 29–34, Nov. 1998.

[51] (2012, Jan.) Nickel metal hydride battery. [Online]. Available: http://en.wikipedia.org/wiki/Nickelmetal_hydride_battery

[52] J. Voelcker, “Lithium batteries take to the road,” *IEEE Spectr.*, pp. 27–31, Sep. 2007.

[53] A. Paseran, “Battery choices and potential requirements for plug-in hybrids,” presented at the Plug-in Hybrid Electric Truck Workshop, Hybrid Truck Users Forum, Los Angeles, CA, Feb. 2007.

[54] F. R. Kalhammer, “Prospects of batteries for PHEV applications,” in *23rd Elect. Vehicle Symp.*, Anaheim, CA, Dec. 2007.

[55] R. Gehm, “Sustainability on a small scale,” *Automative Eng. Int.*, pp. 28–32, Apr. 2008.

[56] A. Burke, “Batteries and ultracapacitors for electric, hybrid, and fuel cell vehicles,” *Proc. IEEE*, vol. 95, no. 4, pp. 806–820, 2007.

[57] *SAE electric vehicle and plug-in hybrid electric vehicle conductive charge coupler*, SAE International Std. J1772, Jan. 2010.

[58] M. F. M. Elias, K. M. Nor, N. A. Rahim, and A. K. Arof, “Lithium-ion battery charger for high energy application,” in *IEEE Nat. Power Eng. Conf.*, Dec. 2003.

[59] A. J. Ruddell, A. G. Dutton, H. Wenzl, C. Ropeter, D. U. Sauer, J. Merten, C. Orfanogiannis, J. W. Twidell, and P. Vezin, “Analysis of battery current microcycles in autonomous renewable energy systems,” *J. Power Sources*, vol. 112, pp. 531–456, 2002.

[60] C. Ropeter, H. Wenzl, and H.-P. Beck, “The impact of microcycles on batteries in different applications,” in *Elect. Vehicle Symp.*, Berlin, Germany, Oct. 2001.

[61] V. Svoboda, H. Wenzl, R. Kaiser, A. Jossen, I. Baring-Gould, J. Manwell, P. Lundsager, H. Bindner, T. Cronin, P. Norgard, A. Ruddell, A. Perujo, K. Douglas, C. Rodrigues, A. Joyce, S. Tselepis, N. v. d. Borg, F. Nieuwenhout, N. Wilmot, F. Mattera, and D. U. Sauer, “Operating conditions of batteries in off-grid renewable energy systems,” *Solar Energy*, vol. 81, no. 11, pp. 1409–1425, 2007.

[62] M. H. Townsend and D. L. Cunningham, “Ac ripple currents in UPS dc link,” in *Internat. Stationary Battery Conf.*, Tampa, FL, 2007.

[63] R. Blohm, “Summary of ac ripple considerations on dc battery systems,” in *Canadian Battery Symp.*, 2001.

[64] A. I. Harrison, “Batteries and ac phenomena in UPS systems,” in *Telecommun. Energy Conf.*, Florence, Italy, 1989.

[65] A. Jossen, “Fundamentals of battery dynamics,” *J. Power Sources*, vol. 154, no. 2, pp. 530–538, 2005.

[66] W. K. Bennett, “Stationary battery charger specifications demystified,” in *Internat. Stationary Battery Conf.*, Marco Island, FL, 2003.

[67] S. S. Misra and L. S. Holden, "UPS battery life characteristics," in *Battery Conf. Appl. Advances*, 1991.

[68] "Long-range EV charging infrastructure plan for tennessee-draft," Electr. Transportation Eng. Corp., Tech. Rep., 2010. [Online]. Available: http://www.ci.knoxville.tn.us/sustainability/ecotality_longrangeplan.pdf

[69] M. Kuss, T. Markel, and W. Kramer, "Application of distribution transformer thermal life models to electrified vehicle charging loads using monte-carlo method," in *Elect. Vehicle Symp.*, Shenzen, China, Nov. 5–9 2010.

[70] R. Moghe, F. Kreikebaum, J. E. Hernandez, R. P. Kandula, and D. Divan, "Mitigating distribution transformer lifetime degradation caused by grid-enabled vehicle (GEV) charging," in *IEEE Energy Conversion Congr. Expo. (ECCE)*, Phoenix, AZ, 2011, pp. 835–842.

[71] J. P. M. Figueiredo, F. L. Tofoli, and B. L. A. Silva, "A review of single-phase PFC topologies based on the boost converter," in *IEEE Internat. Conf. Industry Appl.*, Sao Paulo, Brazil, Nov. 2010, pp. 1–6.

[72] B. A. Miwa, D. M. Otten, and M. F. Schlecht, "High efficiency power factor correction using interleaving techniques," in *IEEE Applied Power Electron. Conf. Expo. (APEC)*, Boston, MA, Feb. 1992, pp. 557–568.

[73] D. Gautam, F. Musavi, M. Edington, W. Eberle, and W. G. Dunford, "An automotive on-board 3.3 kW battery charger for PHEV application," in *IEEE Vehicle Power Propulsion Conf. (VPPC)*, Chicago, IL, 2011, pp. 1–6.

[74] D. S. Gautam, F. Musavi, M. Eddington, W. Eberle, and W. G. Dunford, "An automotive onboard 3.3-kW battery charger for PHEV application," *IEEE Trans. Veh. Technol.*, vol. 61, no. 8, pp. 3466–3474, Oct. 2012.

[75] R. Martinez and P. N. Enjeti, “A high-performance single-phase rectifier with input power factor correction,” *IEEE Trans. Power Electron.*, vol. 11, no. 2, pp. 311–317, 1996.

[76] J.-W. Lim and B.-H. Kwon, “A power factor controller for single-phase PWM rectifiers,” *IEEE Trans. Ind. Electron.*, vol. 46, no. 5, pp. 1035–1037, 1999.

[77] M. A. Fasugba and P. T. Krein, “Gaining vehicle-to-grid benefits with unidirectional electric and plug-in hybrid vehicle chargers,” in *IEEE Vehicle Power Propulsion Conf. (VPPC)*, Chicago, IL, Sep. 2011, pp. 1 – 6.

[78] G. R. Stanley and K. M. Bradshaw, “Precision dc-to-ac power conversion by optimization of the output current waveform-the half bridge revisited,” *IEEE Trans. Power Electron.*, vol. 14, no. 2, pp. 372–380, 1999.

[79] H. Qian, J.-S. Lai, J. Zhang, and W. Yu, “High efficiency bidirectional ac-dc converter for energy storage systems,” in *IEEE Energy Conversion Congr. Expo. (ECCE)*, Atlanta, GA, 2010, pp. 3224–3229.

[80] G. Pellegrino, E. Armando, and P. Guglielmi, “An integral battery charger with power factor correction for electric scooter,” *IEEE Trans. Power Electron.*, vol. 25, no. 3, pp. 751–759, 2010.

[81] L. Solero, “Nonconventional on-board charger for electric vehicle propulsion batteries,” *IEEE Trans. Veh. Technol.*, vol. 50, no. 1, pp. 144–149, 2001.

[82] F. Lacressonniere and B. Cassoret, “Converter used as a battery charger and a motor speed controller in an industrial truck,” in *European Conf. Power Electron. Appl.*, Dresden, Germany, 2005.

[83] M. Kruger, “Integrated traction and charging unit for battery fed vehicles,” in *European Conf. Power Electron. Appl.*, Lausanne, Switzerland, 1999.

[84] A. Davis, Z. M. Salameh, and S. S. Eaves, “Evaluation of lithium-ion synergetic battery pack as battery charger,” *IEEE Trans. Energy Convers.*, vol. 14, no. 3, pp. 830–835, 1998.

[85] (2010) Ac Propulsion reductive charger. [Online]. Available: http://www.acpropulsion.com/products-reductive.html

[86] R. Zhang, M. Cardinal, P. Szczesny, and M. Dame, “A grid simulator with control of single-phase power converters in d-q rotating frame,” in *IEEE Power Electronics Specialists Conf. (PESC)*, vol. 3, 2002, pp. 1431–1436.

[87] D. Dong, “Modeling and control design of a bidirectional PWM converter for single-phase energy systems,” Master’s thesis, Virginia Polytechnic Inst. State Univ., 2009.

[88] C. Tufon, A. G. Isemonger, B. Kirby, J. Kueck, and F. Li, “A tariff for reactive power,” Oak Ridge Nat. Lab., Tech. Rep. ORNL/TM-2008/083, Jun. 2008. [Online]. Available: http://info.ornl.gov/sites/publications/files/Pub11472.pdf

Vita

Mithat C. Kisacikoglu received the B.S. degree from Istanbul Technical University in 2005 and the M.S. degree from University of South Alabama in 2007, both in electrical engineering.

He has been a Ph.D. student and research assistant at at the University of Tennessee in power electronics major since August 2007. He has also been a student researcher in the Power and Energy Systems Group and in the the Power Electronics and Electric Machinery Group at the Oak Ridge National Laboratory since May 2008. His research areas include plug-in electric vehicles and renewable energy and energy storage system grid-interface circuit design and control.